**Synthesis and Assembly of Anisotropic Ellipsoidal Particles**

**by**

**Aayush Amit Shah**

**A dissertation submitted in partial fulfillment**
**of the requirements for the degree of**
**Doctor of Philosophy**
**(Macromolecular Science and Engineering)**
**in The University of Michigan**
**2014**

**Doctoral Committee:**

Professor Michael J. Solomon, Chair
Professor Sharon C. Glotzer
Professor Peter F. Green
Assistant Professor Charles W. Monroe

## Dedication

This dissertation is dedicated to my grandfather

Jayantbhai Shah,

who I miss very much.

**Acknowledgements**

As I complete this wonderful experience, I'd like to take this opportunity to pen down my heartfelt gratitude to the people who are responsible for all the work that I have done in my PhD.

I would like to start by first acknowledging the immense role played by my research advisor Prof. Michael J. Solomon. Prof. Solomon has ensured that we maintained the highest standards of research quality in this work by not only necessitating the practice of cutting edge research techniques but also enforcing a stringent moral code of conduct while performing and reporting research work. I am indebted to him for giving me the opportunity to work with him and this experience will surely hold me in good stead as I enter my professional career.

I would like to thank my committee members: Prof. Sharon C. Glotzer, Prof. Peter F. Green and Asst. Prof. Charles W. Monroe. I have had the opportunity to work with them during my PhD. and their suggestions have proven to be invaluable. Collaborations with Prof. Glotzer and her group as well as Prof. Monroe have proven to be critical in the success of our work. I would also like to thank all the professors connected with the NSF-NIRT and ARO-MURI projects that I worked on. I have also had the opportunity to teach a junior-senior level chemical engineering class during my PhD and I would like to thank Asst. Prof. Fei Wen for being incredibly supportive of my research work while I was the Graduate Student Instructor for her class. I am also grateful to all my collaborators, especially Kevin Kohlstedt and Benjamin Schultz, for their invaluable inputs and for performing research of the highest quality that has made our collaborative work unique and of a broad impact.

The administrative staff connected to both the Macromolecular Science and Engineering Program as well as the Chemical Engineering department have ensured that I was never worried about anything not connected to research. I would like to especially mention Nonna Hamilton, Susan Hamlin, Harald Eberhart and Brian Johnson for going far above and beyond their office duties to help me and ensure that my experiments have the best possible chance of success.

I have had the opportunity to mentor nine undergraduates during my PhD. They have all been incredibly dedicated and have made lasting contributions to not only my work but also the overall work and direction of our group's research efforts. I would like to wish them the very best in their careers.

The Solomon group over the years has been a wonderful support system and virtually my 'Michigan family'. I would like to thank Deshpremy Mukhija and Abhishek Shetty for taking the time to introduce me to research and life as a graduate student in general. I would like to thank all of my colleagues as well as the younger graduate students for their help and understanding throughout my PhD. They have been active collaborators as well as a great sounding board for all of my ideas. Most importantly, they have been great friends and have made work not really seem like work at all.

I would like to thank my friends for always being there whenever I've needed them. I'd first like to thank all the friends from my undergraduate and high school days who I've stayed in touch with. They have helped me maintain a connection to my country and my hometown. I have met wonderful people connected to research, the Indian community, racquetball and just the University in general since coming to Ann Arbor. I have thoroughly

enjoyed this wonderful city with them and completely transformed as an individual in their company. A heartfelt thanks to them all!

I'd like to thank my aunts and uncles in Detroit who have treated me as their own son and have taken me into their families. I have never really missed my family even though they were eight thousand miles away because of them. I'd also like to thank my extended family as well as my brother who have been so interested and supportive of all my work. Finally, I'd like to take this opportunity to thank my parents. They have made tremendous sacrifices so that we could have an enjoyable childhood with strong educational foundations. This work is a direct result of all their efforts.

## Table of Contents

## List of Figures

# Abstract

We create complex non-close packed assemblies from ellipsoidal anisotropic particles using external electric fields in this dissertation. Spherical colloidal particles have long been self-assembled into close-packed 2-D and 3-D ordered structures, while external fields have been used to accelerate their self-assembly as well as to alter the free energy landscape to create novel field driven ordered structures. In the first part of the dissertation, we develop a direct current (DC) electric field assembly method that accelerates the self-assembly of charged colloidal particles. In the second part of the dissertation, we use alternating current (AC) electric fields to alter the free energy landscape and actuate the self-assembled colloidal assemblies created from anisotropic particles.

We report the use of an applied DC electric field to produce anisotropic orientational order in micron-sized Brownian colloidal rods with aspect ratio between about three and eight. The suspensions, because of their slow Brownian dynamics, undergo equilibrium self-assembly only on long time scales. Application of an applied field significantly accelerates the kinetics of assembly. We analyze our results in terms of the underlying electrokinetics of the system as well as connect the observed field-induce orientational order to the equilibrium isotropic-nematic transition predicted for repulsive rods. Body-centered tetragonal crystal phases are observed on assembly of the ellipsoidal particles under optimal conditions. The results show a transition from mobile to glassy dynamics as the field-strength is increased, and

this glassy behavior is an impendent to achieving high-density order structures. We subsequently demonstrate the utility of the DC electric field to assemble nano-micron sized colloidal particles into close-packed ordered structures. We assemble colloidal particles ranging from 100 nm to 1.4 μm into close-packed crystalline structures on the order of ~ 2 minutes. The assemblies obtained for particles between 300-500 nm in size display structural color that spans the visible spectrum. Switching the DC electric field leads to reversible generation of structural color that could potentially be useful for display and camouflage applications.

In the second part of the dissertation, we investigate the assembly of complex particles that have interaction anisotropy in addition to shape anisometry. We report a method to synthesize and image Janus ellipsoid and "kayak"-shaped patchy particles that combine both shape and interaction anisotropy. We specifically self-assemble the Janus ellipsoids into ordered self-limiting one-dimensional chains. This ordered structure is formed due to the combination of both shape and interaction anisotropy of the Janus ellipsoids. The unique unit cell of this ordered cell permits reconfiguration of the positional order of the ellipsoids via a sliding mechanism upon micro-scale actuation by alternating current (AC) electric fields. This actuation permits the reversible elongation of the Janus ellipsoid assembly chain length (by ~ 36%) at short-time scales, comparable to normal elongation of human muscles. Actuation of synthetic Janus ellipsoid assemblies on long time scales further leads to the generation of long, uniform self-assembled chains. These materials have potential applications in microrobotics and artificial muscles

# Chapter 1

# Introduction

Colloidal science is the study of suspensions of sub-micron to micron-sized particles. Colloidal particles have interesting and complex individual properties, their aggregate properties (assemblies) are arguably even more exciting for applications such as photonic bandgap materials, metamaterials, micro robotics, etc. This dissertation is focused on the creation of colloidal assemblies using complex particle-particle and particle-external field interactions.

## 1.1 Colloidal Suspensions

Colloids are sub-micron to micron-sized particles that are suspended in a fluid medium.[1] Colloids are all around us in nature and important to the existence of life itself. Blood, for instance, is a colloidal suspension made up of red and white cells suspended in an aqueous medium. Milk, fog and pigmented inks are some other examples of naturally occurring colloidal materials. Colloids are also a part of several man-made products such as paints, detergents, inks, butter, etc.[2]

Colloidal particles can essentially be made up of any kind of material (like polymers, metals, ceramics, etc) suspended in a wide variety of liquid (organic or aqueous media) and gaseous mediums. However, all colloidal systems, due to their size, universally experience Brownian motion.[1] Brownian motion of colloidal particles is caused due to collisions of particles with fluid molecules. It results in the random, continuous motion of colloidal particles in their

fluid medium. This continuous motion permits a colloidal suspension to explore a wide variety of configurations. Some of these configurations are energetically preferred and the system tends to predominantly adopt those states. This spontaneous adoption of specific configurations leads to the self-assembly of colloids.

## 1.2 Self-Assembly

Self-assembly is a process wherein a disordered system of pre-existing components form an organized structure or pattern based solely on the interactions between the components themselves, and without any external direction.[3] The folding of polypeptide chains into proteins is an example of biological self-assembly.[4] At the macroscopic scale, modular robots can also be self-assembled into pre-determined structures.[5] Self-assembly is thus ubiquitous and observed for a wide variety of size-scales, both in natural and man-made systems. The constituents of any self-assembling system are able to identify their individual roles and positions in the larger organization and the constituents must rely on local interactions to self-assemble, as there are no external directing forces.

### 1.2.1 Self-Assembly and Colloids

Both natural and synthetic colloidal systems undergo self-assembly to form macroscopic structures. Opal gemstones are examples of naturally occurring self-assembled materials that are formed by the assembly of small silica particle into periodic arrays.[6] The periodic silica arrays are responsible for the diffraction of incident light giving rise to the brilliant colors of opals. Synthetic poly(methyl methacrylate) particles have been self-assembled by Pusey and Van

Megen to give similar iridescent colors, thus replicating the optical properties of opal gemstones using man-made colloidal particles that form similar ordered structures.[7]

Self-assembly in colloidal systems occurs primarily due to Brownian motion, excluded volume, and potential interactions between the colloids. As stated earlier, Brownian motion allows a colloidal system to explore a wide variety of structural configurations. Each configuration of the colloidal system is has a specific energy. The colloidal system is able to accesses its free energy space, before settling into a configuration that has the minimum energy. The colloidal system thus maintains this equilibrium configuration over a long time span, and this is the self-assembled state of the colloidal assembly. External factors such as temperature and pressure staying constant, the inter-particle forces in a colloidal suspension determine the energy of a colloidal system. An understanding of these inter-particle forces is thus vital to formulate the interparticle interaction potential, which is vital in the study of colloidal self-assembly.[1]

### 1.2.2 Pair interactions of colloidal particles

Typical forces that cause colloidal particles to interact with each other in most colloidal suspensions include diffusive, dispersion, electrostatic and hydrodynamic forces.[1] The cumulative sums of all these forces, simultaneously present in a colloidal suspension, determine the interparticle forces and thus the free energy in a colloidal system. These forces are a direct function of the particle concentration, charge, shape, size and material of the particles.

Forces between colloidal particles lead to attraction or repulsion between individual particles. The simplest and most basic interactions between colloidal particles occur when they come in contact with each other. These ‘hard’ particle interactions, also known as excluded

volume interactions, are caused due to infinite repulsion between particles when the come in contact (particles are impenetrable).[8] This simple, short-range repulsion is singularly responsible for rich phase behavior in colloidal particle systems at different particle concentrations.[7]

Longer-range attractive and repulsive forces are also present in colloidal particles. For example, the short-range repulsion between two colloidal particles that are similarly charged is called electrostatic repulsion, and can be modeled by the Yukawa potential.[1] Surface colloidal charge is usually acquired due to the dissociation of certain stabilizing groups on the particle surface. On the other hand, van der Waals forces are an example of long-range attractive forces that exist between colloidal particles due to induced dipole moments. This force is a function of the material composition of colloidal particles.[1]

Crucially, a number of such attractive and repulsive forces can all be active simultaneously in colloidal particles. In such cases, these forces are additive in nature and this leads to highly complex interaction potentials. These interaction potentials can be tuned in colloidal particles. For instance, the repulsion between colloidal particles induced by the Yukawa potential can be controlled by screening the charge on colloidal particles through the addition of salt in the colloidal suspension. Similarly, modifying the surface of colloidal particles and creating patchy particles can tune attractive Van der Waals's forces. Thus, tuning the forces between colloidal particles can be used to modulate the interaction potential that directly affects the self-assembled structure of colloidal particles. Hence, colloidal particles serve as exciting systems that can be engineered to create a wide variety of self-assembled structures to form functional materials.

### 1.2.3 Spherical Colloidal Particles

The most commonly studied colloidal particle systems are isotropic, uniform spherical particles. These particles are widely observed in nature and can also be synthesized easily in laboratories. Due to their spherosymmetry, spherical particles have uniform isotropic potentials. Spherical particles interacting through excluded-volume interactions thus have a simple phase diagram that is dependent on particle concentration in the colloidal suspension. Spherical particles form a disordered fluid phase at low volume fractions and transition into close-packed ordered cubic structures at high volume fractions.[7]

Introduction of further repulsive and attractive forces to colloidal sphere suspensions can lead to the formation of other distinct, complex structures. For example, addition of small amounts of polymers to the colloidal solution leads to the generation of attraction between the colloidal particles. This force is called the depletion attraction and is responsible for the formation of space-spanning gel-like structures.[9] Further, the self-assembly of a colloidal suspension that contains more than one type of colloidal sphere (of opposite charge) has shown the formation of a rich variety of ionic crystal phases depending on the size and interaction potential of the constituent colloidal spheres.[10]

The assembly structure and dynamics of spherical particles has been studied widely through experiments and is well understood theoretically. Experimental techniques to analyze spherical colloidal particles are also well established. However, in the realm of ordered self-assembly, colloidal spheres can only form close packed structures. Applications such as materials with photonic bandgaps, metamaterials, filters, etc. however need non-close packed structures. To realize such non-close packed structures, non-uniform, orientation-dependent surface potentials must be created. Anisotropic particle and external fields are a couple of

approaches currently being used to create orientation-dependent surface potentials with the eventual aim of assembling non close-packed structures for applications.[11]

### 1.2.4 Anisotropic Colloidal Particles

Colloidal particles are model systems for atoms and molecules and the various cubic structures observed by self-assembling colloidal particles are also seen in molecular crystals.[10] Molecular crystals, more generally, are however, highly complex and have a variety of different symmetries, a small subset of which are the close packed cubic crystal structures obtained from spherical colloidal particles. The addition of anisotropy to colloidal particles increases the complexity of crystal structures to potentially match those seen in molecular crystals.[11] Apart from the assembly structure, anisotropic particles also have highly complex and distinct single particle, dynamical and rheological behavior.[1,12]

Theory, simulations and more recently experiments have shown that shape anisotropic and interaction anisotropic particles have strong potential in the assembly of complex assembly structures.

#### 1.2.4.1 Shape Anisotropic Colloidal Particles

Due to the break in spherosymmetry, non-spherical particles have more degrees of freedom as compared to simple isotropic spherical particles. The additional degrees of freedom lead to pairwise orientation-dependent interactions between particles as well as the surrounding fluid.[13] Rods, discs and dumbbells are examples of such shape anisotropic particles.[11] In this thesis, we focus on ellipsoidal (rod) particles.

The anisotropic potential of ellipsoids, which is a direct consequence of the particle shape, plays a significant role in the dynamics, assembly and rheological properties of a colloidal suspension. For example, studies by Champion and Mitragotri have shown that spherical particles are much more easily internalized by white blood cells or macrophages as compared to rod shaped particles.[14] The interaction between macrophages and bacteria is purely physical and this confirms the role of shape in interactions of particles with the surrounding.

The shape anisotropy of rod shaped particles leads to the origin of both rotational and translational diffusivity in a rod particle. This diffusivity is a function of not only the size, but also the aspect ratio (length/diameter) of the rod shaped particle.[15] In contrast, diffusivity of spherical particles does not vary in space. This anisotropic diffusivity of rod shaped particles is the origin of complex rheological and assembly properties of rod shaped particles. Rod shaped particles can be assembled into space spanning gel-like structures at far lower volume fractions as compared to spheres.[16] Rods can also be packed at higher volume fractions as compared to spheres.[13] Nematic (orientational order, but no positional order) and smectic (orientational order and 1D positional order) liquid crystal phases along with crystalline phases are observed for rod shaped particles. This rich assembly phase behavior is not observed for spherical particles.[17] Thus, the assembly properties of rod shaped particles are distinct and unique due to the shape of the particle.

Rod shape also directly affects the rheological properties of rod suspensions. It was found that rod gels with higher aspect ratios show restrained dynamics compared to smaller aspect ratio rod-gels.[16]

#### 1.2.4.2 Interaction anisotropic colloidal particles

Particles with heterogeneous surfaces (non-uniform surface composition) that have a pairwise orientation-dependent interaction potential are called interaction anisotropic or patchy colloidal particles.[11] Patchy colloids permit the formation of directional bonds, and have generated much attention and excitement over the past decade. This is because the directional bonds generated by patchy colloids resemble covalent bonds seen at the molecular scale.[18] Hence, novel crystalline structures such as the diamond lattice could potentially be synthesized using patchy colloids.[19] Such materials could have applications in photonic bandgap materials, metamaterials, catalysis, drug delivery, etc.[19-21]

The simplest patchy particles are spherical Janus particles. Janus particles are named after the Roman god 'Janus' who had two faces.[18] These particles similarly have different surfaces (variations in chemistry, composition, smoothness, etc.) on each of their half faces. The surface chemistry of the particle can be tuned to create amphiphilic particles such that one half of the particle is hydrophobic, while the other half is hydrophilic.[22] The surface charge on the Janus particle makes them repulsive and stable. However, introduction of salt in solution to screen the charge on colloidal particles leads to attraction between the hydrophobic faces of the Janus particle (because the particles are placed in an aqueous environment). This leads to directional bonding of the Janus particle and formation of clusters. Over time, these clusters merge together to form chain like structures called Bernal spirals.[23]

The addition of two patches to the same spherical particle leads to the formation of triblock patchy particles. Unlike Janus particles, triblock particles have two bonding sites and this results in the formation of 2D Kagome lattice crystalline structures.[24] Thus, the introduction of multiple clusters in the same particle results in the formation of open crystalline structures that

are not possible through the assembly of spherical particles. Methods are now being developed to synthesize particles with multiple patches that could potentially assemble into non-close packed 3D crystalline structures.[18,20]

#### 1.2.4.3 Shape and Interaction Anisotropy

The previous sections showed that spherical patchy particles can be assembled into ordered, open crystalline structures. Simulations have shown that shape anisotropic particles with patches can be assembled into complex clusters, ribbons and chains.[25] Preliminary experiments on shape anisotropic patchy particles have validated some of these simulation experiments.[26]

In this thesis, we synthesize and assemble complex colloidal particles with shape anisotropy as well as interaction anisotropy.

## 1.3 Colloidal Assembly in External Fields

Self-assembly has shown exciting potential to create complex structures from individual colloidal particles of the right size-scale in solution under appropriate conditions. However, self-assembly is limited by the time of assembly, monodispersity of particles and quality of overall ordering.[27] Further, the symmetry of self-assembled structures are limited by the synthesis methods available to create colloidal particles with complex interaction potentials. We classify external fields based on their potential to give two types of colloidal assemblies:

a. Field-assisted colloidal self-assemblies
b. Field-directed colloidal assemblies

### 1.3.1 Field-assisted colloidal self-assembly

The use of fields to improve self-assembly of colloidal particles is called field-assisted self-assembly. Fields can be used to influence self-assembly in three ways: (i) Fields can accelerate the kinetics of the self-assembly process. (ii) Fields can be used to create a gradient in volume fraction through the colloidal suspension to create co-existing liquid crystalline phases. (iii) External fields can be used to influence the onset of order-disorder transitions in the colloidal particle phase diagram.[28]

Examples of field-assisted self-assembly methods include spin-coating, gravitational fields and convective fields. For example, Shereda et al. show that spin coating can be used to increase the rate of crystallization and improve the quality of self-assembly of colloidal spheres into close-packed 3D structures.[29] Prevo et al. use convective assembly to create highly ordered 2D monolayers of colloidal spheres.[30] These methods show that colloidal spheres can be rapidly self-assembled into highly ordered close-packed colloidal crystals.

Anisotropic particles such as ellipsoids (rods) are harder to self-assemble because of their complicated Brownian dynamics. Recently, external fields have been used recently to rapidly induce order in colloidal rod suspensions. For example, spin coating was used to produce 2D orientationally ordered structures from ZnO nanorods.[31] Rapid self-assembly of colloidal rods using external fields has proven to be far more elusive. Mukhija and Solomon used gravitational fields (centrifugation) to induce order in colloidal ellipsoids.[32] However, in that study, the gravitational fields were too strong (body force on the colloidal particle was too high compared to Brownian forces) to give highly ordered and crystalline ellipsoid assemblies. Thus, new methods that can control the assembly forces on ellipsoidal anisotropic particles are needed. In

this thesis, we introduce direct current (DC) electric fields to rapidly self-assemble colloidal ellipsoids into ordered 3D structures.

#### 1.3.1.1 Direct Current (DC) Electric Fields

Low voltage (1-3V) DC electric fields have been used to assemble 2D and 3D colloidal crystalline structures. In aqueous solvents, application of DC electric fields leads to generation of electrohydrodynamic flows that cause deposition of particles at the electrode surface to form 2D crystalline structures.[33] In non-aqueous solvents, the DC electric field couples to the charge of the colloidal particle and drives the particle to the oppositely charged electrode.[34,35] This electrophoretic motion densifies the colloidal suspension. The primarily role of the DC electric field in this case is to control the concentration of colloids at the oppositely charged electrode and induce a phase transition. We design a new DC electric field device that permits direct visualization of the colloidal assembly process on the CLSM.

### 1.3.2 Field directed colloidal assembly

The use of fields to tune the interaction potential of colloidal particles and induce formation of ordered assemblies distinct from those obtained through self-assembly is called field directed colloidal assembly.[36] Alternating current (AC) electric fields and magnetic fields are two common methods to direct the assembly of colloidal particles.

AC electric fields can be used to create chains and 2D crystals from colloidal spheres.[37] Magnetic fields have also been used on spherical particles (polystyrene core, iron-oxide nanoparticle shell) to form chains.[38] Shape anisotropic particles show even more complex responses to AC electric fields as well as magnetic fields. Ellipsoids have formed zig-zag chains

at low concentrations and 2D centered rectangular structures at high concentrations on application of AC electric fields.[39] 'Peanut' hematite particles with permanent magnetic dipoles have formed kinked chains in 2D on application of magnetic fields.[40] Interaction anisotropic particles have also been assembled into highly complex assembly structures. Janus and patchy particles have formed staggered and double chains on application of AC electric fields or magnetic fields.[41,42] In this thesis, we use AC electric fields to assemble and reconfigure our shape anisotropic patchy particles

## 1.4 Organization of the Dissertation

This dissertation will be divided into two parts. The first part (Part 1) deals with DC electric field assisted self-assembly of colloidal particles. Part 2 deals with the synthesis, analysis and reconfigurable assembly of shape anisotropic patchy particles.

Specifically, Part 1 consists of Chapter 2, which demonstrates the 3D assembly of colloidal ellipsoids into 3D ordered crystalline phases. CLSM imaging and image-processing tools are used to analyze the experimental assembly structures and the results are compared to theoretical data available for the self-assmbly of colloidal ellipsoids. Chapter 3 describes the rapid assembly (~ 2 min) of nano-micron sized colloidal spheres (100 nm – 1.2 μm diameter) using DC electric fields. Structural color is obtained on assembly of 300 nm – 500 nm diameter colloidal spheres. CLSM imaging, spectrophotometry and light scattering are all tools used to analyze the assembly ordering.

Part 2 consists of Chapter 4 that describes the synthesis of patchy colloidal ellipsoid particles that have both shape and interaction anisotropy. CLSM imaging and image-processing tools were developed to recover all six degrees of freedom of patchy ellipsoidal particles to

analyze patch-patch binding in assembly structures. Chapter 5 describes the self-assembly of Janus ellipsoid particles into ordered chain-like structures. AC electric fields are subsequently used to reversibly reconfigure the ordering of the self-assembled chains.

We finally conclude our results and provide some future directions for research to expand the work presented in this thesis.

## 1.5. References


1. Russel, W. B.; Saville, D. A. & Schowalter, W. R. *Colloidal Dispersions* (Cambridge University Press, 1989).

2. Kaegi, R.; Ulrich, A.; Sinnet, B.; Vonbank, R.; Wichser, A.; Zuleeg, S.; Simmler, H.; Brunner, S.; Vonmont, H. & Burkhardt, M. Synthetic TiO2 nanoparticle emission from exterior facades into the aquatic environment. *Environmental Pollution* **156**, 233-239 (2008).

3. Whitesides, G. M. & Grzybowski, B. Self-assembly at all scales. *Science* **295**, 2418-2421 (2002).

4. Sali, A.; Shakhnovich, E. & Karplus, M. How does a protein fold? *Nature* **369**, 248-251 (1994).

5. Yim, M.; Shen, W.-M.; Salemi, B.; Rus, D.; Moll, M.; Lipson, H.; Klavins, E. & Chirikjian, G. S. Modular self-reconfigurable robot systems [grand challenges of robotics]. *Robotics & Automation Magazine, IEEE* **14**, 43-52 (2007).

6. Marlow, F.; Sharifi, P.; Brinkmann, R. & Mendive, C. Opals: status and prospects. *Angewandte Chemie International Edition* **48**, 6212-6233 (2009).

7. Pusey, P. N. & Van Megen, W. Phase behaviour of concentrated suspensions of nearly hard colloidal spheres. *Nature* **320**, 340-342 (1986).

8. Tretiakov, K. V. & Wojciechowski, K. W. Monte Carlo simulation of two-dimensional hard body systems with extreme values of the Poisson's ratio. *Physica Status Solidi (b)* **242**, 730-741 (2005).

9. Asakura, S. & Oosawa, F. On interaction between two bodies immersed in a solution of macromolecules. *The Journal of Chemical Physics* **22**, 1255-1256 (1954).

10. Leunissen, M. E.; Christova, C. G.; Hynninen, A.-P.; Royall, C. P.; Campbell, A. I.; Imhof, A.; Dijkstra, M.; Van Roij, R. & Van Blaaderen, A. Ionic colloidal crystals of oppositely charged particles. *Nature* **437**, 235-240 (2005).

11. Glotzer, S. C. & Solomon, M. J. Anisotropy of building blocks and their assembly into complex structures. *Nature Materials* **6**, 557-562 (2007).

12. Larson, R. G. *The Structure and Rheology of Complex Fluids* (Oxford university press New York, 1999).

13. Donev, A.; Cisse, I.; Sachs, D.; Variano, E. A.; Stillinger, F. H.; Connelly, R.; Torquato, S. & Chaikin, P. M. Improving the density of jammed disordered packings using ellipsoids. *Science* **303**, 990-993 (2004).

14. Champion, J. A. & Mitragotri, S. Role of target geometry in phagocytosis. *Proceedings of the National Academy of Sciences of the United States of America* **103**, 4930-4934 (2006).

15. Mukhija, D. & Solomon, M. J. Translational and rotational dynamics of colloidal rods by direct visualization with confocal microscopy. *Journal of Colloid and Interface Science* **314**, 98-106 (2007).

16. Mohraz, A. & Solomon, M. J. Gelation and internal dynamics of colloidal rod aggregates. *Journal of Colloid and Interface Science* **300**, 155-162 (2006).

17. Savenko, S. V. & Dijkstra, M. Sedimentation and multiphase equilibria in suspensions of colloidal hard rods. *Physical Review E* **70**, 051401 (2004).

18. Yi, G.-R.; Pine, D. J. & Sacanna, S. Recent progress on patchy colloids and their self-assembly. *Journal of Physics: Condensed Matter* **25**, 193101 (2013).

19. Zhang, Z. & Glotzer, S. C. Self-assembly of patchy particles. *Nano Letters* **4**, 1407-1413 (2004).

20. Mao, X.; Chen, Q. & Granick, S. Entropy favours open colloidal lattices. *Nature Materials* (2013).

21. Mitragotri, S. & Lahann, J. Physical approaches to biomaterial design. *Nature Materials* **8**, 15-23 (2009).

22. Chen, Q.; Yan, J.; Zhang, J.; Bae, S. C. & Granick, S. Janus and multiblock colloidal particles. *Langmuir* **28**, 13555-13561 (2012).

23. Chen, Q.; Whitmer, J. K.; Jiang, S.; Bae, S. C.; Luijten, E. & Granick, S. Supracolloidal reaction kinetics of Janus spheres. *Science* **331**, 199-202 (2011).

24. Chen, Q.; Bae, S. C. & Granick, S. Directed self-assembly of a colloidal kagome lattice. *Nature* **469**, 381-384 (2011).

25. Liu, Y.; Li, W.; Perez, T.; Gunton, J. D. & Brett, G. Self Assembly of Janus Ellipsoids. *Langmuir* **28**, 3-9 (2012).

26. Chaudhary, K.; Chen, Q.; Juarez, J. J.; Granick, S. & Lewis, J. A. Janus Colloidal Matchsticks. *Journal of the American Chemical Society* **0**, (0).

27. Whitesides, G. M. & Boncheva, M. Beyond molecules: Self-assembly of mesoscopic and macroscopic components. *Proceedings of the National Academy of Sciences* **99**, 4769-4774 (2002).

28. Mukhija, D. Measurement of rotational and translational diffusivities of colloidal rods in a highly viscous solvent with the help of CLSM Imaging. *Chemical Engineering, University of Michigan* 7-8

29. Shereda, L. T.; Larson, R. G. & Solomon, M. J. Local stress control of spatiotemporal ordering of colloidal crystals in complex flows. *Physical Review Letters* **101**, 038301 (2008).

30. Prevo, B. G. & Velev, O. D. Controlled, rapid deposition of structured coatings from micro-and nanoparticle suspensions. *Langmuir* **20**, 2099-2107 (2004).

31. Sun, B. & Sirringhaus, H. Surface tension and fluid flow driven self-assembly of ordered ZnO nanorod films for high-performance field effect transistors. *Journal of the American Chemical Society* **128**, 16231-16237 (2006).

32. Mukhija, D. & Solomon, M. J. Nematic order in suspensions of colloidal rods by application of a centrifugal field. *Soft Matter* **7**, 540-545 (2011).

33. Trau, M.; Saville, D. A. & Aksay, I. A. Field-induced layering of colloidal crystals. *Science* **272**, 706-709 (1996).

34. Rogach, A. L.; Kotov, N. A.; Koktysh, D. S.; Ostrander, J. W. & Ragoisha, G. A. Electrophoretic deposition of latex-based 3D colloidal photonic crystals: A technique for rapid production of high-quality opals. *Chemistry of Materials* **12**, 2721-2726 (2000).

35. Napolskii, K. S.; Sapoletova, N. A.; Gorozhankin, D. F.; Eliseev, A. A.; Chernyshov, D. Y.; Byelov, D. V.; Grigoryeva, N. A.; Mistonov, A. A.; Bouwman, W. G. & Kvashnina, K. O. Fabrication of artificial opals by electric-field-assisted vertical deposition. *Langmuir* **26**, 2346-2351 (2009).

36. Grzelczak, M.; Vermant, J.; Furst, E. M. & Liz-Marzán, L. M. Directed self-assembly of nanoparticles. *ACS Nano* **4**, 3591-3605 (2010).

37. Lumsdon, S. O.; Kaler, E. W. & Velev, O. D. Two-dimensional crystallization of microspheres by a coplanar AC electric field. *Langmuir* **20**, 2108-2116 (2004).

38. Bizdoaca, E. L.; Spasova, M.; Farle, M.; Hilgendorff, M. & Caruso, F. Magnetically directed self-assembly of submicron spheres with a Fe3O4 nanoparticle shell. *Journal of Magnetism and Magnetic Materials* **240**, 44-46 (2002).

39. Singh, J. P.; Lele, P. P.; Nettesheim, F.; Wagner, N. J. & Furst, E. M. One-and two-dimensional assembly of colloidal ellipsoids in ac electric fields. *Physical Review E* **79**, 050401 (2009).

40. Lee, S. H. & Liddell, C. M. Anisotropic magnetic colloids: a strategy to form complex structures using nonspherical building blocks. *Small* **5**, 1957-1962 (2009).

41. Gangwal, S.; Pawar, A.; Kretzschmar, I. & Velev, O. D. Programmed assembly of metallodielectric patchy particles in external AC electric fields. *Soft Matter* **6**, 1413-1418 (2010).

42. Ren, B.; Ruditskiy, A.; Song, J. H. & Kretzschmar, I. Assembly behavior of iron oxide-capped Janus particles in a magnetic field. *Langmuir* **28**, 1149-1156 (2011).

# Chapter 2

# Liquid Crystal Order in Colloidal Suspensions of Spheroidal Particles by Direct Current Electric Field Assembly


**Chapter Summary**

We use direct current (DC) electric fields to produce colloidal assemblies with orientational and layered positional order from a dilute suspension of spheroidal particles. These 3D assemblies, which can be visualized *in situ* by confocal microscopy, are achieved in short time spans ($t$ < 1 hour) by the application of a constant voltage across the capacitor-like device. This method yields denser and more ordered assemblies than had been previously reported with other assembly methods. We observed structures with a high degree of orientational order as well as layered positional order normal to the electrode surface. These colloidal structures are explained as a consequence of electrophoretic deposition and field-assisted assembly. We find the interplay between the deposition rate and the rotational Brownian motion to be critical to the optimal ordering, which occurs when these rates, as quantified by the Peclet number, are of order one. The results suggest that the mechanism leading to ordering is equilibrium self-assembly but with kinetics dramatically accelerated by the application of the DC electric field.[42]

## 2.1. Introduction

Anisotropic colloidal particles[1] have the potential to assemble into structures with complex symmetries, such as the bcc rotator phase[2], diamond[3,4] and other non-orthorhombic symmetries[5]. In addition, anisotropic particles can adopt preferential orientations on the lattice positions of these self-assembled crystals.[6] Such complex unit cells have applications in advanced optical materials.[7] Further, the orientational alignment of the anisotropic building blocks is also important for new forms of matter, such as metamaterials[1,8] and reconfigurable colloids[9]. Spheroids are simple anisotropic building blocks that may adopt both positional and orientational order in crystal structures. A practical advantage of using spheroids for experimental studies is their convenient production via syntheses based on the solidification of liquid droplets.[10-13]

For hard prolate spheroids, the classic simulations of Frenkel and Mulder found a progression of stability with increasing volume fraction from the isotropic phase, to the nematic phase, to an oriented crystal, with a unit cell having face-centered orthorhombic (FCO, uniaxial stretched FCC) symmetry.[6] The recent results of Pfleiderer and Schilling,[14] building on the packing simulations of Donev et al.,[15,16] have found a higher-density, entropically stabilized monoclinic phase. This phase breaks cubic symmetry and has a two spheroid centered monoclinic unit cell (mC2) mutually aligned at an angle that depends on the packing fraction of the suspension.[15] While further free-energy studies were done to quantify the self-assembly propensity of hard spheroids to the mC2 phase,[17] such systems have proved difficult to assemble rapidly.[18]

Although these structures are important targets for self-assembly and a number of them have been observed experimentally,[19] micron-scale rods with prolate spheroidal or cylindrical shape are difficult to self-assemble because of their slow translational and rotational Brownian

motion. For example, the isotropic-nematic transition can require more than 24 hours for cylindrical rods of length 180 nm[20] and simulations predict significant barriers to the nucleation of multilayer structures.[21] Thus, methods to accelerate the self-assembly of anisotropic colloids are required.

Analogous to methods to accelerate crystallization of spheres,[22-24] gravitational, electric, convective flow or shear fields may be applied to accelerate ordering in suspensions of anisotropic particles.[25] By varying the strength of the applied field, orientational order of colloidal rods was previously generated with an effective gravitational force generated by centrifugation.[18] However, in that study the field-strength was too large (Pe >> 1) to give high quality ordering or allow a direct connection to self-assembly. Electric fields are a promising alternative compared to centrifugation for field-assisted assembly, because they can be applied across a variety of geometries, including those compatible with *in situ* visualization of the assembly process.

To date, AC electric fields have been the predominant means to generate chains and 2D crystals from rods and spheres.[26-32] Such dielectrophoretic methods can be extended to yield 3D assemblies when the gap between the electrodes is thin.[30-31] AC electric fields require relatively high electric fields. In this paper we address the rapid assembly of prolate spheroidal colloids through the novel use of a direct current (DC) electric field-assisted assembly device. We characterize the assembled phases using confocal microscopy.

This method is based on the application of small electric fields generated by relatively low applied voltages (~ 1 – 3 V). The DC electric field couples to the charge monopole of the rods, generating electrophoretic motion of the particle.[24,33,34] This electrophoretic motion densifies the colloidal suspension at the electrode whose polarity is opposite to that of the

spheroidal particles. It is important to emphasize that the low voltage electric field does not align the spheroids, but rather provides a driving force towards denser configurations. The densification is sufficient to induce a phase transition that persists many (> 15) colloidal layers away from the electrode surface. We observe highly aligned nematic structures, as well as layered positional ordering of the prolate spheroids along an axis parallel to the electrode surface at the highest packing fraction.

## 2.2. Materials and Methods

### 2.2.1 Monodisperse Spheroid Synthesis:

We synthesized spheroidal PS particles by mechanically stretching 1.10 ± 0.02 μm diameter spherical carboxylate modified polystyrene (PS) particles (Fluospheres F8820, Invitrogen Inc) embedded in a polyvinyl alcohol (PVA, Sigma Aldrich, 30000-70000 molecular weight) matrix at a temperature above the glass transition of the spheres. PS microsphere solution in water (2 vol %, 300 μL) was mixed with PVA stock solution (10 wt% PVA, 7.5 mL). This mixture was allowed to dry overnight in flat omni trays. The trays were placed on leveling platforms to ensure thin film formation of uniform thickness. The dried films (thickness ~ 40 μm) were then pealed from the tray and cut into strips. These strips were placed in a custom stretching device, which was housed in an oven. The oven was heated to 120° C, which is above the glass transition temperature of polystyrene ($T_g$ ~ 100° C). This temperature was maintained for ~ 10 minutes to ensure uniform heating. An elongational strain of 2.5 was then applied to the films so as to obtain a final aspect ratio of 4.3. The stretched portions of the PVA strips were cut out and placed in distilled water for 24 hours to dissolve the PVA matrix, thereby releasing the spheroidal particles. The particles were dispersed in DMSO by solvent transfer to yield a

solution with an initial volume fraction ($f_i$) of 2.0 vol%. TBAC (0.1 mM, Fluka) was dissolved in DMSO to control the Debye length of the solution. The rod dimensions were characterized using a Scanning Electron Microscope (Philips XL-30). Zeta potential measurements were done for a dilute rod suspension (~ 0.5 vol%) using a Nano-ZS (Malvern Instruments) to calculate the charge on the colloidal particles.

### 2.2.2 Direct current electric field assembly device:

Thin glass cover slips (Fisher Scientific, 12545-G) were coated with a thin layer of indium tin oxide (ITO, ZC&R Inc). The ITO coating was sufficiently thin (~ 10 nm) that high quality confocal microscopy images could be acquired across the electrode. Two such cover slips were used to make the electric field device. To separate the electrodes, we created spacers from 1 mm thick microscope cover slips. We drilled a 1 cm hole in the center of the spacer to create a chamber for the colloidal suspension. We also glued T2 thermocouple wires (0.5 mm diameter, Goodfellow Inc) to the ITO coated cover slips using silver epoxy (MG Chemicals). This created a conductive connection to the ITO layer. We used UV curable glue (Light weld, Dymax Corporation) to glue the spacer between the two cover slips (ITO coating facing the solution side). A small (1 mm diameter) hole was drilled through the top electrode to allow solution to be injected into the sample chamber. We ensured that no air bubbles were present upon introduction of the colloidal suspension by slowly filling up the chamber and sealing the hole with a small piece of glass coated with vacuum grease. In this paper, the solvent for assembly was DMSO; however, experiments in solvents of different polarities (e.g. ethanol and a mixture of cyclohexylbromide-decalin) showed similar results.

### 2.2.3 *In situ* characterization of assembly structure and kinetics with confocal microscopy:

The electric field device was placed on the stage of a confocal laser-scanning microscope (Leica TCS SP2), and the leads were connected to a potentiostat (Autolab PGSTAT 128N). The cover slip directly above the objective was given a positive polarity, while the top cover slip was given a negative polarity. The potentiostat was programmed to apply a constant voltage across the colloidal suspension, while simultaneously measuring the resulting current density. We studied the kinetics of assembly in planes both parallel and perpendicular to the electrode surface, by taking images at a maximum of 0.657 seconds per frame using a 100X oil immersion objective (N.A. 1.4). The experiment was performed for at least 1 hour.

For some experiments, we added 1 wt% initiator (Irgacure 2100, Ciba Speciality) and 5 wt% photopolymer (trimethylolpropane triacrylate esters, Sartomer Inc) to enable immobilization of the assembled structures by photopolymerization.[22] Photopolymerization was performed for samples with low voltages, which formed diffuse assemblies whose structure could not be captured for successful image processing without photopolymerization. We activated the photopolymer using UV light after a steady-state assembly had been obtained. The photopolymer immobilized the structure within less than 1 s and had a negligible effect on the Debye length and the zeta potential (data not shown).

### 2.2.4 Quantitative image processing and structural characterization of CLSM image volumes

For characterization of the self-assembled structures by image processing, we acquired image volumes of size 19.63 x 19.63 x 2.5 $\mu m^3$. The voxel size was 38.3 x 38.3 x 38.4 $nm^3$.

These stacks were representative of near wall local order in a particular region. Image processing was used to identify the centroids and directors of all rods in the image volume.[13] Briefly, after a Gaussian filer had been applied, the program automatically identified the central backbone of the rods as the brightest pixels within a local region of order the half-width of the rod. These backbone pixels were identified as individual rods by cluster analysis. The centroid and the orientation angles of each rod were computed from the set of backbone clusters. The variation in centroidal density from the coverslip was reported in Figure 7 as a function volume fraction. All the orientation angles identified were used to compute the S given by equation (7) and as shown in Figure 6. We tested the method by comparing the number of particles identified in a specified volume to the known macroscopic volume fraction, as determined by sample weight. The relative error in number of particles identified was 1.5%. Moreover, rod backbones identified by the algorithm were overlaid on Gaussian filtered images to check for the fidelity of the centroidal location and the orientation of the identified backbone. Additional details of the performance of the image processing are available in Dzul et al.[48]

**2.3. Results**

We directly visualize the assembly of polystyrene (PS) spheroidal particles of aspect ratio 4.3 ± 0.6 (major axis $L$ = 3.35 ± 0.41 μm and a minor axis $D$ = 0.79 mm ± 0.07 mm). The particles are relatively uniform in size and shape, as shown in the scanning electron micrograph of Figure 2-1. They were produced by uniaxial deformation of PS spheres embedded in an elastomeric film (cf Methods). We use the electrolyte tetrabutylammonium chloride (TBAC, 0.1 MM) to screen the electrostatic interactions between the particles. The Debye length ($k^{-1}$) was found to be 23.9 nm from a conductivity measurement of the system (3.45 μS/cm). For some

measurements, a small amount of photopolymer and initiator was added to the solvent to allow the assembled structure to be immobilized by UV-induced photopolymerization for further direct visualization studies (cf Methods). The z-potential of the colloids at the conditions of the experiments was measured to be -38 ± 12 mV.

A small volume (~ 35 mL) of the colloidal rod suspension at an initial volume fraction $f_i$ = 2.0% was placed between parallel planar electrodes (indium tin oxide coated on glass coverslips) held at a separation of 1.15 mm with a glass spacer. The cross-sectional area available for assembly was 19.6 $mm^2$. The device, which resembles a parallel-plate capacitor, was mounted on the stage of a confocal laser scanning microscope (CLSM, Leica TCS-SP2) for *in situ* visualization with an NA=1.4 oil immersion objective. The two electrodes were connected to a potentiostat (Autolab PGSTAT 128N), which applied a constant voltage and measured the resultant current density. A schematic of the device is shown in Figure 2-2a. Images of the assembled cell and the area available for self-assembly are shown in Figures 2-2b and 2-2c. Representative confocal microscopy images of self-assembled structures obtained *in situ* are shown for field of views of 161 x 161 $mm^2$ (Figure 2-2d) and 19 x 19 $mm^2$ (Figure 2-2e).

We tested the device using spherical particles to create a 3D close packed crystal consistent with earlier reports that used similar methods.[24,34] We used the electric field device described in the main text to form colloidal crystals of spheres, and compared the results with previous reports that used different particle and solvent systems. For an applied voltage of 0.66 V, a suspension of 1.4 mm poly(dimethylsiloxane) stabilized poly(methyl methacrylate) spheres[3] in cyclohexylbromide and decalin (68:32 wt%) formed a dense multilayer colloidal crystal. High-quality positional ordering is apparent from CLSM images of the colloidal structure in a plane parallel to the electrode surface (Figure 2-3a; the plane depicted is the first colloid layer

above the electrode) and in a perpendicular plane (Figure 2-3b; this image shows multilayer ordering at least up to ~ 40 mm from the electrode surface). These close packed colloidal crystals formed rapidly ($t$ < 1 hr) and persisted while the constant voltage was applied. When the applied voltage was removed, the ordered array melted and the colloidal particles diffused from the electrode until an apparently homogeneous concentration between the electrode gap was achieved. Although small regions of the self-assembly are shown in Figure 2-3 and the subsequent figures, confocal imaging at multiple points in the specimen showed that the crystal structure of the electrodeposited colloids was uniform across the full 19.6 $mm^2$ cross sectioned area of the gap.

We then introduced spheroidal particles at an initial volume fraction of 2.0%. On application of a constant DC voltage, the negatively charged spheroids migrated towards the positively charged electrode. The transient densification of the PS rods in dimethyl sulfoxide (DMSO) was observed at the coverslip by imaging at 1.4 fps using the CLSM. Images that characterize the kinetics of rod assembly are shown in Figure 2-4 and in Supplemental Movie 1 (SM1). Figure 2-4a shows that the sample was initially unaligned and at a low volume fraction. The densification process began upon application of the constant voltage. After about 3 minutes (Figure 2-4b), the first regions of enhanced rod concentration were observed, although these regions are still largely disordered both in position and orientation. SM1 shows that the enhancement of colloidal density was due to particles moving into the image focal plane (from above). Supplemental Movie 2 (SM2) shows the rod assembly under the same conditions as Figure 2-4 and SM1, but visualized in a plane perpendicular to the electrode surface. SM2 also shows that the increase in colloidal density at the electrode surface is due to the migration of rods toward the electrode surface from the bulk of the sample.

For 1.5 min < $t$ < 7 min, the sample continued to densify over time as the regions of concentrated disorder grew (Figure 2-4c). Even though densification of the rods due to deposition occurred in this period, the rods remained highly mobile due to Brownian translations and rotations at this voltage and volume fraction (cf SM1).

The rod suspension showed significant alignment (Figure 2-4d) at $t$ ~ 11min which persisted until the conclusion of the experiment ($t$~ 1.5 hr). The structure of the suspension appeared visually to be nematic, with a domain texture visible on scales of 5 mm. SM2 indicates that the orientational order extends at least 8 mm into the specimen. We further observed ordering up to at least 15 mm into the sample by imaging the suspension at the highest excitation power of the CLSM. This distance is at the limit for imaging in this system, given the refractive-index contrast between the PS particles and the DMSO solvent. Ordering may have continued above this distance; however, it could no longer be observed in this particular colloid/solvent system.

Figure 2-5 shows the effect of different applied voltages on the rod assemblies. The samples were imaged at the surface of the positive electrode after at least 1 hr. This time was sufficient for the system to reach a steady-state structure, as per the kinetics reported previously in Figure 2-4.

Figures 2-5a and 2-5b show that this structure is orientationally and positionally disordered at applied voltages of 1.0 V and 1.25 V. (Regions of the images with radially symmetric intensity resembling that of a sphere are actually rods oriented perpendicular to the image plane and electrode surface.) Moreover, at these applied voltages, the rod assemblies were highly mobile due to Brownian motion. The solvent of these specimens was photopolymerized during assembly to lock in the structure prior to 3D CLSM imaging. This

procedure made quantification of order possible in these highly mobile assemblies (cf Methods). Figure 2-5c shows that an applied voltage of 1.5 V results in a much denser colloidal phase at the electrode surface than that observed for the lower applied voltages, with some aligned domains. However, the layers further above the electrode (not apparent in Figure 2-5c) are more disordered and diffuse.

In Figures 2-5d and 2-5e, we show assemblies with a high degree of alignment for applied voltages of 1.80 V and 1.85 V, respectively. Here, the effect of the applied voltage was sufficient to support significant densification of the colloidal particles at the electrode surface.

As the applied voltage was increased to 2 V, small domains of order were evident (Figure 2-5f), but there was no large-scale order. At 2.5 V and 3.0 V, the rods appeared jammed, with limited mobility due to the rapid densification caused by the high initial voltage. Moreover, the assemblies in Figures 2-5g and 2-5h do not show significant orientational or positional order.

Thus, variation of the applied voltage results in a series of reversible transitions among assemblies of colloidal spheroids. Lower applied voltages (< 1.75 V) lead to fluids with orientational disorder. At intermediate applied voltages, nematic order as well as positional order is observed along an axis perpendicular to the electrode surface. Lastly, at large voltages (> 2.5 V), a jammed, disordered packing of rods is formed.

We explain the rich assembly behavior in Figure 2-5 by investigating the effects of the electric field on the colloidal suspension. A spatially varying external field leads to a gradient in the osmotic pressure of the solution.[35,36] Thus, the force due to the DC electric field is balanced by the gradient in osmotic pressure according to

$$\frac{d\Pi(z)}{dz} = -\frac{F_e}{V_p}\Phi(z)\,. \qquad \textbf{(1)}$$

Here, Π($z$) is the osmotic pressure as a function of the distance z from the electrode surface, $F_e$ is the external force on the spheroid due to the DC electric field, $V_p$ is the volume of the prolate spheroid, and F($z$) is the volume fraction of rods at that height. In a semi-infinite medium, integration of Equation (1) and application of the boundary condition $\Pi(z \to \infty) = 0$ yields the osmotic pressure at the base of the sample[35]

$$\boldsymbol{\Pi(z=0) = -\frac{F_e H}{V_p}\phi_i}\,. \qquad \textbf{(2)}$$

We calculate the electrophoretic mobility of a particle in the thin Debye layer limit ($\kappa R \to \infty$). Here, κ is the debye length and R is the smallest particle radial dimension. We begin by assuming the applied field 'E' in the capacitor is small compared to the field due to the particle double layer. The forces acting on the particle are the retarding drag of the particle, and the electrostatic force coupled with the hydrodynamic interactions of the ions. Thus, the force balance is: [37]

$$\mathbf{F}_e = \mathbf{F}_d = -[\int_{V_f} \varepsilon \nabla^2 \varphi \frac{\partial \phi}{\partial x} dV]\,\mathbf{E} + [\int_{V_f} \varepsilon \mathbf{u}_r \nabla^2 \varphi \frac{\partial \phi}{\partial x} dV]\,\mathbf{E} = \mu \mathbf{A}_r \cdot \mathbf{U}\ , \qquad \textbf{(3)}$$

where $\mathbf{A}_r$ is the resistance matrix for the particle. The resistance matrix incorporates information of the shape of the particle.[37], [50] $\phi$ , $\varphi$ are the potentials induced by the ambient field and double layer around the spheroid, respectively, μ is the solvent viscosity and $\mathbf{u}_r$ represents the disturbance flow field. To solve for the mobility u, one needs to solve two boundary value problems in $f$ and $\varphi$ with the disturbance velocity field $\mathbf{u}_r$. [50], [51]. We get

$$4\pi\mu \mathbf{A}_r \cdot \mathbf{U} = 4\pi\varepsilon\varphi_o \mathbf{A}_r \cdot \mathbf{E} \qquad \textbf{(4)}$$

Thus, when $\kappa R \rightarrow \infty$, the resistance matrix cancels out on both sides. Now, with the boundary condition of constant surface potential $\varphi_0 \rightarrow \zeta$, which gives rise to the familiar form of the electrophoretic mobility

$$u_s = \frac{\varepsilon \zeta}{\mu} E \ , \tag{5}$$

where, $\zeta$ is the zeta potential of the spheriod.

The force due to the electric field is given by,

$$F_e = \varepsilon \varepsilon_0 E \zeta A_r \tag{6}$$

The force acting on a prolate spheroid with a thin debye layer is given by equation (6). The resistance matrix ($A_r$) for a prolate spheroid is given by,

$$A_r = \frac{128\Pi}{3(4\chi + L^2\alpha_1)} + \frac{32\Pi}{3(\chi + R^2\alpha_2)}$$

$$\alpha_1 = \frac{4}{L^2 e^2}(\chi - \frac{4}{L})$$

$$\alpha_2 = \frac{2}{Le^2}(\frac{1}{R^2} - \frac{\chi}{L})$$

$$\chi = \frac{4}{Le} \mathrm{Ln}(\frac{L}{R}(1+e))$$

$$e = \sqrt{1 + \frac{R^2}{L^2}}$$

Here, L is the major axis length of the spheroid and R is the minor axis radius.

To include effects of our finite debye length, we use the asymptotic expansion by O'Brien and Ward[8] in the limit of thin Debye lengths ($\kappa R >> 1$) to calculate the mobility of a prolate ellipsoid.

In this expansion, the electrophoretic mobility is written in terms of $\beta$ and the deviation with respect to the Smoluchowski limit decays with $1/\kappa R$.

$$\beta \sim \frac{e^{|\bar{z}|/2}}{\kappa R}, \tag{7}$$

with $\bar{z} = ez\zeta/kT$. Here, e is the electronic charge, z is the charge number, k is the Boltzmann constant and T is the temperature. For our experimental conditions, $\beta \approx 0.13$

For $\beta << 1$, the mobility is

$$u = \frac{e\zeta}{\mu} E - \frac{\varepsilon kT}{3e\mu}\left(\bar{z} - \frac{2}{z}\ln 2\right)[f^{\parallel}(\beta) + 2f^{\perp}(\beta)]\, E, \tag{8}$$

where $f^{\parallel}(\beta)$ and $f^{\perp}(\beta)$ are the geometric factors for the aligned and transverse cases, respectively. We note that when $\kappa R \to \infty$, $f^{\parallel}(0) = f^{\perp}(0) = 0$. Finally, if we scale $u/u_s$, we can write a scaled dimensionless mobility that approaches unity at the Smoluchowski limit.

For our assembly conditions the scaled mobility is $u/u_s = 0.95 \pm 0.11$. Thus, we can conclude that our spheroids have sufficiently low surface potential and thin Debye layer such that the shape of the ellipsoid does not have a significant effect on the mobility and the force in comparison to the Smoluchowski limit. Although, we note that the mobility is strongly dependent on the surface potential of the spheroid and such that relatively small changes in z can have significant effects upon the retardation forces. For our system, we are safely within the Smoluchowski limit and calculations of the spheroidal Peclet numbers and forces are calculated in that limit.

In the Smoluchowski limit we can directly write $F_e = \varepsilon\varepsilon_0\zeta\langle A_r\rangle E$, where z is the zeta potential and $\langle A_r \rangle$ is the shape factor given in the SI.[37] The effective electric field in the solution between the electrodes can be calculated through direct measurement of the current density for

all the conditions reported in Figure 2-6. We neglected concentration polarization in calculating the effective electric field because we estimate that it is small relative to the voltages applied. For all electrode geometries, measured current density relates to the bulk electric field through:[38]

$$\boldsymbol{E} = \frac{\boldsymbol{i}}{\lambda_0}, \tag{9}$$

where $\boldsymbol{i}$ is the current density (per area of electrode) generated in the device and $\lambda_0$ is the ionic conductivity of the solution

Results of the potentiostat measurements are reported in Figure 2-7. The measurements reported are for particle-free experiments, where $\boldsymbol{i}$ is measured in a test cell containing DMSO solvent and salt (TBAC). No significant differences in $\boldsymbol{i}$ were found using a 0.5 vol% solution of colloidal spheres or a 2.0 vol% solution of colloidal rods (data not shown). Measurements were conducted for 1000 s, the period required to generate steady-state assemblies in the device, as reported in Figure 2-4.

In Figure 2-7, for low applied voltages (1.0 V, 1.25 V), the current density generated was small (< 0.5 μA/cm$^2$). The current density at 5 s corresponds to an effective field of 0.15 V/cm. For intermediate field strengths (1.5 V, 1.8 V, 1.85 V, 2.0 V), the current generated increased with voltage and was at least 10 times higher than measured for small field strengths ($\boldsymbol{i}$ =5 μA/cm$^2$). The effective field for this range of applied voltages was ~ 1.5 V/cm. At the highest field strengths of 2.5 V and 3.0 V, large initial current densities were observed (> 10 μA/cm$^2$) and the effective field for these experiments was 7.5 V/cm for the initial currents.

The trends in Figure 2-7 are crucial to the understanding of the rod assembly experiments shown in Figure 2-5. First, the current is a monotonically increasing function of the applied voltage. This increase is expected from electrochemical kinetics, where current increases exponentially with voltage for the case of an electrode surface reaction.[38] Further, at each applied

voltage, the current progressively decreases over the duration of the experiment. This is consistent with electrochemical transport theories, in which $\boldsymbol{i}$ decreases with time for a fixed voltage due to mass transfer transients in the diffusion layer near the electrodes and depletion of the reactant in the bulk solution.[38] Although a steady-state current density is not achieved, $\boldsymbol{i}$ stabilizes into a slow decay by t = 100 s. This stabilization is faster than the kinetics of the assembly experiments that led to the results in Figures 2-4 and 2-5. At high voltages (2.5 V, 3.0 V), the steady state is achieved at later times ($t$ > 800s) and most of the deposition and assembly has already occurred by this time. Although the range of voltages used varied only between 1.0 V – 3.0 V, the difference in $\boldsymbol{i}$ (and thus effective fields) generated under these conditions varied by more than three orders of magnitude. The driving force due to the electric field experienced by the rod colloids is thus an extremely sensitive function of the applied voltage.

We find that the primary mechanism for the enhanced number density of colloids at the electrode surface is electrophoresis. DC electric fields are known to cause bulk fluid flows, which have an effect on particle mobility.[33,39] To evaluate the possible significance of these previously reported fluid flows for our experiments, we applied a constant voltage across a test suspension of dilute spherical PS particles. The time-dependent displacement of the spheres (s = 1.1 μm) was quantified by means of image processing and trajectory linking algorithms (cf Methods). In the Smoluchowski limit, the electrophoretic mobility $U$ is proportional the magnitude of the electric field $E$=|$\boldsymbol{E}$|

$$\boldsymbol{U = \frac{\varepsilon \varepsilon_0 \zeta E}{\eta}}, \qquad \textbf{(10)}$$

where ε is the dielectric constant of the solvent, $\varepsilon_0$ is the permittivity of free space, ζ is the zeta potential, and η is the viscosity of the solution.

Equations (9) and (10) can be used to calculate the expected electrophoretic mobility from the measured current density and standard electrokinetic theory appropriate to the screening length of our system in the Smoluchowski limit. Our hypothesis is that the electrophoretic mobility of the particles in the DC electric field causes the suspension to densify at the electrode. To evaluate this claim, we tracked the electric-field induced displacement of dilute suspensions of charged spheres in our device as a function of time, and compared to the predicted mobility based on a simultaneous measurement of the current. We used a 0.5-vol% spherical PS particle solution suspended in DMSO. The diameter of the spheres was 1.10 μm and the measured zeta potential was -41 ± 11 mV. This solution was introduced in our device, which was connected to a potentiostat and placed on a confocal microscope stage. We applied an external voltage of 2.75 V, while simultaneously acquiring a time series of images at the rate of 1.4 fps in a plane parallel to the direction of the electric field (perpendicular to the electrode). The particles moved to the oppositely charged electrode, and the current was simultaneously recorded by the potentiostat.

We experimentally calculated the particle velocity due to the applied voltage by using particle-tracking algorithms based on the methods of Crocker and Grier.[49] Particles suspended in DMSO without an applied electric field were confirmed to exhibit Brownian motion. In contrast, when the electric field was applied, the particles experienced motion due to electrophoretic force as well as random Brownian motion. The mean displacement in the direction of the field was calculated for every 5 frames (2.6 s), and then converted to an instantaneous mean velocity, to yield the instantaneous velocity over the duration of the experiment. The experimental mobility showed fluctuations due to random Brownian motion. From the measured current we computed the electric field to which the particles were subjected using equation 2. We then calculated the particle velocity (u) for the particles, which have a thin Debye layer, using Smoluchowski's

mobility equation (Equation 3 in the main text). As discussed in the main text, the experimental and theoretical electrophoretic velocities agreed well over the full duration of the experiment; the average variability was 11% as in Figure 2-2. Thus, electrophoretic deposition was the dominant mechanism of motion due to the external electric field.

Thus, in our hypothesis, the electric field has an effect on the colloidal rod trajectories only to the extent that the electrophoretic displacement is dominant relative to the random motion of the rods due to rotational and translational Brownian motion. This physical idea allows us to parameterize the strength of the electric field by means of the Peclet number (Pe), which can be interpreted as a ratio of the spheroid's characteristic rates of motion. In this work, Pe is the ratio of the rate of displacement of the colloid in the applied field to the rate of Brownian motion, evaluated at the scale of the longest dimension of the particle. Thus,

$$\mathbf{Pe} = \frac{U/L}{D_r} = \frac{\varepsilon\varepsilon_0\zeta E}{\eta L D_r}, \qquad \textbf{(11)}$$

where $D_r$ is the rotational diffusivity, and again $L$ is the length of the spheroid's major axis. The Pe is independent of viscosity because both the electrophoretic velocity and rotational diffusivity are inversely proportional to the viscosity,.

From the theory of Brenner[40], we compute the rotational diffusivity of the prolate spheroids to be $D_r = 0.08 \pm 0.02$ s$^{-1}$. The (time-dependent) Pe computed from the measured $\boldsymbol{i}$ for each of the constant-voltage experiments is reported in Figure 2-7.

In order to investigate trends in self-assembly with Pe, we take its value at a time of 100 s as characteristic of that applied voltage. Although a full analysis would account for the temporal evolution of Pe, the selection of Pe ($t$ = 100 s) as a characteristic value is supported in two ways. First, the time-dependent $\boldsymbol{i}$ (t) (and thus Pe) had typically stabilized at nearly its steady-state value by t = 100 s for all voltages other than 2.5 V and 3 V. Excluding these voltages, the

measured $\boldsymbol{i}$ (and Pe) decreased on average by a factor of about 2.5 between $t$ = 100 s and $t$ = 1000 s. This change is much smaller than the initial change of greater than a factor of 10 between $t$ = 0 s and $t$ = 100 s. Second, the steady-state structures observed in Figure 4 were all achieved within the window of 100 s < $t$ < 1000 s. Even though a steady state is not reached in this time range for high voltages (2.5 V, 3.0 V), most of the assembly is complete due to the enhanced deposition rate. Thus, in subsequent figures we report Pe at $t$ = 100 s as characteristic of the conditions for self-assembly. Understanding the specific effect of the time-dependence of the Pe would be of interest, but is beyond the scope of the current study.

By comparing the results of Figures 2-5 and 2-7, it is clear that the electric field was not sufficiently strong to densify the suspensions to the order-disorder transition for Pe < 0.1. Conversely, for Pe > 1, the motion due to the applied field dominated over the randomizing effects of Brownian motion and as a result, the particles had insufficient mobility to organize into orientationally ordered structures. Instead, orientationally and positionally ordered structures are only observed for Pe ~ 1, when rapid densification is still observed at the coverslip, but rotational and translational Brownian motions are still possible, thus permitting equilibration into ordered phases.

We used image-processing (IP) algorithms to quantify the observed ordering by identifying the centroids and orientation angles of all the rods in image volumes as acquired by confocal microscopy (cf Methods).[13] The volume imaged was 19.7 x 19.7 x 2.5 $mm^3$. It extended out into the specimen from the positive electrode surface. We quantified the volume fraction for our assembly structures in the near-wall region (z < 2.5 mm) from the rods identified by image processing. From Figure 2-8a, the volume fraction is initially an increasing function of Pe. For Pe < 0.1, the colloidal volume fraction is well below the phase transition. The volume fraction

exceeds the phase transition coexistence region at Pe ~ 1 and stays nearly constant for the jammed structures obtained for Pe > 1.

We compare our assembly to that predicted by the theory of simple field-assisted assembly of Equations (1) and (2). The theory predicts the sediment volume fraction and order parameter to be a consequence of the osmotic pressure built up in the sample so as to balance the force applied to the colloids by the electric field. In this case, we can write an implicit equation connecting the spheroid volume fraction to the Pe, through calculation of the osmotic pressure:

$$\mathbf{Pe} = \frac{\mathbf{\Pi}(z)V_p}{\langle A_r \rangle \varphi_i H \eta L D_r}\,. \qquad \mathbf{(12)}$$

The simulations of Tjipto-Margo and Evans[41] report the osmotic pressure as a function of the volume fraction for a system of hard spheroids. With these results and Equation (6), we compute and plot the predicted dependence of the assembly volume fraction on the applied Pe. When compared to this field assisted self-assembly theory, we find that the experiments require an order of magnitude greater Pe than theoretically predicted to attain the volume fraction required for nematic order, as shown in Figure 2-8a.

We also computed the nematic order parameter *S* to quantify the quality of the orientational ordering. *S* is the largest eigenvalue of the orientation angle tensor, **Q**, of all the rods in the image volume.

$$\mathbf{Q} = \frac{1}{2n_r}\sum_{i=1}^{n_r} 3\mathbf{d}_i\mathbf{d}_i - \mathbf{I}\,, \qquad \mathbf{(13)}$$

where $n_r$ is the number of rods in the image volume, $\mathbf{d}_i$ is the director specifying the orientation angle of the $i^{th}$ rod and **I** is the identity tensor. S varies from 0 (complete orientational disorder) to 1 (full orientational order).

As is evident from Figure 2-8b, $S < 0.4$ for low dimensionless applied fields (Pe < 0.1). This quantification agrees well with the images reported in Figures 2-5a-c (Fig 4c shows small

nematic domains in the colloidal layer immediately above the coverslip. However, the order parameter in these volumes is low because there is no overall 3D orientational order). Significant rod alignment ($S > 0.6$) was found for the intermediate Pe, again in good agreement with the images of Figures 2-5d and 2-5e. Structures with partial alignment ($S = 0.42$) were observed at the still higher applied voltage corresponding to Pe = 2.5 (see Figure 2-5f). Finally, we observe structures with small orientational order and glassy dynamics for Pe > 10. These conditions lead to low order parameter measurements ($S < 0.4$). In summary, through the calculation of S, the best rod orientational ordering was observed for Pe~1 where the electrophoresis driving force is comparable to that of Brownian motion.

The order parameter for a given volume fraction of a self-assembling system of hard rods is also available from Tjipto-Margo and Evans.[41] We use their data together with Equation (6) to predict the expected field-assisted assembly order parameters as a function of Pe. We find that the experimental order parameters are nearly as large as the theory predicts, but the Pe required to attain nematic ordering is ~ 10 times greater for the experiments than for the theory.

Thus, volume fraction and order parameter are highly correlated and consistent with equilibrium thermodynamics. However, the field strengths necessary to densify and align colloidal suspensions are about an order of magnitude greater than predicted by the simple theory of Equations (1) and (2) predicts. A similar discrepancy was reported by Mukhija and Solomon[18] for the case of an effective gravitational field generated due to centrifugation.

The experiments and image processing also yield the centroid locations of all the rods in the image volume. We show an example image volume at 1.85V in Figure 2-9a that is highly ordered and from which the centroid locations were taken. From these data, we calculate the density distribution as a function of height (z-axis). The density plot in Figure 2-9b shows a

periodic rod density at 0.5D indicating alternating layered structure. A simple structure that has such a periodicity is a body-centered tetragonal (BCT) lattice (e.g. Figure 2-9c). We further investigate the periodicity of assembly via the static structure factor S(q) for the assembly experiments along the normal (z-axis) to the electrode surface and compare them to the Bragg peaks of the BCT lattice. We calculate the S(q) over a range of wavenumbers along the $q_z$ reciprocal lattice from the centroid data. We observe a strong peak at $q_z = 12.3/D$ (Figure 2-9d), which corresponds to spacing of 0.51D. This peak indicates the presence of layered positional order in the sample along an axis normal to the electrode surface. The layers are periodically arranged at a distance of about half the minor axis width of the rods or 0.5D. We note that the diminished higher harmonics in S(q) of the data is due, in part, to separate oriented domains. If we restrict the scattering to specific domains we see an emergence of a harmonic peak at $q_z \approx 25/D$. At both lower and higher Pe, diffuse and jammed structures did not show such positional order.

For comparison, we created representative renderings of the known spheroidal assemblies predicted by self-assembly simulations, shown in Figures 2-9e, 2-9f and 2-9g. Possible structures that might include layered ordering and be consistent with the measured volume fraction of 49% are the smectic C phase with an interlayer distance of the minor axis (D) (Figure 2-9e), face-centered orthorhombic (FCO) as simulated by Frenkel and Mulder[6] with an interlayer distance of 0.92D (Figure 2-9f), and the monoclinic spheroidal mC2 phase of Pfleiderer and Schilling[14] with an interlayer distance of 0.6D (Figure 2-9g). A rendering of a body-centered tetragonal (BCT) phase that is consistent with experiments showing positional ordering is shown in Figure 2-9h. In particular, the render shows a layer spacing of ~ 0.5D, a high order parameter (S =1), and a volume fraction of 49%. We remark that the spacing of the mC2 phase rendered in Figure 2-9g

could be consistent with the experiments (Figure 2-9b) yet require higher densities to form than were achieved in the experiments.

### 2.4. Discussion

The application of a DC electric field across a colloidal suspension of polystyrene spheroidal particles dispersed in DMSO led to a rapid increase in concentration of the particles at the oppositely charged electrode surface (< 1 hour). At low voltages, the electric field induced the formation of diffuse, disordered structures of the rods. At intermediate voltages the volume fraction was high enough and the kinetics of the assembly sufficiently favorable that large-scale nematic structures with high orientational order formed. Finally, at high voltages, although the volume fraction was high, the kinetics of the assembly did not lead to equilibration into large-scale ordered structures, and disordered glassy structures formed instead. The experiments require a greater field strength to achieve a given order parameter and volume fraction than a simple theory of field-assisted assembly predicts. We experimentally verified that the primary effect of the DC field was to facilitate rapid concentration of an initially low volume fraction sample of spheroids. This concentrating effect was sufficient to induce equilibrium phase transitions. The densest assembly displayed phases with high orientational order ($S = 0.77 \pm 0.06$) and positional ordering consistent with efficient packings of spheroids. The order parameters reported in this paper are comparable or better to previous literature reports. For example, Mukhija and Solomon, using rigid rods of a similar aspect ratio, reported a best order parameter of 0.58 by the method of centrifugation. A very high order parameter ($S \sim 0.85$) for rod shaped colloidal particles was reported by Dogic et al. for the case of semi-flexible fd virus rods and a depleting polymer at high aspect ratios (~ 130) [42] This discussion section focuses on

the electrochemical mechanism that drives the electrophoresis, as well as the action of the electric field in facilitating the self-assembly. The unexpected lateral positional order observed for some of our samples is also discussed.

DC electric fields can lead to electrohydrodynamic flows[33] and electro-osmotic flows[39] in addition to the electrophoretic motion of the colloids themselves. Each effect can influence the structure of the final assembly. For example, Trau et al.[33] reported that electrohydrodynamic flows lead to lateral motion of the particles along the electrode surface, which leads to formation of 2D aggregates that crystallized over time. By contrast, in our system, direct visualization by CLSM in planes both parallel and perpendicular to the electrode surface showed no significant lateral motion of colloids. Instead, the principal observed motion was perpendicular to the electrode surface, consistent with electrophoresis.

The observed electrophoretic motion is driven by an electric field, the magnitude of which is proportional to the current density across the gap between the electrodes. The current density is not created by double-layer charging, since the millisecond time scale for developing the double layer is much faster than the observed relaxation of ***i***. Instead, the exponential increase in ***i*** with applied voltage as seen in Figure 2-7 is consistent with a Faradaic process at the electrode, i.e. a heterogeneous chemical reaction. Depletion of the reactant undergoing this chemical reaction sets up ionic mass transfer toward the electrode, which leads to the observed ***i***. The observed decay of ***i*** over time for an applied voltage is consistent with the reactants diffusing to the electrode surface. It is our hypothesis that dissolved oxygen and/or water in our solvent are the reactants that ultimately drive the field-assisted assembly process. For example, a 5 $\mu A/cm^2$ current density would require a dissolved impurity concentration of ~ 1 mM.[38] This concentration is reasonable: for example, oxygen dissolved in DMSO is ~ 0.75 mM.[43] Further, ***i***

decreases as the available concentration of reactants is depleted at the electrode due to the chemical reaction and mass-transfer limited diffusion of reactants from the bulk. Thus, the depletion of residual reactants from the cell due to the electrode reaction explains the time dependence of the measured current reported in Figure 2-7.

We attempted to affect the electric field driving force for assembly by changing the concentration of water and dissolved oxygen in the assembly device. The experiment was conducted in a glove box where the oxygen had been purged from anhydrous DMSO. In this case, the current density generated upon application of a constant 2.75 V in the solvent was at least a factor of 8 less than reported at the same voltage in Figure 2-7. The lower ***i*** is explained by the lower concentration of oxygen and water reactants, which had been partially removed from the system. This further justifies our hypothesis that oxygen and water are the reactants responsible for the evolution of current in the system.

In Figure 2-8, we compare the measured equation of state in our field-assisted assembly system using the relation of Equation (1) to that of an equilibrium simulation of hard prolate-spheroids. The Pe required to generate the reported volume fractions and order parameters at the cover slip in the experiments were ~ 10 times larger than the theory predicted. This discrepancy was observed earlier for colloidal rods assembled using the centrifugal force (although it was more pronounced in that case).[18] In the present work, the theory was able to predict the sharp increase in experimental order parameters near the nematic order-disorder transition volume fraction. Further, there was an excellent correlation between the observed volume fraction and order parameters with volume fractions and order parameters calculated theoretically. Thus, even though the external force needed to assemble ordered structures was larger than expected, the behavior of colloids in the DC electric field device is consistent with a mechanism of self-

assembly and equilibrium phase transitions. The larger external force may be required to overcome the increased osmotic pressure due to charge repulsion and excluded volume interactions between ions in the experimental rod system. Further, particle number density effects on rotational and translational dynamics might require higher effective Pe to achieve ordering than predicted by the simple theory that is valid for Pe < 1. Finally, the time-dependent electric-field driving force complicates the comparison to the steady-state theoretical results.

An additional deviation from theory is that at high Pe, we observe the formation of disordered, jammed structures. This result contradicts the prediction that as the field strength is increased; the colloidal volume fraction ought to increase to the point that crystalline structures form.[35] We attribute this discrepancy to the formation of jammed structures, which prevent formation of the high degree of orientational ordering required to achieve the densest, crystalline assemblies. A first possible mechanism, which could lead to formation of these jammed structures, is that at high Pe the kinetics of the electrophoretic deposition is too rapid relative to orientational relaxation times to allow the specimens to self-organize into crystalline arrays. Attention to the effect of increased volume fraction (or effective viscosity) on the rotational diffusivity of rods in a uniform velocity field would help address this potential effect. A second possible mechanism is that the Pe are sufficient to densify the suspensions above their glass transition volume fraction. Yatsenko and Schweizer[44] predicted a glass transition volume fraction of 32% for an aspect ratio ~ 4. The high field experiments all result in assembled structures with volume fractions larger than this glass transition volume fraction. In future studies, through measurements of the mean-squared displacement, the approach to the glass transition could be determined quantitatively.

We also observe formation of domains and grain boundaries in the nematic phases. For example, the average domain size is ~ 680 ± 120 $\mu m^2$ for the applied voltage of 1.85 V in the plane parallel to the electrode surface. Qualitatively, the domain size is observed to be a strong function of the applied voltage, as apparent in Figure 2-5. It is interesting to consider the future possibility that larger nematic domains might be produced through variation of the applied voltage, as in annealing. Moreover, future quantification of the nematic texture would more definitively address the question of spatial persistence of local order in the colloidal rod suspensions.

Under optimal assembly conditions (1.85 V) we find that the density of the assembly varied periodically as a function of height leading to positional and orientational symmetries. In Figure 2-9d we plot the structure factor along the z-axis for the nearest four layers and find periodicity at $q_z$=12.3 or z=0.5D, which recovers the 0.5D layers seen in the spheroidal number density in Figure 2-9b. This periodicity suggests that these conditions induce the formation of a body-centered tetragonal (BCT) phase with spheroids layered in alternating fashion (Figure 2-9c and 2-9h). For comparison, we overlay the S(q) for a BCT lattice of spheroids (see Figure 2-9c). An interlayer spacing of 0.5D suggests that other known ordered phases are not commensurate. For example, in smectic structures this spacing is expected to be no less than the minor axis of the rod (Figure 2-9e).[35] Alternatively, the interlayer spacing of the crystal structure of spheroids studied by Frenkel and Mulder was 0.866D at a volume fraction of 74% (Figure 2-9f).[6] For a volume fraction of 49% (equal to the experimental volume fraction), this crystal would have an interlayer spacing of 0.94D. Pfleiderer and Schilling observed even denser spheroidal crystals with an interlayer spacing of 0.5D (Figure 2-9g) at a volume fraction of ~77%.[14] For a volume fraction of 49% this interlayer spacing would be 0.6D. Finally, it is interesting to note that the

BCT phase has not been previously predicted in equilibrium self-assembly of hard spheroids, although there is evidence of the BCT phase in the assembly of anisotropic colloidal particles such as heterodimers.[45,46] While the observed interlayer spacing of 0.5D and the high order parameter (S = 0.77) are consistent with the BCT structure, we cannot say whether the emergence of the BCT phase is a field-induced phase or a non-equilibrium phase. Further studies are necessary to be able to distinguish the effect of the field on the phase diagram of the ordered rods.

Finally, we note that although we used an electric field to drive the particles to higher densities, the system is suitable for the study of equilibrium self-assembly. Most field-assisted assembly studies reported to date have used time invariant driving forces that are described by the action of a fixed gravitational force on the colloids during assembly.[18,35] Even with a constant voltage DC electric field, the method discussed in this paper produces a time varying driving force on colloidal particles, as demonstrated by results in Figure 2-7. The origin of the time-varying force is most likely the temporal evolution of the electric field due to transport phenomena and electrochemical reaction of residual reactants at the electrode surface. This driving force is initially high and thus leads to rapid accumulation of colloids at the surface, a process that is advantageous for accelerated assembly kinetics. Next, as the residual reactant is depleted from the cell, the driving force becomes relatively small and nearly constant due to the lower effective field strengths. At this stage, a further gradual increase in volume fraction occurs. The relative magnitude of the applied field is now comparable to Brownian motion (Pe ~ 1). This congruence facilitates rearrangement and the efficient formation of ordered structures. On the contrary, if the driving force remains high after the initial deposition stage, as in the case of an applied initial voltage of between 2-3 V, jammed structures form instead of oriented arrays.

## 2.5. Conclusion

We have used DC electric fields to induce highly oriented ordered spheroidal phases in an initially low volume fraction colloidal rod suspension. We see a strong correlation up to intermediate voltages (~ 1.85 V) between experimental and theoretically reported order parameter and the volume fractions. This correlation suggests that the assembly is controlled by equilibrium thermodynamics. The method introduced in this paper is broadly applicable to the controlled self-assembly of colloidal particles. As opposed to other field-assisted assembly methods, such as sedimentation or centrifugation, the method provides a natural way to controllably vary the applied field over the course of the experiment. Moreover, it is a versatile method that requires only a small number of particles to study the kinetics and statistical thermodynamics of the assembly process. The method is an excellent candidate for the assembly of colloids such as Janus particles[47] that are often only available in limited quantities and this method has only small material requirements. Anisotropic particles have complex shapes and potential interactions and hence optimization of kinetic pathways might be required to successfully assemble particular target structures. Due to the scope for programming the applied field strength in this device, the electric-field assembly method described here provides flexibility to select particular kinetic pathways for assembly.

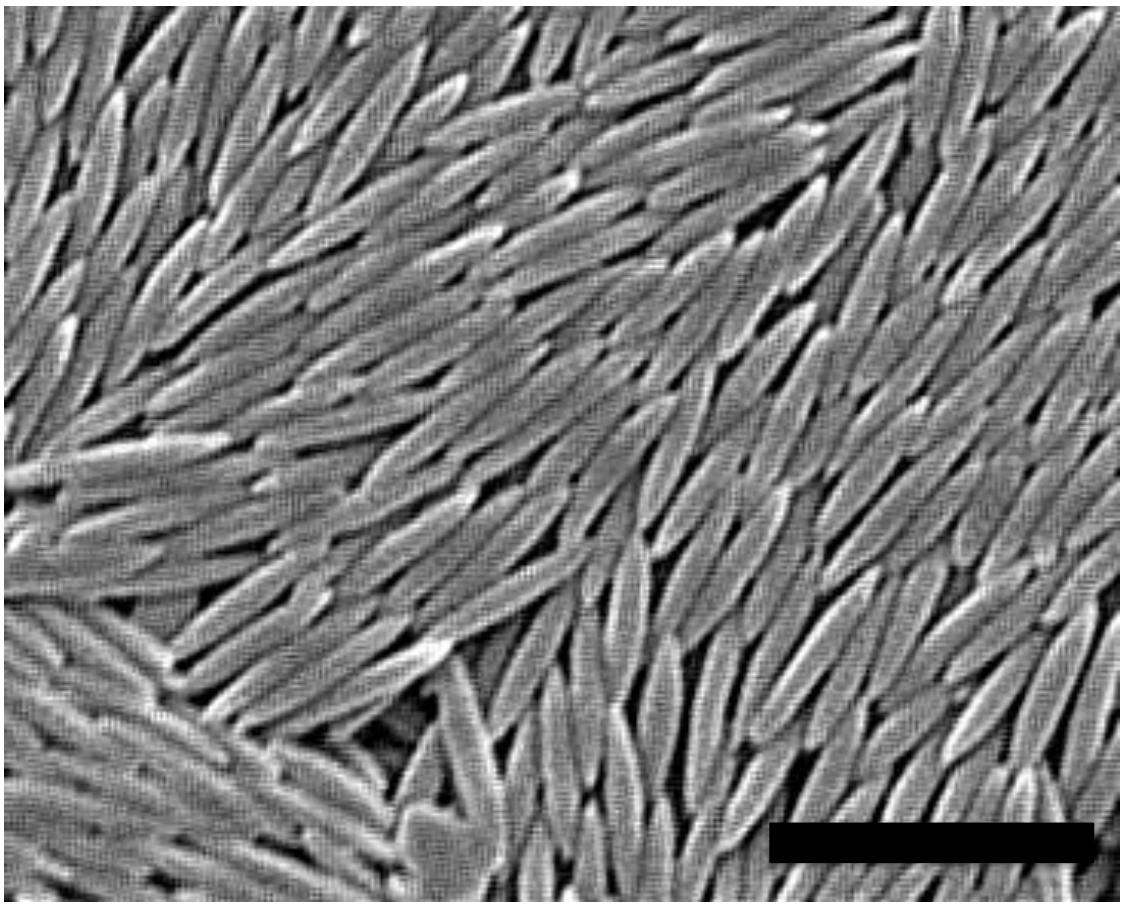

F**igure 2-1:** Scanning electron microscopy image of polystyrene ellipsoids. Their aspect ratio is 4.3 ± 0.6. Major axis $L$ = 3.35 ± 0.41 μm and a minor axis $D$ = 0.79 ± 0.07 μm. Scale bar is 5.0 μm.

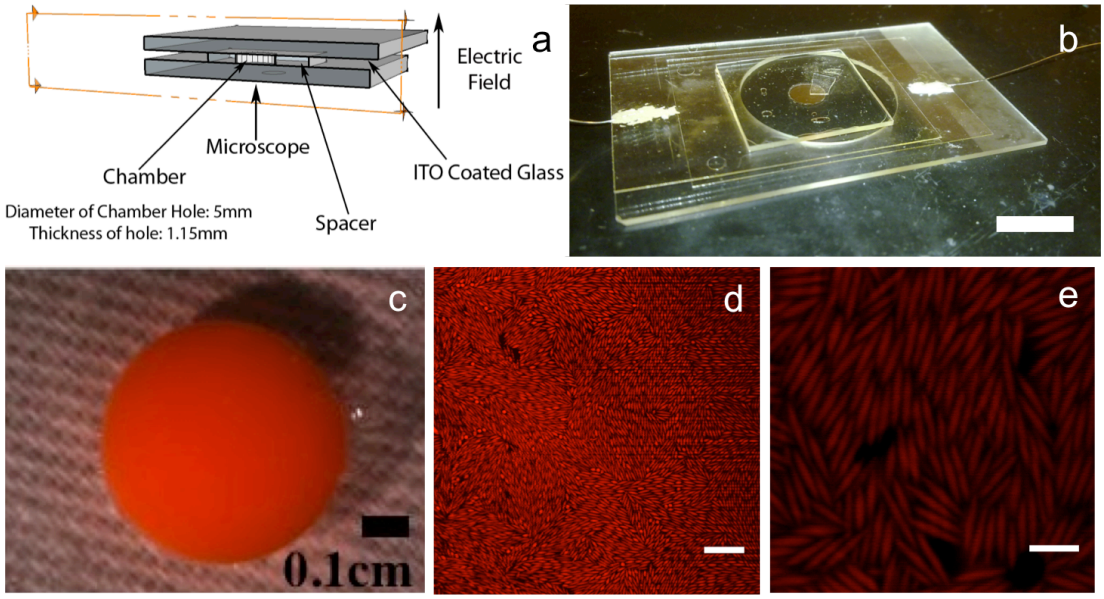


**Figure 2-2:** a) Schematic of the direct current electric field device used to assemble colloidal rods. The electrode gap is 1.15 mm. b) Image of device. Scale bar is 1.0 cm. c) Image of the chamber containing the colloidal suspension. The central region is orange due to fluorescence on the suspended rods. Scale bar is 0.1 cm. d) Zoomed out confocal laser scanning microscopy (CLSM) image of an assembly generated by the electrical field device. The assembly is obtained on application of a constant 2.0 V and the image is at the electrode surface. Orientational ordering on large scales is apparent. Scale bar is 20.0 μm. e) A zoomed in CLSM image of the same experiment. It shows the orientational alignment of individual rods. Scale bar is 3.0 μm.

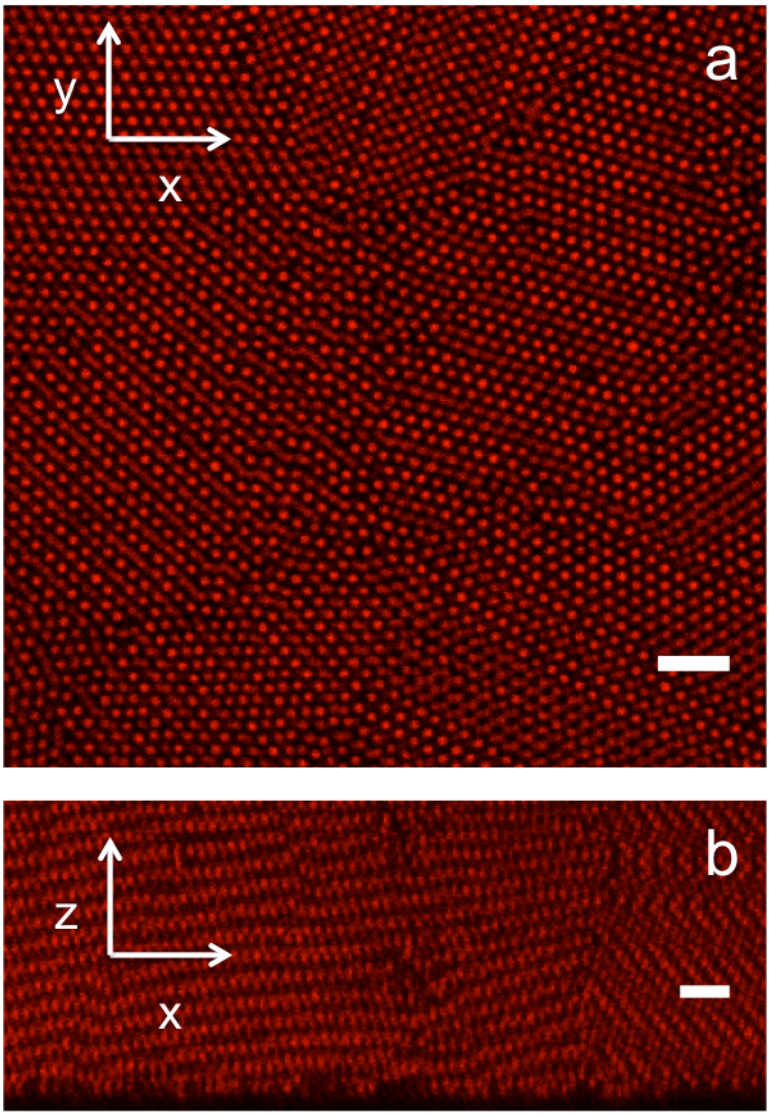


**Figure 2-3:** Spherical PMMA particles dispersed in a mixture of CHB and decalin form colloidal crystals on application of a constant voltage of 0.66 V/mm. Scale bars are 5 μm. (a) Image of the self-assembled structure in a plane parallel to the electrode surface. (b) Image of the colloids in a plane perpendicular to the electrode surface. The electrode surface is at the bottom of the image.

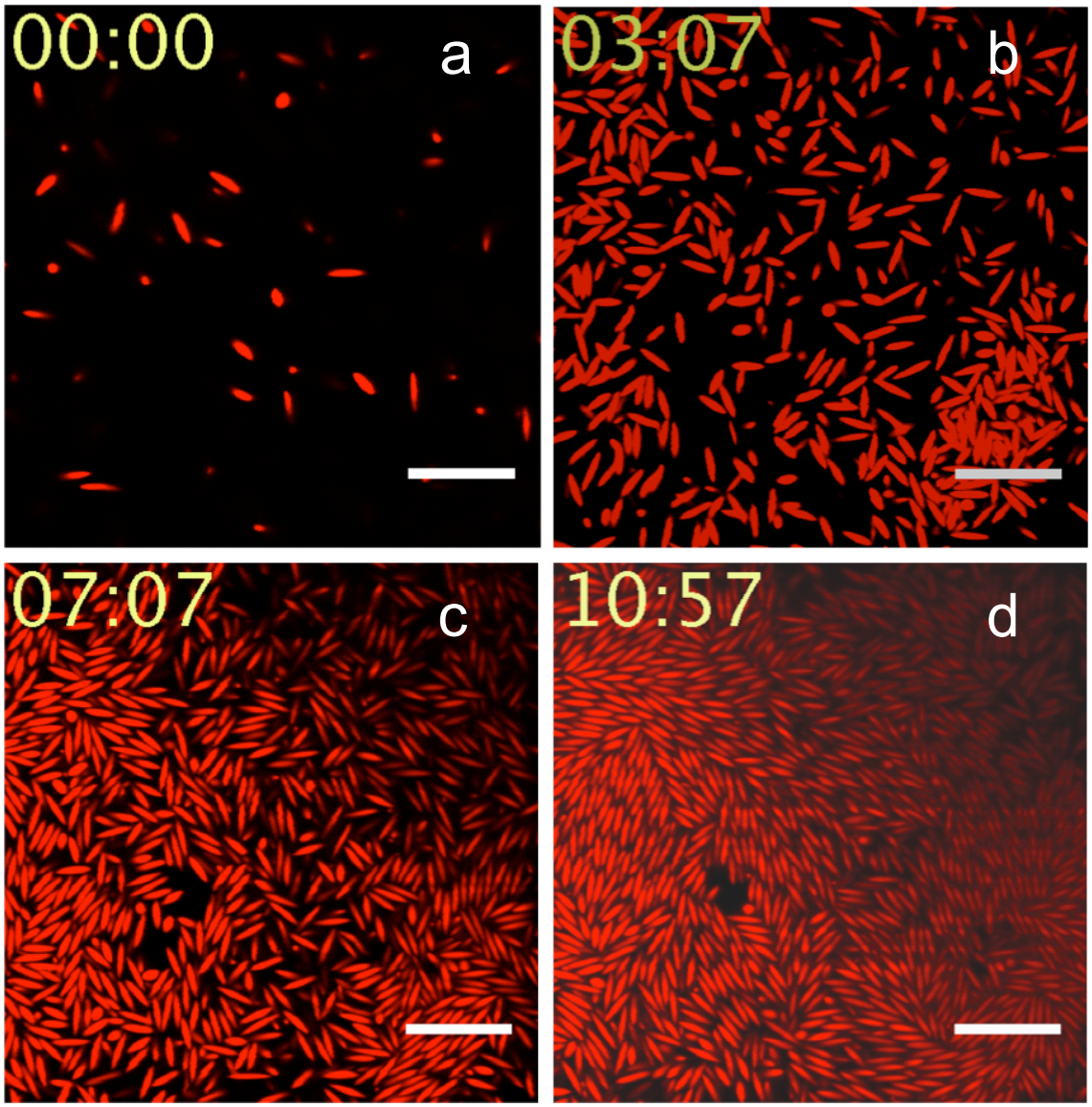


**Figure 2-4:** Images (a-d) show the kinetics of the self-assembly of colloidal rods as observed by confocal microscopy at 1.85 V. The initial volume fraction is 2%. The images, acquired in a plane parallel to the electrode surface, show that the volume fraction and orientational order increase over time, until a nematic phase is apparent after the electric field has been applied for about 11 min. The scale bars are 10.0 μm.

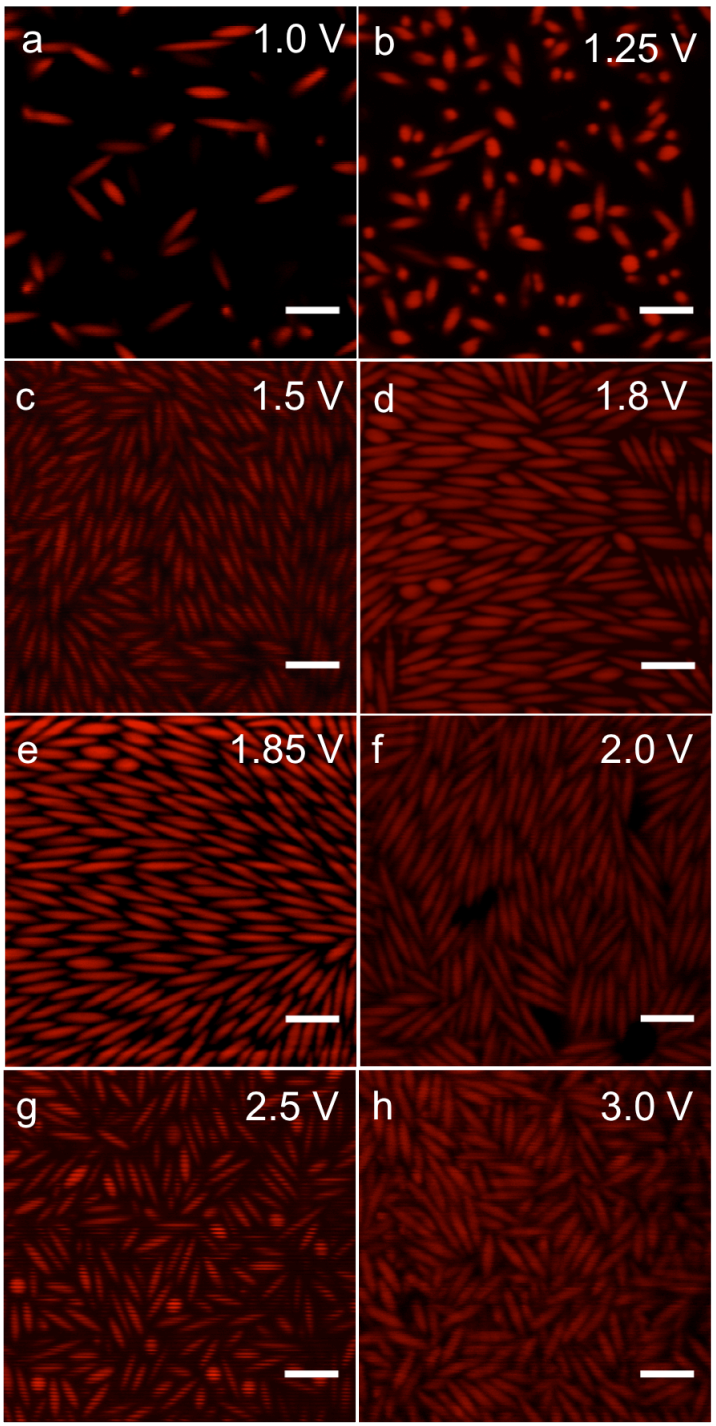


**Figure 2-5:** CLSM images of the self-assemblies acquired at the electrode surface after the structures have achieved steady state. Assemblies are obtained on application of different constant voltages (a-h). Scale bars are 3 μm.

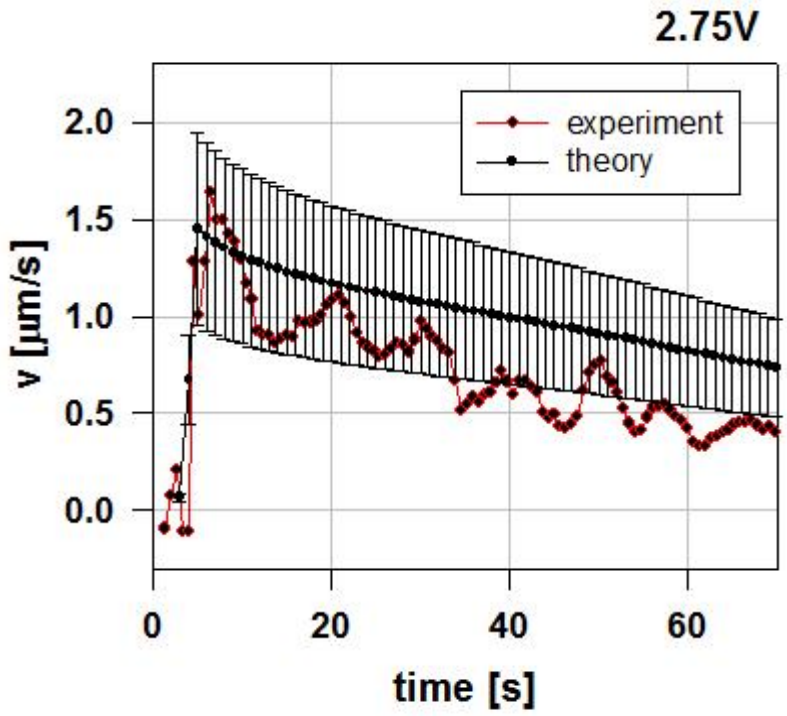


**Figure 2-6:** Comparison of electrophoretic mobility calculated theoretically and experimentally.

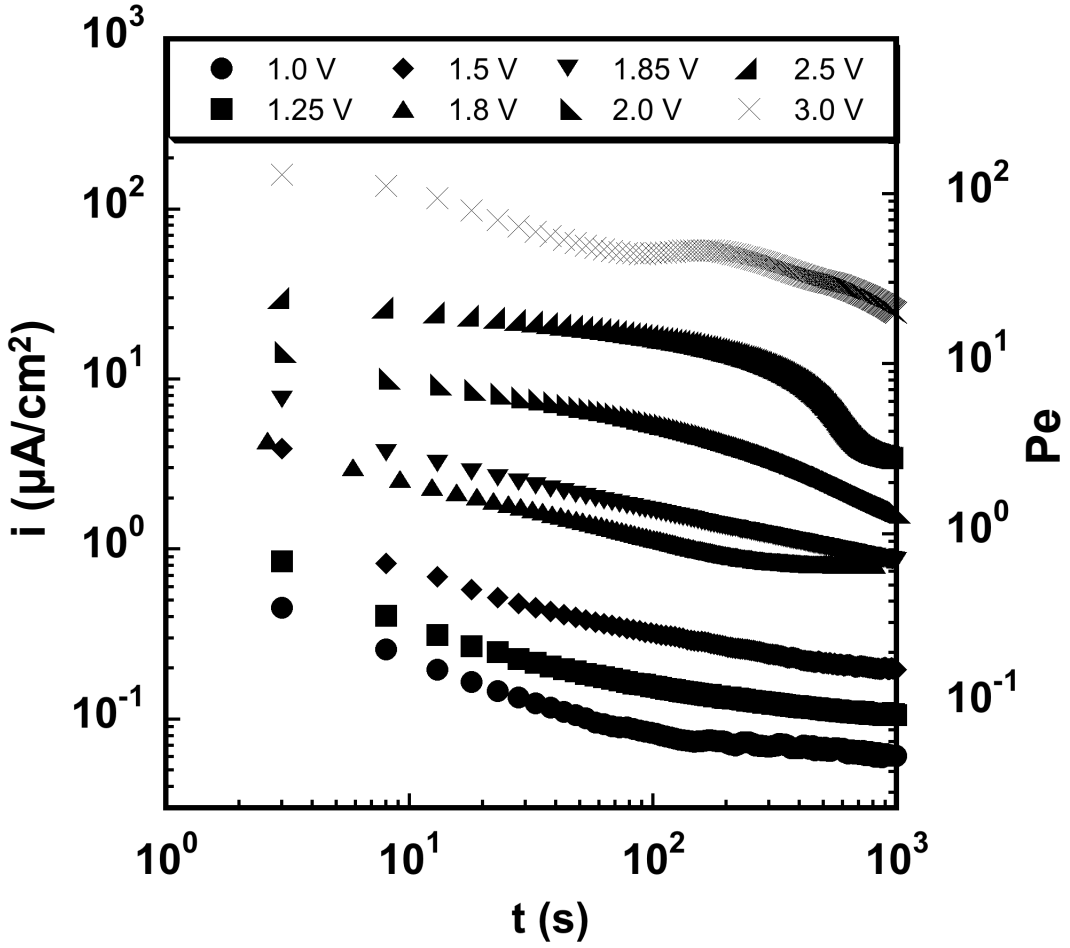


**Figure 2-7:** Time dependent current density as measured upon application of different constant voltages across DMSO containing 0.1 mM tetra butyl ammonium chloride salt. The measured current density is proportional to Pe (see text for definition), which is plotted on the right hand axis.

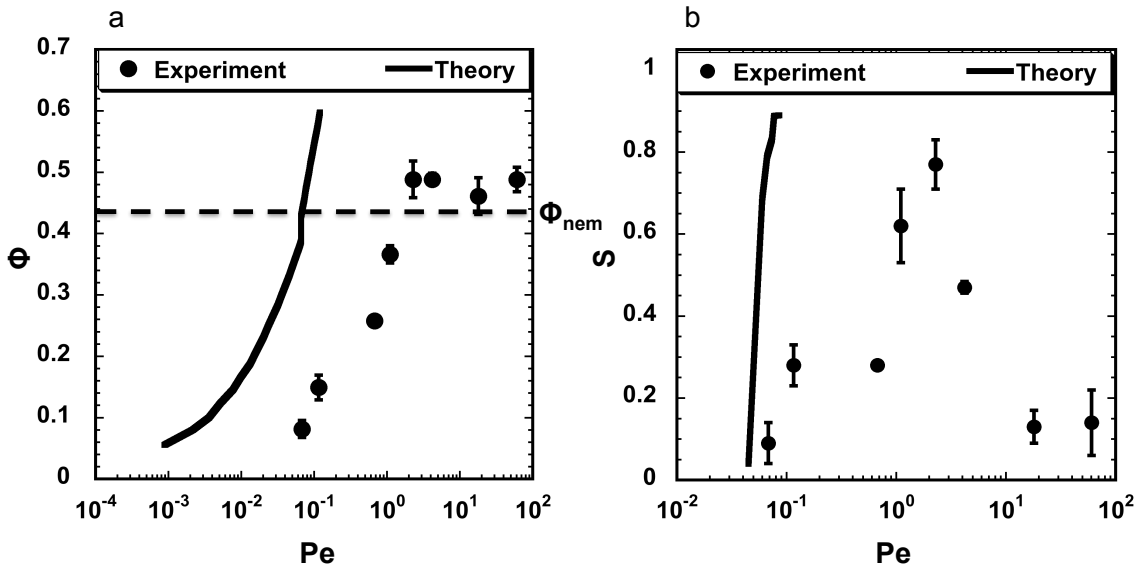


**Figure 2-8:** a) Volume fraction of the assembly structure of a 19.7 x 19.7 x 2.5 $mm^3$ stack is plotted for Pe (t = 100s). The measured volume fractions are also compared to expected I-N transition volume fractions from theory (dashed line).[38] b) The nematic order parameter, *S*, is plotted for a 19.7 x 19.7 x 2.5 $mm^3$ stack for different Pe (t = 100s) obtained on application of different initial voltages. Nematic ordering is observed when the Pe is ~ 1. These results are compared to the order parameter predicted from application of Equation (7) and the results of equilibrium self-assembly simulations (solid lines).[38]

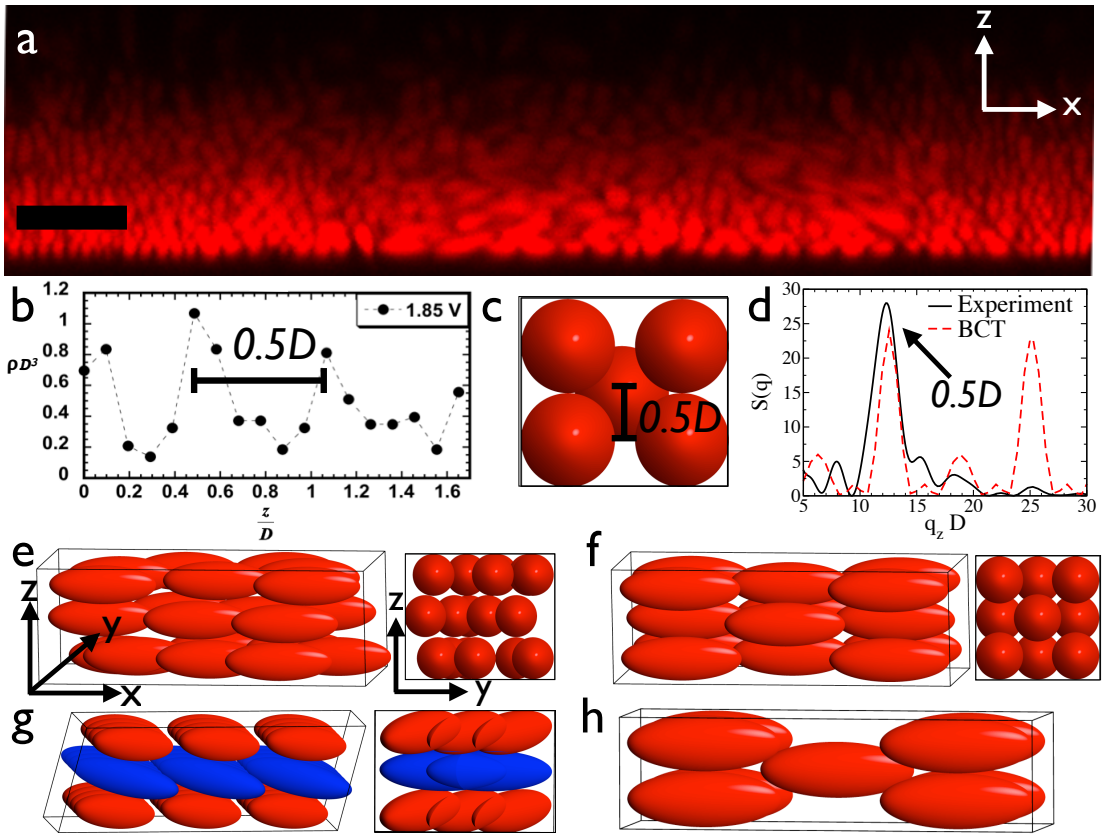


**Figure 2-9:** The positional order of the rods for the optimal assembly voltage is shown for layers nearest to the electrode surface. a) A CLSM image taken perpendicular to the coverslip showing the layered structure (scale bar 10 µm). b) Plot of the experimental density profile obtained by means of image processing. It shows a spacing of 0.5D between successive rod layers. c) Rendering of a lattice with such spacing (taken from the BCT structure shown in h). d) We compare the rod assemblies to the BCT lattice via the static structure factor S(q). At 1.85 V we find a peak at $q_z = 12.3/D$ corresponding to a layering distance $z = 0.51D$. Additionally, we plot the Bragg peaks of the BCT lattice and we find good agreement for the range of wavenumbers. For comparison, we show renderings in two perspectives of the known phases for hard ellipsoids (e-g) and the BCT phase in (c,h). All renderings in panels (e-h) are shown for volume fractions of 49%.

## 2.6. References


1 S. C. Glotzer, M. J. Solomon, *Nature Materials* 2007, ***6***, 557.

2 U. Agarwal, F. A. Escobedo, *Nature Materials* 2011, ***10***, 230.

3 P. F. Damasceno, M. Engel, S. C. Glotzer, ACS Nano 2011, published online DOI 10.1021/nn204012y.

4 Y. Kallus, V. Elser, *Physical Review E* 2011, ***83***, 036703.

5 M. J. Solomon, *Current Opinion in Colloid & Interface Science* 2011, ***16***, 158.

6 D. Frenkel, B. M. Mulder, *Molecular Physics* 2002, ***100***, 201.

7 A. P. Hynninen, J. H. J. Thijssen, E. C. M. Vermolen, M. Dijkstra, A. Van Blaaderen, *Nature Materials* 2007, ***6***, 202.

8 T. Koschny, L. Zhang, C. M. Soukoulis, *Physical Review B* 2005, ***71***, 121103.

9 M. J. Solomon, *Nature* 2010, ***464***, 496.

10 C. C. Ho, A. Keller, J. A. Odell, R. H. Ottewill, *Colloid and Polymer Science* 1993, ***271***, 469.

11 K. M. Keville, E. I. Franses, J. M. Caruthers, *Journal of Colloid and Interface Science* 1991, ***144***, 103.

12 Z. K. Zhang, P. Pfleiderer, A. B. Schofield, C. Clasen, J. Vermant, *Journal of the American Chemical Society* 2011, ***133***, 392.

13 A. Mohraz, M. J. Solomon, *Langmuir* 2005, ***21***, 5298.

14 P. Pfleiderer, T. Schilling, *Physical Review E* 2007, ***75***, 020402.

15 A. Donev, I. Cisse, D. Sachs, E. A. Variano, F. H. Stillinger, R. Connelly, S. Torquato, P. M. Chaikin, *Science* 2004, ***303***, 990.

16 A. Donev, F. H. Stillinger, P. M. Chaikin, S. Torquato, *Physical Review Letters* 2004, ***92***, 255506.

17 M. Radu, P. Pfleiderer, T. Schilling, *The Journal of Chemical Physics* 2009, ***131***, 164513.

18 D. Mukhija, M. J. Solomon, *Soft Matter* 2011, ***7***, 540.

19 Z. Dogic, S. Fraden, *Current Opinion in Colloid & Interface Science* 2006, ***11***, 47.

20 M. P. B. vanBruggen, F. M. vanderKooij, H. N. W. Lekkerkerker, *Journal of Physics-Condensed Matter* 1996, ***8***, 9451.

21 R. Ni, S. Belli, R. van, Rene, M. Dijkstra, *Physical Review Letters* 2010, ***105***, 088302.

22 L. T. Shereda, R. G. Larson, M. J. Solomon, *Physical Review Letters* 2010, ***105***, 038301.

23 J. P. Hoogenboom, P. Vergeer, A. van Blaaderen, *The Journal of Chemical Physics* 2003, ***119***, 3371.

24 A. L. Rogach, N. A. Kotov, D. S. Koktysh, J. W. Ostrander, G. A. Ragoisha, *Chemistry of Materials* 2000, ***12***, 2721.

25 M. Grzelczak, J. Vermant, E. M. Furst, L. M. Liz-Marzan, *ACS Nano* 2010, ***4***, 3591.

26 J. J. Juárez, M. A. Bevan, *The Journal of Chemical Physics* 2009, ***131***, 134704.

27 N. Li, H. D. Newman, M. Valera, I. Saika-Voivod, A. Yethiraj, *Soft Matter* 2009, ***6***, 876.

28 S. O. Lumsdon, E. W. Kaler, O. D. Velev, *Langmuir* 2004, ***20***, 2108.

29 O. D. Velev, K. H. Bhatt, *Soft Matter* 2006, ***2***, 738.

30 M. E. Leunissen, M. T. Sullivan, P. M. Chaikin, A. van Blaaderen, *The Journal of Chemical Physics* 2008, ***128***, 164508.

31 M. T. Sullivan, K. Zhao, A. D. Hollingsworth, R. H. Austin, W. B. Russel, P. M. Chaikin, *Physical Review Letters* 2006, ***96***, 15703.

32 J. P. Singh, P. P. Lele, F. Nettesheim, N. J. Wagner, E. M. Furst, *Physical Review E* 2009, ***79***, 050401.

33 M. Trau, D. A. Saville, I. A. Aksay, *Science* 1996, ***272***, 706.

34 K. S. Napolskii *et al., Langmuir* 2010, ***26***, 2346.

35 S. V. Savenko, M. Dijkstra, *Physical Review E* 2004, ***70***, 051401.

36 W. B. Russel, D. A. Saville, W. R. Schowalter, *Colloidal Dispersions,* Cambridge University Press, **1989**, p. 411.

37 M. Teubner, *The Journal of Chemical Physics* 1982, ***76***, 5564.

38 A. J. Bard, L. R. Faulkner, *Electrochemical Methods: Fundamentals and Applications,* Wiley, Hoboken, **2001**, p. 12.

39 Y. Solomentsev, M. Bohmer, J. L. Anderson, *Langmuir* 1997, ***13***, 6058.

40 H. Brenner, *International Journal of Multiphase Flow* 1974, ***1***, 195.

41 B. Tjipto-Margo, G. T. Evans, *The Journal of Chemical Physics* 1990, ***93***, 4254.

42 Z. Dogic, K. R. Purdy, E. Grelet, M. Adams, S. Fraden, *Physical Review E* 2004, ***69***, 051702.

43 R. Henríquez, M. Froment, G. Riveros, E. A. Dalchiele, H. Gómez, P. Grez, D. Lincot, *The Journal of Physical Chemistry C* 2007, ***111***, 6017.

44 G. Yatsenko, K. S. Schweizer, *Langmuir* 2008, ***24***, 7474.

45 I. D. Hosein, S. H. Lee, C. M. Liddell, *Advanced Functional Materials* 2010, ***20***, 3085.

46 E. B. Mock, C. F. Zukoski, *Langmuir* 2007, ***23***, 8760.

47 Q. Chen, J. K. Whitmer, S. Jiang, S. C. Bae, E. Luijten, S. Granick, *Science* 2011, ***331***, 199.

48 S. P. Dzul, M. M. Thornton, D. N. Hohne, E. J. Stewart, A. A. Shah, D. M. Bortz, M. J. Solomon, J. G. Younger, *Appl. Environ. Microbiol.* 2011, ***77***, 1777.

49 J. C. Crocker, D. G. Grier, *Journal of Colloid and Interface Science* 1996, ***179***, 298.

50 B. J. Yoon, S. Kim. *Journal of Colloid and Interface Science* 1996, ***179***, 298.

51 S. S. Dukhin, V. N. Shilov, *Adv. Colloid Interface Sci* 1980, ***13***, 153.

52 A. A. Shah, H. Kang, K. L. Kohlstedt, K. H. Ahn, S. C. Glotzer, C. W. Monroe, M. J. Solomon, *Small* 2012, **8**, 1551-1562.

# Chapter 3

# Reversible Direct Current Electric Field Assembly of Nano and Micron-Sized Colloidal Particles into Photonic Crystals with Structural Color

**Chapter Summary**

Direct current (DC) electric fields are used to self-assemble close-packed colloidal crystals from micro to nano-sized spheres. The three-dimensional ordered assemblies are created rapidly (~ 2 minutes) from an initially low volume fraction colloidal particle suspension using a capacitor-like electric field device that applies a steady DC electric voltage. Confocal microscopy is used to observe particle assembly structures. 6-fold diffraction patterns are observed on analysis of the particle assemblies using small angle light scattering methods, thus indicating the crystallinity of the samples. RGB structural color is also observed on assembly of spherical particles between 290 nm to 500 nm in diameter. A spectrophotometer is used to identify the reflection spectrum for these samples. Spectrophotometer analysis as well as small-angle light-scattering results are

explained theoretically using Snell's law and Bragg's law calculations. We switch the DC electric field to reversibly switch the spherical particle assemblies between the ordered-disordered states. We observe the reversible switch between colorless-color features of the bulk sample on switching the DC electric field.

### 3.1 Introduction

Spatial ordering at the micron and sub-micron scale is responsible for the distinctive optical and photonic properties found in nature, such as the brilliant, iridescent colors of butterfly wings[1] and beetles[2] as well as the camouflage of cephalopods[3]. Similar periodically ordered features at the sub-micron and micron-scale have been produced through top down fabrication[4] as well as through the self-assembly of synthetic colloidal spheres. Pusey and van Megen showed the formation of iridescent colors on simple self-assembly of colloidal spheres from their initial fluid phase to the highly ordered, close-packed assembly phases.[5] However, the self-assembly of colloidal particles is a slow process and prone to dislocations, vacancies and grain boundaries which leads to poor quality colloidal crystals. Methods such as spin coating,[6,7]and convective assembly[8-11] have significantly enhanced assembly rates as well as colloidal crystal uniformity to give high quality photonic crystals.

While these methods give permanent crystals that have a uniform color, structural color from colloidal crystals can also be tuned by embedding synthesized colloidal crystals into elastomers and polymers. [12] The elastomers change the color properties of the material by tuning the lattice arrangement of the embedded colloidal crystal by stretching and contracting in response to stimuli such as mechanical stress,[13] pH changes[14] and electric actuation[15].

Methods described earlier are used to create permanent colloidal crystals. However, the order-disorder transition of colloidal particle assemblies can be tuned easily by application of an external field. Hence, external fields such as Alternating Current (AC) electric fields,[16] centrifugation[17] and magnetic fields[18] are increasingly being used to control forces and thus the assembly of colloidal particles. In most cases, particles assemble reversibly into ordered structures on application of external fields. For example, Lumsdon et al. use AC electric fields to assemble colloidal particles into 2D ordered structures that dissipate into a disordered fluid phase on removal of the AC electric field.[16] However, AC electric field assembly needs high voltages to assemble colloidal particles. Further, most of the field driven methods need expensive equipment.

Here, we use a Direct Current (DC) electric field method to rapidly and reversibly assemble colloidal crystal structures into ordered assemblies.[19-21] The low voltage (less than 3 V) DC electric field is used to drive negatively charged polystyrene colloidal particles to the positively charged electrode surface. The particles densify at the electrode surface and form a thick, ordered crystal with close-packed structure. These materials have distinct optical properties that display structural color (for 290 nm to 500 nm diameter spherical particle assemblies). This structural color is maintained while the DC electric field is applied. However, removal of the DC electric field causes particles in the ordered crystals to transition back into their disordered fluid phase and lost their bulk color properties. Thus, DC electric fields can be used to reversibly assemble colloidal particles between ordered and disordered phases to tune their optical properties.

### 3.2 Materials and Methods

### 3.2.1 Spherical Colloids

Polymeric particles suspended in organic solvents are used in this paper for DC electric field assembly experiments. Poly(methyl methacrylate) (PMMA) particles suspended in cyclohexyl bromide and decalin (CHB-decalin) is a refractive index matched system used for imaging the 3D structure of the DC electric field induced assembly. Undyed polystyrene (PS) particles suspended in dimethyl sulfoxide (DMSO) is a non-refractive index matched system used for all light scattering and spectrophotometry experiments

Poly(methyl methacrylate) (PMMA) Particle Synthesis

PMMA colloids are stabilized with polyhydroxystearic acid (PHSA) using methods described earlier.[7,22] The synthesized particles were 0.70 ± 0.08 μm in size. The particles were not adequately charged for DC electric field assembly at this stage. To increase the charge on colloidal particles, we increase the stabilizer concentration on the surface of the particle. 1 gram of the synthesized particles were suspended in 20 mL hexane (Sigma-Aldrich). 1 gram of PHSA was added to the solution. Finally, 0.01 grams of the initiator azobisisobutyronitrile (AIBN) was also added and dissolved in solution. This solution was taken in a 3-neck flask and heated at 60-70°C for approximately 2 hours. The particles were then thoroughly washed with hexane by centrifugation at least 5 times and dried subsequently for 1 day. These particles are then dispersed in cyclohexylbromide (CHB, Sigma-Aldrich) and decalin(Sigma-Aldrich) (66:34 volume percent). 100 μM tetra butyl ammonium chloride (TBAC) salt is also added to the system to increase the conductivity of the solvent. This process ensures that there is sufficient stabilizer and charge on the colloidal particles for DC electric field assembly.

Polystyrene (PS) Colloids

PS particles of a variety of different sizes are purchased in aqueous suspensions (Invitrogen Inc. and Bangs Laboratories). These suspensions are centrifuged at 5000 G for 1 hour to separate the particles from the solvent (one transfer). The solvent is replaced by dimethyl sulfoxide (DMSO) for DC electric field assembly.

### 3.2.2 DC Electric Field Device

Two device geometries are used in the assembly of spherical particles.

A sectional view of the primary DC electric field device is shown in Figure 1a. The device is made up of indium tin oxide (ITO) coated transparent electrode slides. These slides are separated by a thin, closed spacer (120 μm thick, Grace Bio-Labs imaging spacers, GBL654002), with the ITO conductive half of the slide facing inwards. The colloidal suspension is placed within the spacer and is in contact with the two electrode slides. The slides are glued to T2 thermocouple wires (Goodfellow Inc) that are connected to a DC electric voltage source. Voltages of up to 3 V are applied across the device using a DC electric voltage generator ().

Nano-sized particles are assembled using alternate device geometry for ease of assembly visualization. The alternate device geometry consists of two parallel ITO coated electrode coverslips separated by a thick, open spacer (1mm thick) that are dipped in a large volume of the colloidal suspension (~ 100mL). The spacer is made from microscope slides (Sigma Aldrich) that are cut into smaller pieces (1 cm x 3 cm) and stuck to each of the electrodes using UV curable glue (Light weld, Dymax Corporation). Voltages of up to 3 V are applied across the device using a DC electric voltage generator (HP). The device is removed from the colloidal suspension and the slides are separated from the spacer using a sharp blade. These slides are subsequently imaged using a Scanning Electron Microscope (SEM).

### 3.2.3Assembly Visualization

Confocal Laser Scanning Microscopy (CLSM)

The electric field device was placed on the stage of a Nikon A1r confocal microscope with a 100X objective. The positive polarity electrode was positioned directly above the objective. Fluorescent mode was used to image dyed PMMA in CHB-Decalin particles. The reflection mode was used in the imaging of undyed PS in DMSO particles.

Scanning Electron Microscopy (SEM)

SEM imaging was used to image nano-sized particles that could not be imaged using a CLSM. The electric field device is carefully removed from the particle suspension and allowed to air dry for approximately one hour. The positive and negative electrodes are then separated and carefully cut into small pieces using a sharp blade. These pieces are stuck to SEM stubs using carbon black conductive adhesives and imaged using an SEM (Phillips XL-30 field emission gun (FEG).

### 3.2.4 Small Angle Light Scattering

Diffraction patterns from the field-assisted assemblies of microspheres were probed using a home made optical setup that consisted of the following. A laser beam of wavelength 632.8 nm (Melles Griot Inc) with a $1/e^2$ diameter of 0.71mm was expanded to 20 times its beam width using a custom built beam expander and was subsequently reduced to a beam spot size of 5 μm at the focal length of a converging lens. The reduced beam spot was used as the incident light to obtain diffraction patterns which were captured using a wide-angle lens (Thor Labs) mounted on a CCD camera (Pixel Fly Co). The above setup was used for particles greater than 0.6 μm (diameter) and for particles greater than 0.4 μm (diameter), a solid state laser (source) of

wavelength 532nm was incorporated suitably. This setup enabled the study of diffraction patterns with the colloidal system contained within the electric field device.

### 3.2.5 Spectrophotometry

Structural color is measured using a fiber optic spectrophotometer (USB 2000). The wavelength range probed is from 300 nm to 750 nm (visible region). The probe is placed exactly perpendicular to the sample to ensure that angle of incidence of white light and reflections are both perpendicular. The spectrum of the sample taken before application of the electric field is subtracted from the sample bearing structural color to ensure that stray light effects from the surroundings and the DC electric field device are mitigated.

## 3.3 Results and Discussions

We test the assembly of spherical particles in the electric field device using a PMMA particle system suspended in CHB: decalin solvent system (66:34 volume ratio, c.f. Methods). The particles are also dyed with Nile Red (Sigma-Aldrich) for easy visualization of the assembly on the CLSM. As is evident in Figure 1b, this particle system is initially dispersed in the fluid phase. Application of a 2 V DC electric field leads to the electrophoretic motion of PMMA particles to the negatively charged electrode. Over time, the volume fraction of the particles at the substrate increases and eventually, they self-assemble into close packed crystal structures (c.f. Figure 1c). The resultant assemblies are 3D crystalline assembly structures as shown by the x-z confocal micrograph shown in Figure 1d. DC electric fields have been shown to induce gradients in the osmotic pressure of a colloidal suspension.[21] High osmotic pressures lead to an

increase in particle concentration in that region. Hence, the region closest to the coverslip has a high particle volume fraction that is sufficient to induce a fluid-crystal transition. As we go away from the coverslip, the osmotic pressure reduces and this leads to a reduction in the volume fraction of the sample in that region. Eventually, the volume fraction of the colloidal particles drops below the fluid-crystal transition volume fraction. Hence, the assemblies are crystalline close to the electrode surface while the particles transition from a crystalline to amorphous state at a height of ~ 20 μm (c.f. Figure 1d).

The mechanism of DC electric field assembly has been explained in Shah et al.[21] Briefly, application of a DC voltage leads to the reaction of residually dissolved species, such as water, oxygen, and potentially TBAC, at the electrode surface. These reaction leads to the generation of ions whose migration leads to the evolution of current in the electric field device. We measure and report the current using a potentiostat (Autolab Inc) as a function of time (c.f. Figure 1e). This current is directly proportional to an effective electric field generated in the device.

$$E = \frac{i}{\psi_0 A} \qquad (1)$$

Here, E – effective electric field, i - measured current, A – surface area of the electric field device.

This electric field couples to the charge on the colloidal particles that is predominantly a consequence of the dissociation of ions on the surface stabilizing groups. The particles are hence electrophoretically driven to the oppositely charged electrode. The role of the electric field is to control the concentration of the colloidal particles at the electrode surface. Once a critical volume fraction is achieved, the fluid undergoes a phase transition to a crystalline phase, as reported in Figure 1b-d. In all the subsequent experiments, we ensure that we apply a sufficiently

strong DC voltage (up to 3V) to lead to the generation of sufficient current to drive colloidal particles into crystalline assemblies.

Figure 1 introduces the DC electric field device used to assemble spherical colloidal particles into close-packed crystalline structures. We use a thin spacer (120 μm thick) to separate the two electrodes of the device. A thin spacer is used as 3D crystalline structures are created more rapidly with smaller numbers of particles. This helps the generation of assemblies rapidly (~ 2 minutes) and the assemblies are maintained for at least 1 hour.

Figure 2 shows imaging and light scattering results of DC electric field induced assembly of polystyrene (PS) colloidal spheres suspended in DMSO. All the experiments were performed with particles at an initial volume fraction of 2%. Figure 2a shows the assembly of 1.2 μm diameter sulfate stabilized-polystyrene particles (Invitrogen Inc) suspended in DMSO obtained on application of a 2V DC electric field. Small angle light scattering measurements were also performed using a 633 nm laser for this sample and the 6-fold diffraction pattern is shown in the inset image. The measured scattering angle of the diffraction pattern, which is an indication of the spacing of the close-packed crystal as shown later, is 28.8° for the 632.8 nm red laser and 24.9° for the 532 nm green laser. The experimental scattering angle is the measured angle between the line joining the sample to center of the screen and the line joining the sample to the points on the 6-fold symmetry. Figure 2b shows the assembly of 0.95 μm diameter sulfate stabilized-polystyrene particles (Invitrogen Inc). This assembly was obtained on application of a voltage of ~ 2.25 V and small angle light scattering measurements were performed (6-fold diffraction pattern is shown inset). The measured scattering angle of the diffraction pattern is 39.2° for the red 632.8 nm laser, while it is 31.9° for the green 533 nm laser. Figure 2c shows the assembly of 0.50 μm diameter sulfate stabilized-polystyrene particles (Bangs Laboratories Inc).

The assembly was obtained on application of 2.65 V DC electric field and small angle light scattering measurements were performed. Here, a 6-fold diffraction pattern is not observed for the 633 nm red laser, while the inset image (Figure 2c) shows the 6-fold diffraction pattern observed for the 532 nm laser.

Figure 2d shows the assembly of 0.4 μm diameter carboxylate stabilized polystyrene particles (Bangs Laboratories). The assembly was obtained on application of 2.75 V DC electric field. Figure 2e shows the assembly of 0.29 μm diameter sulfate stabilized-polystyrene particles (Invitrogen Inc). The assembly was obtained on application of a 2.9 V DC electric field. Light scattering experiments do not show 6-fold diffraction patterns for these assemblies.

The applied voltages used to assemble the colloidal crystals were identified by direct visualization of the assemblies on the CLSM. We see an increase in the applied voltage needed to create the colloidal assembly with decrease in the size of the colloidal particle. This is because Brownian motion that promotes disorder in a colloidal particle suspension increases with decrease in size of the particle,[23] while on the other hand, the surface charge density that is directly proportional to the electrophoretic driving force does not change significantly for different particles.

Finally, the scanning electron microscopy (SEM) image of the assembly of 0.11 μm diameter carboxylate stabilized-polystyrene particles is shown in Figure 2f. These particles were assembled at a voltage of 2.9 V using an alternate device geometry (c.f. Methods). The alternate device geometry consists of ITO coated electrode coverslips separated by a thick spacer (1mm thick) that are dipped in a large volume of PS-DMSO (~ 100mL). The volume fraction of the PS particles is substantially lower as compared to other experiments (~ 0.01 volume %). The DC electric field is also applied much longer (~ 24 hours) to create 3D colloidal assemblies. This is

due to the low initial volume fraction of the suspension. We subsequently remove the coverslips from the solution and air-dry the DMSO solution. The slides are imaged in an SEM because the particle size is too small to permit visualization on a CLSM. Colloidal assemblies are only observed on the positively charged electrode and this confirms that the crystals seen in the SEM are not as a result of drying processes.

The light scattering measurements and scattering angles of colloidal crystals are strongly tied with their optical properties. We analyze the light scattering experiments of Figure 2 in Figure 3. Figure 3a shows the path of light impinging on a DC electric field device. Light, incident perpendicular to the sample, enters a new liquid medium from air and this results in a decrease in the wavelength of light in accordance to Snell's law (Figure 3a, point 1). Snell's law is given by,

$$\frac{\lambda_2}{\lambda_1} = \frac{\eta_1}{\eta_2} \qquad (2)$$

Here, $\lambda_2$ represents the wavelength of light in colloidal suspension, $\lambda_1$ represents the wavelength of light in air, $\eta_1$ refractive index of air and $\eta_2$ refractive index of the colloidal suspension. The colloidal suspension is itself made up of polystyrene particles suspended in dimethyl sulfoxide (DMSO) solution. To calculate the change in wavelength, we calculate the effective refractive index for this suspension using:

$$\eta_2 = \phi_{PS}\eta_{PS} + \phi_{DMSO}\eta_{DMSO} \qquad (3)$$

Here, $\phi_{PS}$ represents volume fraction of PS, $\phi_{DMSO}$ represents the volume fraction of DMSO, $\eta_{PS}$ refractive index of polystyrene and $\eta_{DMSO}$ refractive index of DMSO. Now, we assume the volume fraction of PS to be the close-packed crystalline volume fraction (0.74).[23] Adjustments are made to account for the Debye layer thickness of the colloidal particles (c.f. SI). Substituting this effective refractive index in (2), we obtain the wavelength of the incident light in the

solution. We note that at this stage, there is no change in direction of the light on account of the perpendicular incidence of the laser light on the sample. The light is subsequently incident on a crystalline array of colloidal particles. The light scatters subsequently and constructively interferes at an angle given by Bragg's law (Figure 3a-point 2).

$$\theta_1 = \sin^{-1}\left(\frac{\lambda_{laser}}{\eta_2 2d}\right) \qquad (4)$$

Here, $\theta_1$ represents the scattering angle, $\lambda_{laser}$ represents the wavelength of the incident laser light and d is the distance of 1100 plane of the HCP lattice structure. We note that this 1100 HCP lattice distance is used based on observation of the crystalline structure and orientation obtained from CLSM images. $d_{HCP}$ varies with particle size (c.f. SI). The scattered light subsequently undergoes refraction at air and colloidal suspension interface on exiting the electric field device (Figure 3a-point 3). The change in angle is given by

$$\theta_{the} = \sin^{-1}\left(\frac{\eta_2}{\eta_1}\sin(2\theta_1)\right) \qquad (5)$$

Here, $\theta_{the}$ represents the final scattered angle that is subsequently compared to our experimentally observed angle. Figure 3b shows that there is strong correlation in the theoretical and experimentally observed scattering angles, which confirms the formation of an HCP crystal phase with the 1100 plane being the scattering geometry. As seen in Figure 3b, $\theta_{the}$ is greater than 90° for colloidal crystals made from particles below 590nm for the red laser (633nm) and 490 nm for the green laser (532 nm). Hence, 500 nm diameter particles show a diffraction pattern for the green laser (532 nm) but not for the red laser (c.f. Figure 2). Spherical colloidal crystals made of 290 nm – 500 nm instead reflect white light and hence emit bulk structural color as shown in Figure 4.

Figure 4 shows the bulk structural color, spectrophotometer data analysis and reflection channel imaging of the 3 samples (290 nm, 400 nm and 500 nm sized PS particles) that show distinct optical properties in the visible region. Figure 4 a-c shows CLSM reflection channel images of 500 nm, 400 nm and 290 nm diameter PS particles respectively. The images indicate clear crystalline order in the sample. Figure 4d-f show the orange, green and blue structural color observed on vertical incidence and reflection of light for the 500 nm, 400 nm and 290 nm diameter PS samples respectively. The structural color observed is reproducible and distinct for different particle sizes. This is further shown in the spectrophotometer data in Figure 4 g-i where there are clear peaks corresponding to the observed structural color for the various samples.

Figure 5 shows structural color reversibility (for 500 nm diameter particles) that can be obtained by switching the DC electric field. A close-packed crystalline structure is created on application of the DC electric field which gives rise to structural color (c.f. Figure 3-4,3-5a). Switching off the DC electric field causes removal of the electrophoretic driving force that is responsible for the formation of a close-packed crystalline structure. Particle Brownian motion then promotes disorder in the sample that leads to a loss of the crystalline structure and thus the structural color is also lost (c.f. Figure 3-5b). Application of the DC electric field causes the system to revert back to an ordered crystalline state that has bulk structural color (Figure 3-5c). Color is lost rapidly (~ 5 seconds) while regenerating color takes slightly longer (~ 1 minute). This reversibility of color formation has been tested at least 6 times.

### 3.4 Conclusions

We used a direct current (DC) electric field method to produce ordered colloidal assemblies from nano-micron sized spherical particles. These 3D assemblies were visualized

using reflection channel confocal microscopy for micron-sized particles and scanning electron microscopy for nano-sized particles, which confirmed the sample crystallinity. In this paper, we study the optical properties of the crystalline assemblies and use small angle light scattering methods to study the light diffraction from the sample. 6-fold symmetry was observed for crystalline samples and the scattering angle was predicted using a theory based on Snell's law and Bragg's law. Reflective optical properties were also analyzed using a spectrophotometer and we show the formation of color across the visible spectrum by changing the size of the assembling particle. The origin of the structural color is also explained theoretically. The DC electric field device is thus a simple method to rapidly produce colloidal spherical crystals (~ 2 minutes) that have unique optical properties. The DC electric field can be switched off to disassemble the colloidal particles and structural color is lost almost instantaneously. The DC electric field device can thus rapidly and reversibly create structural color in colloidal particles and such materials could be useful for applications such as displays, camouflage and sensors.

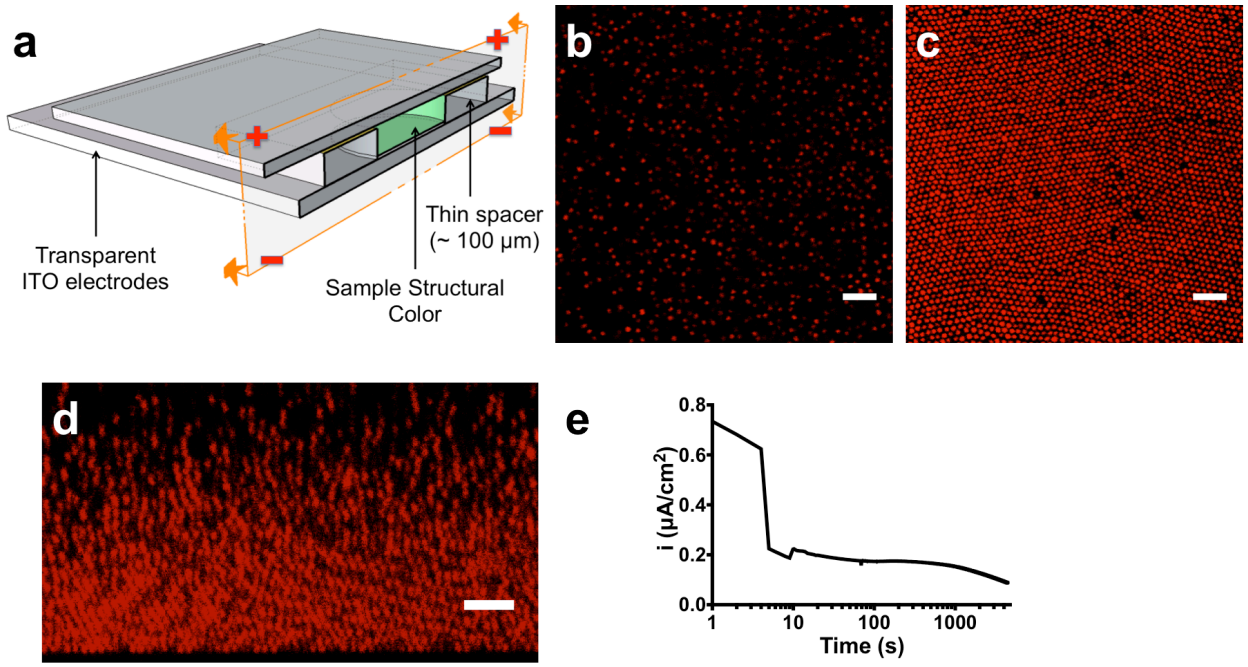


**Figure 3-1:** a. Schematic of electric field device. b. CLSM image of dispersed PMMA particles in CHB-decalin. c. CLSM x-y image of PMMA particle assembly structure at the coverslip on application of 2 V DC electric field. d. CLSM x-z image of PMMA particle assembly on application of 2 V DC electric field. Scale bars are 5 µm.

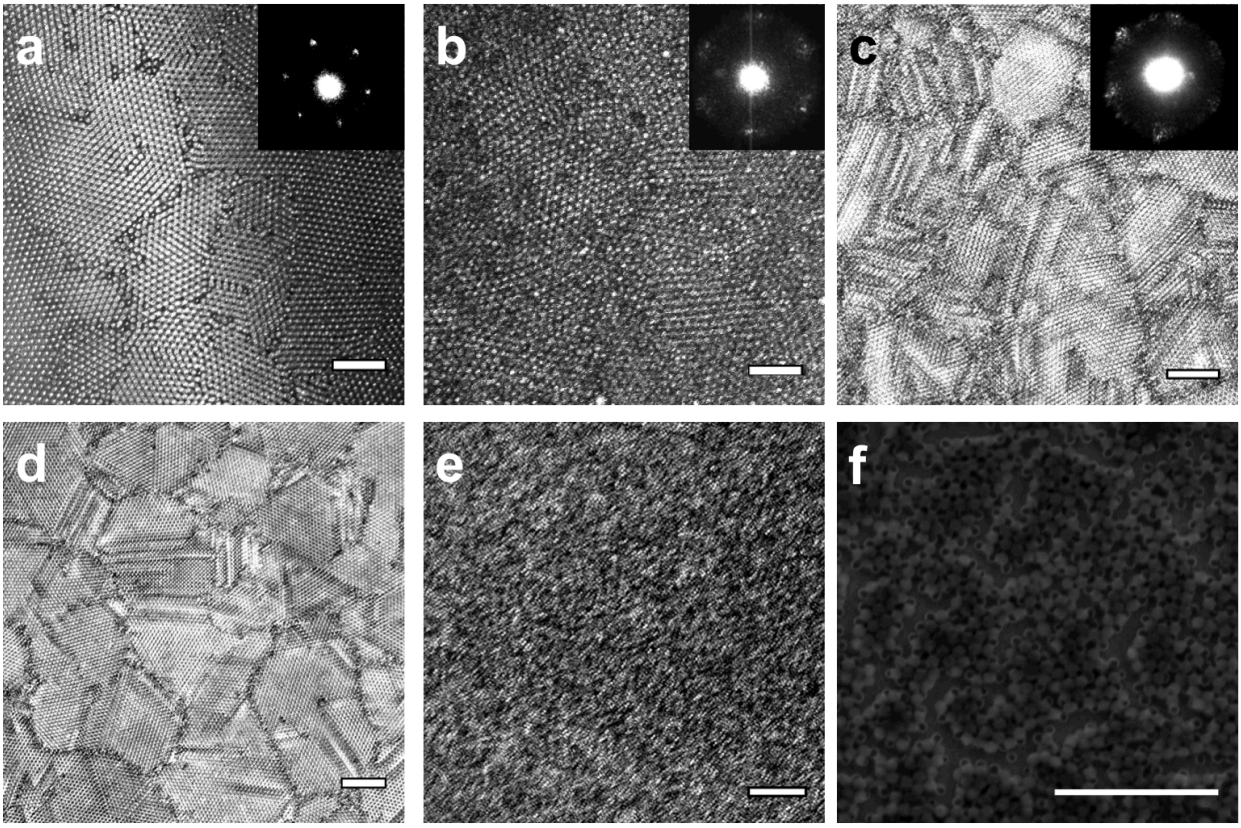


**Figure 3-2:** a-e CLSM reflection channel image of DC electric field assembly at the coverslip for a. 1.2 μm PS particles in DMSO. b. 0.95 μm PS particles in DMSO. c. 0.5 μm PS particles in DMSO. d. 0.4 μm PS particles in DMSO. e. 0.3 μm PS particles in DMSO. f. Scanning electron microscopy image of 0.11 μm PS particles in DMSO. Scale bars are 5 μm.

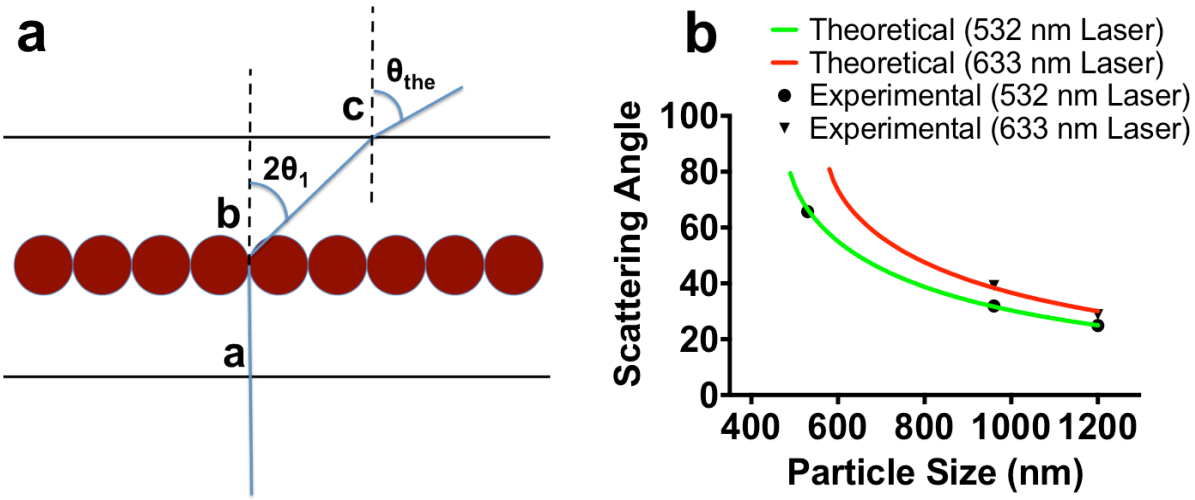


**Figure 3-3:** a. Path of light on incidence on a DC electric field device with a colloidal crystal assembly. b. Experimental observations and theoretical predictions of the scattering angle as a function of particle size for static light scattering measurements.

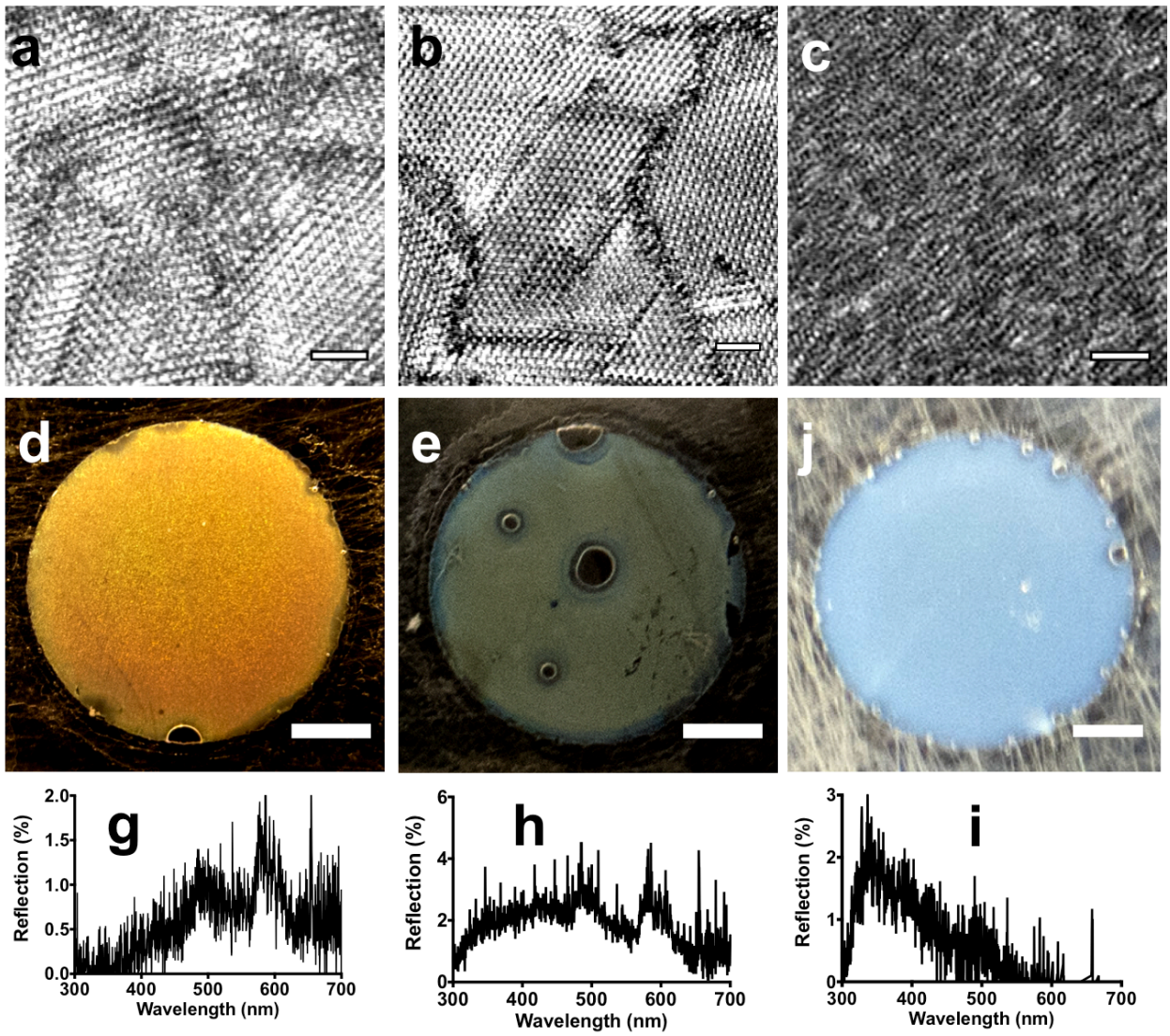


**Figure 3-4:** a-c CLSM reflection channel images of the DC electric field induced assembly of 500 nm, 400 nm and 290 nm sized particles respectively. d-f Bulk structural color observed for the 500 nm, 400 nm and 290 nm sized particles respectively. (Scale bars are 2 mm) g-i Spectrophotometry data of the structural color for 500 nm, 400 nm and 290 nm sized particles respectively. Scale bars are 2 μm.

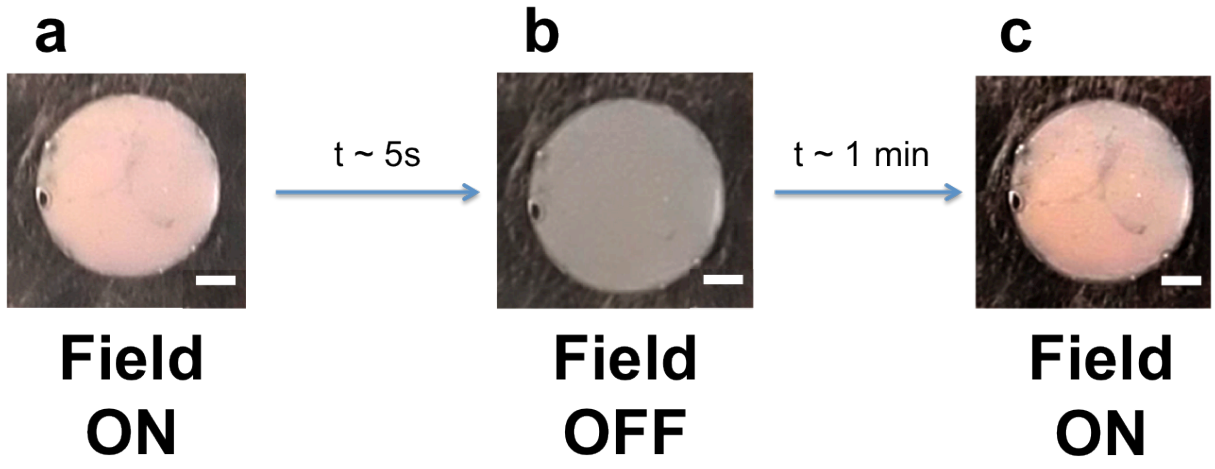


**Figure 3-5:** a. Structural color obtained for 500 nm particles on application of 2.65 V DC electric field. b. Bulk color of the sample on removal of the DC electric field after 5 seconds. c. Regeneration of structural color on application of DC electric field for 1 minute. Scale bars are 2 mm.

### 3.5. References


1. Kolle, M.; Salgard-Cunha, P. M.; Scherer, M. R. J.; Huang, F.; Vukusic, P.; Mahajan, S.; Baumberg, J. J. & Steiner, U. Mimicking the colourful wing scale structure of the Papilio blumei butterfly. *Nature Nanotechnology* **5**, 511-515 (2010).

2. McNamara, M. E.; Briggs, D. E. G.; Orr, P. J.; Noh, H. & Cao, H. The original colours of fossil beetles. *Proceedings of the Royal Society B: Biological Sciences* **279**, 1114-1121 (2012).

3. Mäthger, L. M.; Denton, E. J.; Marshall, N. J. & Hanlon, R. T. Mechanisms and behavioural functions of structural coloration in cephalopods. *Journal of the Royal Society Interface* **6**, S149-S163 (2009).

4. Geissler, M. & Xia, Y. Patterning: Principles and some new developments. *Advanced Materials* **16**, 1249-1269 (2004).

5. Pusey, P. N. & Van Megen, W. Phase behaviour of concentrated suspensions of nearly hard colloidal spheres. *Nature* **320**, 340-342 (1986).

6. Jiang, P. & McFarland, M. J. Large-scale fabrication of wafer-size colloidal crystals, macroporous polymers and nanocomposites by spin-coating. *Journal of the American Chemical Society* **126**, 13778-13786 (2004).

7. Shereda, L. T.; Larson, R. G. & Solomon, M. J. Local stress control of spatiotemporal ordering of colloidal crystals in complex flows. *Physical review letters* **101**, 038301 (2008).

8. Prevo, B. G. & Velev, O. D. Controlled, rapid deposition of structured coatings from micro-and nanoparticle suspensions. *Langmuir* **20**, 2099-2107 (2004).

9. Kleinert, J.; Kim, S. & Velev, O. D. Electric-field-assisted convective assembly of colloidal crystal coatings. *Langmuir* **26**, 10380-10385 (2010).

10. Jiang, P.; Bertone, J. F.; Hwang, K. S. & Colvin, V. L. Single-crystal colloidal multilayers of controlled thickness. *Chemistry of Materials* **11**, 2132-2140 (1999).

11. Vlasov, Y. A.; Bo, X.-Z.; Sturm, J. C. & Norris, D. J. On-chip natural assembly of silicon photonic bandgap crystals. *Nature* **414**, 289-293 (2001).

12. Furumi, S.; Fudouzi, H. & Sawada, T. Self-organized colloidal crystals for photonics and laser applications. *Laser & Photonics Reviews* **4**, 205-220 (2010).

13. Fudouzi, H. & Sawada, T. Photonic rubber sheets with tunable color by elastic deformation. *Langmuir* **22**, 1365-1368 (2006).

14. Lee, K. & Asher, S. A. Photonic crystal chemical sensors: pH and ionic strength. *Journal of the American Chemical Society* **122**, 9534-9537 (2000).

15. Arsenault, A. C.; Puzzo, D. P.; Manners, I. & Ozin, G. A. Photonic-crystal full-colour displays. *Nature Photonics* **1**, 468-472 (2007).

16. Lumsdon, S. O.; Kaler, E. W. & Velev, O. D. Two-dimensional crystallization of microspheres by a coplanar AC electric field. *Langmuir* **20**, 2108-2116 (2004).

17. Mukhija, D. & Solomon, M. J. Nematic order in suspensions of colloidal rods by application of a centrifugal field. *Soft Matter* **7**, 540-545 (2011).

18. Ahniyaz, A.; Sakamoto, Y. & Bergström, L. Magnetic field-induced assembly of oriented superlattices from maghemite nanocubes. *Proceedings of the National Academy of Sciences* **104**, 17570-17574 (2007).

19. Rogach, A. L.; Kotov, N. A.; Koktysh, D. S.; Ostrander, J. W. & Ragoisha, G. A. Electrophoretic deposition of latex-based 3D colloidal photonic crystals: A technique for rapid production of high-quality opals. *Chemistry of materials* **12**, 2721-2726 (2000).

20. Trau, M.; Saville, D. A. & Aksay, I. A. Field-induced layering of colloidal crystals. *Science* **272**, 706-709 (1996).

21. Shah, A. A.; Kang, H.; Kohlstedt, K. L.; Ahn, K. H.; Glotzer, S. C.; Monroe, C. W. & Solomon, M. J. Liquid crystal order in colloidal suspensions of spheroidal particles by direct current electric field assembly. *Small* **8**, 1551-1562 (2012).

22. Antl, L.; Goodwin, J. W.; Hill, R. D.; Ottewill, R. H.; Owens, S. M.; Papworth, S. & Waters, J. A. The preparation of poly (methyl methacrylate) latices in non-aqueous media. *Colloids and Surfaces* **17**, 67-78 (1986).

23. Russel, W. B.; Saville, D. A. & Schowalter, W. R. *Colloidal Dispersions* (Cambridge University Press, 1989).

# Chapter 4

# Synthesis, Assembly and Image Analysis of Spheroidal Patchy Particles


**Chapter Summary**

We report a method to synthesize and image Janus spheroid and "kayak" shaped patchy particles that combine both shape and interaction anisotropy. These particles are fabricated by sequentially combining evaporative deposition of chrome and gold with the uniaxial deformation of the colloidal particles into spheroids. We introduce combined reflection and fluorescence confocal microscopy to image each component of the patchy particle. Image analysis algorithms that resolve patch orientation from these image volumes are described and used to characterize self-assembly behavior. Assemblies of the Janus spheroid and kayak particles produced at different salt concentrations demonstrate the functional nature of the patch-to-patch interactions between the particles. Selective gold-to-gold patch bonding is observed at intermediate salt concentrations, while higher salt concentrations yield gel-like structures with non-selective patch-to-patch bonding. At intermediate salt concentrations, differences in the orientational order of the assemblies indicate that both the preferential gold-to-gold patch bonding and the particles' shape anisotropy influence the self-assembled structure.[27]

## 4.1 Introduction

Colloidal particles with diverse shapes and anisotropic interactions can self-assemble into structures with complex symmetries.[1] An important class of anisotropic particles is patchy colloids; that is, particles with a pairwise, orientation-dependent interaction potential. The orientation dependence of the pairwise interaction is generated by creating one or more attractive or repulsive patches on the particle surface. Patchy colloids are ideal for drug delivery applications[2] and can be used as model systems to study liquid state phenomena such as the glass transition, crystallization kinetics and spinodal decomposition.[3-5] This interest has driven the development of a number of techniques to synthesize patchy colloids.[6-9] One such method to synthesize patchy colloids is by the controlled deposition of metals (e.g., chrome and gold) on one side of a monolayer of polymer spheres.[6] This technique can be used to vary the functionality of patchy particles by creating one (e.g. Janus) or two (e.g. triblock) patches of varying patch sizes. Such particles have recently been self-assembled into structures such as Bernal spirals and kagome lattices that can be useful for membranes and filters.[3,10] Simulations and recent experiments have shown that particles with multiple patches, which have a high functionality, can assemble into diverse structures.[11,12] In this paper, we introduce a new class of functional patchy particles that have a combination of shape and patch anisotropies, and have the potential to create assemblies of complex symmetry.[13-15]

We report the synthesis of patchy colloids whose functionality is controlled by varying the patch anisotropy. This control is clearly illustrated through the concept of three anisotropy dimensions[1] of patch size, aspect ratio, and patch separation that are varied through the synthetic methods reported in this paper. These dimensions are known to affect colloidal self-assembly behavior. For example, patch coverage affects the propensity for assembly of diamond as

opposed to face centered cubic (FCC) or body centered cubic (BCC).[4,11,16] Spheroid aspect ratio controls the isotropic-nematic crystal transition.[17] Patch separation, which offsets the potential range of the patch from the particle center, affects the formation of micelles and helices in Janus sphere assemblies as well as the formation of plastic crystal phases.[18,19] Particles that combine these anisotropy dimensions have the potential to self-assemble into structures that have properties associated with each individual anisotropy dimension, or emergent properties from combinations of these dimensions, creating highly complex and tunable structures. The first class of particle we consider is a combination of the two orthogonal anisotropy dimensions of patch size and aspect ratio. We refer to this particle as a "Janus spheroid." The second class of patchy particle we report is a combination of the two orthogonal anisotropy dimensions of patch separation and aspect ratio. We refer to this patchy particle as a "kayak" because of its visual likeness to the familiar boat.

Patchy particles such as those described herein present a unique challenge for current imaging techniques. Although confocal laser scanning microscopy (CLSM) is a standard tool for imaging colloidal particle position, the quantification of particle orientation, which is necessary with anisometric and/or patchy particles, has thus far received little attention. We introduce a new and versatile imaging method using two channel CLSM to resolve all six degrees of freedom of each particle. Using this method, we quantify the anisotropic orientation of both the Janus spheroids and patchy kayak particles alone and in complex assemblies.

## 4.2 Materials and Methods

### 4.2.1 Spheroidal Particle Synthesis:

Spheroidal particles are synthesized using methods described in Shah et al.[20] Briefly, 300 μL of a 2 vol% sulfate-modified polystyrene (PS, F8851, Invitrogen Inc) particle solution is dispersed in a 7.5 mL of a 10 wt% poly (vinyl alcohol) (PVA) solution. This solution is poured into flat omni trays and allowed to dry overnight. This leads to formation of a thin film (~ 40 μm), which is pealed off the omni tray. Strips are cut out of this film, and uniaxially stretched to a strain of 2.5 at a temperature of 120 °C using our custom made stretching device. The films are then allowed to cool and resuspended in water. The PVA dissolves in water and spheroids are released in to the solution. This solution is centrifuged at 5000G for 10 minutes and then re-suspended in water at least five times to remove residual PVA from the suspension.

### 4.2.2 Sphere/Spheroid Particle Monolayer Synthesis:

300 μL of a 2-vol% solution of PS spheres / synthesized PS spheroids (F8851, Invitrogen Inc) are solvent-exchanged with 300 μL of ethanol using centrifugation. This solution of spheres/spheroids is spin coated on to a glass microscope slide (pre-soaked in a 0.1 N potassium hydroxide solution for 15 minutes (Sigma Aldrich)) at 3000 rpm for 30 seconds to create a single particle monolayer.

### 4.2.3 Substrate Modification for Assemblies:

We suspend our particles on glass substrates (glass coverslip, 35mm x 50mm x 0.13mm, Fisher Scientific) that have been treated with a potassium hydroxide base bath solution (300g

potassium hydroxide pellets (Sigma-Aldrich) dissolved in 4 L of isopropanol (Sigma-Aldrich) and 1 L of deionized (DI) water) for 2 hours.

These substrates are then further modified for patchy particles suspended at high salt concentrations (100 mM salt). A thin poly(acrylic-acid) (PAA) layer is created, which prevents the adsorption of particles onto the substrate and minimizes particle-substrate interactions, by spin coating (3000 rpm) 1 mL of a 5-wt% solution of poly(acrylic acid) (PAA, 4 million molecular weight, Sigma-Aldrich) in ethanol solution onto the coverslip.

#### 4.2.4 Patchy Particle Assembly:

~ 100 μL of patchy particles (~ 0.1 wt%) are suspended in DI water at varying sodium chloride salt concentrations. These particles are then allowed to sediment for ~ 24 hours. Most of the patchy particles are heavier than water and sediment to the coverslip. This leads to an increase in particle concentration and assembly structures form over time at the coverslip. We image our assemblies at a time of ~ 24 hours and note that there is no qualitative change in the assembly structure after 24 hours.

## 4.3. Results

#### 4.3.1.1 Janus Sphere Particle Synthesis

Janus spheres are synthesized by sequential deposition of chrome and gold on a monolayer of PS particles.[6,10] Glass microscope slides are first treated in 0.1 M KOH solutions for 10 minutes. 200 μL of a 2-vol% PS particle solution is resuspended in ethanol and spin coated on to the glass microscope slide at 3000 rpm for 30 seconds to create a single particle monolayer. This substrate is allowed to dry and then placed in an e-beam evaporator (Denton Vacuum, DV-502A). 7.5 nm

of chrome and 15 nm of gold are then sequentially deposited on the particle monolayer. A self-assembled monolayer (SAM) is created on the gold face of the particle by suspending the microscope slides in a 10 mM 8-mercaptooctanoic acid (Sigma Aldrich) solution in ethanol for at least 24 hours. The slides are taken out of this solution and thoroughly washed with deionized (DI) water. The particles are then manually swept off the surface and any particle aggregates broken up by sonication using a horn sonicator. The particles are then sequentially centrifuged at 1000G for 10 minutes and resuspended in water five times.

### 4.3.1.2 Janus Spheroid Particle Synthesis

Figure 4-1 reports the synthesis of Janus spheroids, which are particles with a single patch along the major axis of the hemispheroid of the particle. Homogeneous spheroids are first synthesized from 1.0 ± 0.03 μm polystyrene (PS) microspheres (F8851, Invitrogen Inc) using the procedure of Shah et al.[20] (Figure 4-1a). A monolayer is created from the spheroidal particles (Figure 4-1b, c.f. SI). The major axis of particles in the monolayer is oriented parallel to the glass surface. Layers of chrome (7.5 nm thickness) and gold (15 nm thickness) are then sequentially deposited on the single particle monolayers using an e-beam evaporator (Denton Vacuum, Figure 4-1c). This deposits chrome and gold preferentially on just one hemispheroid of the spheroidal particle to create Janus spheroids. The patchy surface charge and anisotropic pair potential of the particles can be tuned further by creating a self-assembled monolayer (SAM) on the gold hemispheroid through a thiol surface reaction. The SAM is produced by suspending the glass microscope slide with a monolayer of Janus spheroids in 10 mM 8-mercaptooctanoic acid (Sigma Aldrich) solution in ethanol (Decon Laboratories) for at least 24 hours. Particles are then manually swept off the microscope slide surface and particle aggregates are broken up through

sonication. The particles are stable and exhibit Brownian motion (Figure **4-**1d and Supplementary Movie (SM) 1).

Figures 4-1e-g are scanning electron microscope (SEM, Philips XL-30) images of the Janus spheroids. The brighter half of the PS spheroid in the images is coated with gold, while the other, lighter half is uncoated. Figure 4-1g shows monodisperse particles with a major axis length of 3.2 ± 0.2 μm, a minor axis length of 0.59 ± 0.05 μm and aspect ratio of 5.4 ± 0.6 (determined by image analysis of 13 particles). Figure 4-1h reports combined fluorescence and reflection imaging of dispersed Janus spheroids using confocal laser scanning microscopy (CLSM). The fluorescence channel of a metal-coated particle excites only the uncoated fluorescently labeled part of the particle.[21] The reflection channel predominantly images the gold coating on the particle because the gold and chrome metal is much more reflective than the PS component of the particle. These two channels are merged together to create a composite image, where the patches of a Janus spheroid are distinctly colored (red-PS and green-chrome and gold). Regions of the particle may appear yellow in the composite images because the red PS patch (fluorescent channel) spatially merges with the green chrome and gold coating (reflection channel), due to the resolution limits of optical microscopy. This merging is especially evident for particles with a gold patch facing away from the coverslip.

#### 4.3.1.3 Patchy Kayak Particle Synthesis

Figure 4-2 reports the synthesis of kayak particles, which are homogeneous spheroids with a patch offset from the centroid of the spheroid backbone. Kayak particles are synthesized using the scheme in Figure 4-2a-f. We first synthesize a monolayer of Janus spherical particles, as depicted in Figure 4-2a, using sequential vapor deposition of 7.5 nm of chrome followed by

15 nm of gold on a monolayer of PS microspheres (c.f. Supplementary Information (SI)). Next, a SAM is produced on the gold half of the particles by suspending the glass microscope slide with the Janus sphere monolayer in a 10 mM 8-mercaptooctanoic acid solution in ethanol for at least 24 hours. The microscope slide is then washed with DI water and placed within a cavity machined in a Teflon mold to a depth that matches the thickness of the microscope slide, leveling the particle monolayer with the surface of the mold. 12 mL of 10-weight % PVA is then poured in this mold and allowed to dry overnight (Figure 4-2a-b). This leads to formation of a thin PVA film containing the embedded Janus spheres with gold patches uniformly oriented in the film (Figure 4-2c). This alignment is essential for the synthesis of uniform kayak particles and is similar to the stamping technique that has been used to transfer monolayers between substrates.[22] The thin film is peeled off the mold and strips are cut out of this film, which are then clamped to the stretching device described in Shah et al.[20] An elongational strain of 2.5 is then applied at a temperature of 120°C (Figure 4-2d). This uniaxial deformation of the elastomeric PVA film above the $T_g$ of PS leads to formation of kayak particles (Figure 4-2e). The metallic half of the Janus particle is essentially undeformed (distorted by <10% of its initial diameter (1 μm)) during this stretching process, while the PS half of the Janus particle deforms to a spheroid of aspect ratio 4.24 ± 0.19. This effect leads to a centrally located spherical metal patch on the spheroidal half of the particle. The kayak particles are released by dissolving the PVA matrix in water once it is cooled (Figure 4-2f). The solution is vigorously sonicated using a horn sonicator (Cole-Palmer Instruments) to break up particle aggregates. For colloidal stability at high salt concentrations (100mM salt), SAMs are created again on the gold cap by dispersing the particles in a 10 mM 8-mercaptooctanoic acid in ethanol solution for 24 hours. The SAM

modified particles are then redispersed in DI water by centrifugation and we observe that the particles are stable and exhibit Brownian motion (c.f. SM 2).

Figures 4-2g-i report SEM images of kayak particles. The gold cap appears considerably brighter than the polymer spheroid in these images. Figure 4-2i shows that the kayak particles are relatively monodisperse. The relative length of the Janus spherical metal patch diameter to the polymeric spheroidal major axis length is nearly uniform at a ratio of 1:3. By analysis of 10 particles in the SEM images, the major axis length of the particle is 2.40 ± 0.15 μm. The gold patch is offset to 0.20 ± 0.01 μm from the minor axis of the spheroid, which is 0.49 ± 0.03 μm in diameter. Figure 4-2j shows the two-channel CLSM composite image of kayak particles, with the chrome and gold patch colored green, and the PS volume colored red.

#### 4.3.1.4 Patchy Kayak Raft Synthesis

Kayak rafts shown in Figure 4-7d are formed by synthesizing kayak particles (Figure 4-2). However, in this case the particles are not sonicated after redispersal in water. This change leads to the formation of kayak rafts because the physical connectivity between kayak particles that is formed during the synthesis process is not broken by sonication. The physical connectivity could be due to undissolved PVA holding the kayak particles together. Alternatively, the connectivity could be due to permanent polymer contacts formed as the specimen was heated above the glass transition temperature and then rapidly cooled to solidify the particle shape.

### 4.3.2 Patchy Particle Image Analysis

#### 4.3.2.1 Janus Sphere Image Analysis

Each component of Janus sphere particles are also uniquely imaged using reflection and fluorescence channels on the CLSM. These distinct channels are image processed to obtain all five degrees of freedom of the particle (c.f. Figure 4-3). The centroids of the overall particles are derived from the sphere algorithm applied to the uncoated PS hemisphere part of the particle (fluorescence channel). The centroids of metal hemispheres are obtained by applying the sphere algorithm to the reflection channel. A PS hemisphere centroid is then matched to a gold hemisphere centroid that is closest to their known separation as calculated from SEM images to identify a Janus sphere. The patch director is the vector that connects the centroid of the PS hemisphere to the centroid of its matched gold hemisphere. Thus, all five degrees of freedom are recovered for Janus spheres.

#### 4.3.2.2 Janus Spheroid Image Analysis

Figure 4-4 reports the particle identification method used to find the centroids and orientations of Janus spheroid particles. Figure 4-4a shows the CLSM image volume (voxel size 0.038 μm x 0.038 μm x 0.038 μm) projection of an immobilized cluster of Janus spheroid particles synthesized as per Section 3.1.2. As in previous work that report techniques to identify the centroids and directors of spheroids[23] from 3D image volumes, we assume that the brightest pixels in a spheroid image volume lie on the backbone of spheroids. We apply these algorithms to each channel of the CLSM, independently identifying individual parts of our patchy particles from the CLSM image volume. For Janus spheroid particles, the primary volumetric portion of the particle is fluorescent spheroidal PS. The particle identification method is applied to this fluorescent image to identify the particle centroid and spheroid director (Figure 4-4b and 4-4d). The centroids of the metal half of the particles are also obtained by applying the spheroid

algorithm to the reflection channel (Figure 4-4c and 4-4e). A PS spheroid centroid is then matched to a gold spheroid centroid that is closest to their known separation, as calculated from SEM images (Figure 4-1e-f). The patch director is the vector that connects the centroid of the uncoated PS to the centroid of its matched chrome and gold cap. Thus, all six degrees of freedom are recovered for Janus spheroid particles (Figure 4-4g). We assess the accuracy of this algorithm by direct comparison of the composite image (Figure 4-4a) and the rendering (Figure 4-4f). In the example here, the matching algorithm correctly identifies all the particles' centroids and orientations.

#### 4.3.2.3 Patchy Kayak Image Analysis

Figure 4-5 reports the particle identification method used to find the centroids and orientations of kayak particles. This method is similar to the procedure developed for Janus spheroids in Section 3.2.2. Briefly, Figure 4-5a shows the CLSM image volume (voxel size 0.038 μm x 0.038 μm x 0.038 μm) projection of an immobilized cluster of kayak particles synthesized as per Section 3.1.3. For kayak particles, the primary volumetric portion of the particle is fluorescent spheroidal PS. The particle centroid and spheroid director (Figure 4-4b and 4d) are identified using the spheroid tracking algorithm[23] of the CLSM image volume and the centroids of metal caps are obtained by applying the standard sphere algorithm[24] to the reflection channel (Figure 4-5c and 4-5e) of the CLSM image volume. A PS spheroid centroid is then matched to a gold cap centroid that is closest to their known separation, as calculated from SEM images (Figure 4-2g-h). We match particles from the fluorescent channel and patches from the reflection channel by gathering pairs of spheroids (detected from the fluorescence channel) and patches (detected from the reflection channel) that are closer than a cutoff radius to a target

separation that we measure from SEM images. We iterate through these pairs, starting with the pair that is closest to the target separation. If both the patch and the spheroid have not been identified as part of a patchy particle, then they are matched and marked as a pair. Once we have iterated through all such pairs, we take any remaining, unmatched spheroids and place the patch behind the spheroid towards the substrate, assuming that the golden cap of a kayak particle was not imaged because it was completely obscured by the substrate. CLSM images indicate that this is a sound assumption, as the reflection channel does not pick up the particle's gold caps for this particular particle configuration. After this step, any remaining unmatched gold caps are residual free floating gold flakes suspended in solution and are discarded (always less than 10% of the total number of particles). The patch is placed in the bisecting plane of the uncoated PS spheroid, such that the director points from the centroid of the uncoated PS spheroid to the centroid of its matched gold cap recovering all six degrees of freedom for kayak particles (Figure 4-5f). We assess the accuracy of this algorithm by direct comparison of the composite image (Figure 4-5a) and the rendering (Figure 4-5f). In the example here, the matching algorithm correctly identifies all the particles' centroids and orientations.

### 4.3.3 Patchy Particle Assembly and Image Volume Analysis

Images and characterization of the self-assembly behavior of the Janus spheroid and patchy kayak particles are reported in Figures 4-6 and 4-7, respectively. We apply the image analysis tools introduced in Section 3.2 to render and statistically analyze the assemblies. Both patchy kayaks and Janus spheroids are negatively charged and pairwise repulsive under conditions of no added electrolyte (c.f. SM 1 and SM 2). Consequently, there is no pair binding observed. However, this charge is screened and the electrostatic repulsion is reduced upon the

addition of salt. We suspend our particles in two different salt concentrations (2.5 mM (Debye length 6 nm, c.f. SI) and 100 mM (Debye length 0.95 nm, c.f. SI) sodium chloride in water) and report the resulting assemblies in Sections 3.3.1 and 3.3.2.

#### 4.3.3.1 Janus Spheroid Particle Assembly and Analysis

Figure 4-6 shows the assembly structures obtained for Janus spheroid particles at two different salt concentrations (100 mM and 2.5 mM salt) formed using methods described in Section 3.1.1. Figure 4-6a shows the disordered, gel-like assembly structure obtained for Janus spheroid particles (aspect ratio 5.4) suspended at high salt concentrations (100 mM salt). We image these assemblies at the same resolution as in Figure 4-4. We analyze a region of interest of that assembly in Figure 4-6b and render the results of the image analysis in Figure 4-6c. The gold-to-gold patch bonding in that structure is computed in Figure 4-6d. The green bonds represent gold-to-gold patch bonding, and the red bonds represent non gold-to-gold bonds. There is no significant preference for gold-to-gold patch bonding as is quantitatively evident in Figure 4-6i.

In Figures 4-6e-h, we analyze an assembly of Janus spheroids (aspect ratio 5.4) at 2.5 mM NaCl salt concentrations. Figure 4-6e shows an assembly obtained at this intermediate salt concentration. We analyze a representative section of this structure (Figure 4-6f) and use image analysis to render the assembly structure in Figure 4-6g. The gold-to-gold patch bonding is computed in Figure 4-6h. In this case, there is a significant preference for gold-to-gold patch bonding (Figure 4-6i).

We compare the fraction of gold-to-gold bonds to the total particle bonds obtained for these two assembly conditions in Figure 4-6i. Particles are considered bonded if their surface

separation is < 0.5 μm. Our analysis shows that 75% of the total bonds are gold-to-gold bonds for intermediate salt concentrations while only 26% of the total bonds are gold-to-gold for high salt concentration. This demonstrates the gold-to-gold patch bonding functionality of Janus spheroids at intermediate salt concentrations. In contrast, the whole particle is attractive at high salt concentrations and there is no gold patch functionality. Here, we note that particles will have a majority of gold-to-gold contacts when the gold-to-gold patch bond is attractive, but are still expected to have a non-zero fraction of non gold-gold contacts because of geometric considerations. In these locally dense configurations non-specifically bonded particles will be within our bonding cutoff even if their patches aren't bonded to one another. The abundance of non-specific contacts depends on the resulting assembly morphology and particle geometry.

We also compare the orientational order of the particles in the assemblies formed at intermediate and high salt concentrations. We compute the orientational order of the PS spheroids with a local alignment order parameter (Ψ).

$$\Psi = \frac{1}{N_p}\sum_{i=0}^{N_p}\frac{1}{N_{NN,i}}\sum_{j=0}^{N_{NN,i}}(\vec{n}_i \cdot \vec{n}_j)^2$$

Here, $N_p$ is the number of particles, $N_{NN,i}$ is the number of nearest neighbors and $n_i$, nj is the gold patch normal vectors of spheroids i and j, respectively. This parameter varies between 0 and 1: Ψ=0 if particles are orthogonal to their neighbors, Ψ=1/2 if they are randomly oriented and Ψ=1 if they are aligned. The gel-like assemblies obtained at high salt concentrations are randomly oriented (Figure 4-6a-d) with Ψ = 0.34±0.06. In contrast, the assemblies obtained at intermediate salt concentrations are highly oriented with Ψ = 0.98±0.003. We note that the patch bonding along the major axis of the Janus spheroids induces local orientational alignment at intermediate salt concentrations.

#### 4.3.3.2 Patchy Kayak Particle Assembly and Analysis

Figure 4-7 shows the assembly structures obtained at two different salt concentrations (100 mM and 2.5 mM salt) for patchy kayak particles obtained using methods described in Section 3.1.3. We observe the formation of disordered, gel-like assembly structures for patchy kayak particles (aspect ratio 3) in Figure 4-7a. We analyze a small section of the resulting assembly in Figure 4-7b, and render the coordinates of the particles in the self-assembly in Figure 4-7c, as obtained from image analysis. The number of gold-to-gold patch bonds to the total particle contacts is reported in Figure 4-7d. Figure 4-7i shows that there is no preference for gold-to-gold alignment in this configuration.

In Figures 4-7e-h, we analyze an image volume of a kayak particle (aspect ratio 2.5) assembly at 2.5 mM NaCl salt concentration. In this case, there is significant preference for gold-to-gold patch bonding as is evident in Figure 4-7i.

We compare the fraction of gold-to-gold bonds to the total particle contacts obtained for these two assembly conditions in Figure 4-7i. Our analysis shows that the 62% of bonds are gold-to-gold bonds at intermediate salt concentrations while only 12% are gold-to-gold at high concentrations. This comparison demonstrates preferential site bonding of patchy kayaks at intermediate salt concentrations.

We also compare the orientational order of the kayaks in the assemblies obtained at intermediate and high salt concentrations. The orientational order parameter ($\Psi$) is 0.34±0.08 for the assemblies obtained at high salt concentrations (Figure 4-7a-d), while $\Psi$ is 0.52±0.07 for the assemblies obtained at intermediate salt concentrations. Thus, there is no orientational alignment

in either sample. We note that the kayaks' patches are clearly bonded, but the particles are still free to rotate about that bond, resulting in limited orientational alignment.

#### 4.3.3.3 Bulk Assembly Structure Analysis through Image-Processing

The image analysis algorithms developed in Section 3.2 are capable of analyzing bulk structural properties of large-scale assemblies. In Figure 4-9, we analyze our gel-like disordered assemblies using the image analysis algorithms developed in this paper. The gel-like assemblies are large, multi-layer structures that assemble into interconnected bundles over 24 hours (c.f. Figure 4-8). Figure 4-9a-c depicts projections of Janus sphere, Janus spheroid and kayak particle assemblies respectively, obtained by suspending particles in a 100 mM NaCl solution, and placed on a coverslip with a thin PAA coating. We produce ordered bulk assemblies pictured in Figure 4-9d using the same procedure described in Section 3.1.3 to contrast our results from the gel-like assembly structures. In this case, the particles are not sonicated after redispersal in water. This leads to the formation of kayak rafts. Results of the patchy particle identification are shown in Figure 4-9e-h. There is very good visual agreement between the assembly structure and results of particle identification. The algorithms misidentified < 5% of particles.

We also report the orientation order parameter (S) of the patch directors, which is a measure of their degree of alignment (Figure 4-9e-h). The patch director is calculated by drawing a vector from the centroid of the uncoated PS body to the centroid of the coated patch. S is defined as the largest eigenvalue of the orientation angle tensor (**Q**) of all such patch directors.

$$Q = \frac{1}{N}\sum_{i=0}^{N}\frac{3}{2}\vec{n}_{patch}(\vec{r}_i)\otimes\vec{n}_{patch}(\vec{r}_i) - \frac{1}{2}\mathbb{I} \quad (2)$$

where $n_r$ is the number of particles in the image volume, $\vec{n}_{patch}(\vec{r}_i)$ is the patch director of the $i^{th}$ particle at position $\vec{r}_i$, $\otimes$ is the direct product and **I** is the identity tensor. The order parameter varies from 0 (all the patch directors are disordered) to 1 (all the patch directors are aligned). The patch directors in Figure 4-9a-c are nearly randomly oriented, as evident from their low order parameters (S < 0.2, Figure 4-9e-g), while the patch directors of the particles in Figure 4-9d are aligned (S = 0.92, Figure 4-9h). The inset plots of Figure 4-9e-g show a histogram of the patch directors projected on the unit sphere (stereographic projection). A cluster of points on the sphere indicates patch alignment, while scattered points indicate random orientation of directors. In Figure 4-9e, the cluster of points shown in the inset stereographic projection indicates partial alignment. The projections of Figure 4-9f-g show no such cluster of points for the spheroid and kayak samples, indicating random patch alignment, while the inset plot of Figure 4-9h shows almost total alignment. This suggests that the tendency of patch-to-patch alignment is negligible at high salt concentrations in the formation of gel-like structures as seen in Figure 4-9.

We also compute a pair correlation function (Figure 4-10) between the patch directors for all the assemblies in Figure 4-9 of the main text. We define the correlation function C(r) as,

$$C(r) = C\left(\left|\vec{r}_i - \vec{r}_j\right|\right) = \left\langle \vec{n}_{patch}(\vec{r}_i) \cdot \vec{n}_{patch}(\vec{r}_j) \right\rangle \tag{3}$$

where $C(r)$ is 0 if there is no correlation between the patch directors, 1 if the patches are aligned and -1 if the patches are anti-aligned. A tight cluster of points on the surface of the sphere indicates patch alignment, while a distribution of points on the sphere indicates random orientation of patch directors. The Janus spheres show partial patch alignment over the sample in

Figure 4-9a of the main text. This partial alignment is easily visualized by the cluster of points in the director histogram shown in the inset stereographic projection (Figure 4-10a). Figure 4-10b and Figure 4-10c show no correlation in patch alignment for the spheroid (Figure 4-9b main text) and kayak samples (Figure 4-9c main text). Figure 4-10d easily distinguishes the artificially assembled kayak structure (Figure 4-9d main text) as the most aligned, $C \cong 1$ at all separation distances.

#### 4.3.3.4 Error Analysis

Errors in our computer-aided identification of patchy particle position and orientation can arise from three possible sources: error in processing the reflection channel (which locates the patch), error in processing the fluorescent channel (which locates the particle position as well as azimuthal and polar orientation), and error in matching the two channels together (which recovers the patch director/axial orientation).

First, we characterize the static errors that arise from confocal microscopy and subsequent image processing by calculating the root mean square (RMS) variations in particle positions and orientations of a static sample. Janus spheroids are suspended in a 100 mM sodium chloride salt solution and allowed to sediment to the substrate. The high salt concentration causes the particles to adhere irreversibly to the substrate. We choose a small section of this sample (12 particles, voxel size 0.038 x 0.038 x 0.038 μm) and image this same volume five times. Subsequently, we use image-processing algorithms on each of these five volumes to identify the centroid and orientation angles of these particles. We then subtract the center of mass drift for all our centroids over the five image volumes, and calculate the RMS deviations from the mean

particle position and orientation. The centroidal error is found to be ± 0.06 μm, and the orientational error is ± 7°. This is consistent with the values reported in Mukhija and Solomon.[17]

We also evaluate the possible error in patch orientation of the assembly reconstructions of Figure 4-9 in the main text. We calculate this error by comparing the ideal patch position and patch-particle centroid separation obtained from the SEM images with the output of the particle identification algorithms (c.f. Table 4-1). For Janus spheres, we calculate the RMS value (Δr) of the difference of the separation of the matched sphere centroids (obtained from reflection and fluorescent channel image processing) from their ideal separation (0.5 μm, from SEM images). We calculate the angle swept out by moving Δr perpendicular to the patch director at the ideal particle patch separation ($\tan\Delta\varphi \sim \Delta\varphi = \Delta r/dr_0$) to estimate the uncertainty in the patch position. For Figure 4-9a of the main text, this error is found to be 22° (c.f. Table 4-1).

We evaluate the accuracy of our Janus spheroids and kayak patch director orientations in a similar fashion, but include the additional orientational information of these particles (obtained from the fluorescent channel). For Janus spheroids, we expect ideal matches to have parallel PS and gold components and have a center-to-center separation of 0.30 ± 0.03 μm. The orientational uncertainty includes the uncertainty from the spheroid identification algorithm, the RMS difference in the director orientations of the patch and particle and the orientational coupling of the radial uncertainty (identical to Janus spheres). For Figure 4-9b of the main text, this error is found to be 27°. For the kayak particles, we expect ideal matches to have a PS spheroid center to gold patch center separation of 0.20 ± 0.01 μm and for the gold patch the lie on the plane bisecting the PS spheroid. The orientational uncertainty includes the uncertainty from the spheroid identification algorithm, the RMS angle between the patch and the bisecting plane of the PS spheroid and the orientational coupling of the radial uncertainty (again, the same as the

Janus spheres). For Figure 4-9c and 4-9d of the main text, we find this error to be 31° and 16° respectively.

We find that in all cases we can resolve the patch director to within an octant. We stress that the current method is therefore sufficient for structural identification and detection of patch-to-patch "bonding" (e.g. identifying the kagome lattice, micelles, and vesicles). However, improvements in reflection channel imaging, which we identify as the major source of error, are necessary to more precisely locate the patch, as would be required, for example, for studies of rotational dynamics.[26]

### 4.4. Discussion

The synthesis of patchy kayak and Janus spheroids that incorporate both shape and interaction anisotropy have been reported. Imaging methods and image analysis algorithms have been developed to identify all 6 degrees of freedom of these patchy particles. We used the image-analysis methods to quantify the selectivity of gold-to-gold patch bonding and analyze patchy particle assembly structures under different assembly conditions.

The synthesis method used to make patchy kayak and Janus spheroid particles is versatile and easily generalizable to other types of anisotropic Janus particles. For example, the aspect ratio of both the Janus spheroid and patchy kayak particles can be changed easily by varying the elongational strain.[17] The patch size of the Janus spheroid and patchy kayaks could be varied using methods such as glancing angle deposition.[6] The patch separation of the patchy kayaks could also be varied by using dicolloids with varying patch separations as synthesized by Mock et al.[25] Thus, the methods introduced in this paper can be used to synthesize anisotropic patchy

particles with variable anisotropy dimensions. Approximately $10^9$ particles are synthesized per experiment using our current methods and these methods could be scaled upward as necessary.

Patchy kayak and Janus spheroid particles both show gold-to-gold patch bonding at intermediate salt concentrations in Figures 4-6 and 4-7. At intermediate salt concentrations, the screening of the electrostatic charges is apparently sufficient for the gold-to-gold interaction to be attractive, while gold-to-PS and PS-to-PS interactions are still repulsive. At high salt concentrations, the screening of electrostatic repulsive charges is sufficient for all the possible particle bonds (gold-to-gold, gold-to-PS and PS-to-PS) to be attractive. Hence, there is no preference for gold-to-gold patch bonding at high salt concentrations. This result indicates that the pair potential of these particles can be tuned by adding salt to the system. The sensitivity of the relative bond propensity to electrolyte concentration may be due to a number of reasons. Potential determinants of the sensitivity include a difference in van der Waals attractions between gold and latex surfaces, a difference in the relative charge density of the gold and latex surfaces, or the presence of the 8-mercaptooctanoic acid self-assembled monolayer on the gold surfaces of the Janus particles. This study's observation of a functional sensitivity to electrolyte concentration would motivate future work to distinguish the relative role of these potential contributions to the propensity for gold-gold bonding Janus particles.

While there is significant gold-to-gold patch bonding in both particles at intermediate salt concentrations, the resultant assemblies are very different. Specifically, the spheroid director orientational order parameter is high for Janus spheroids (0.98), indicating that the particles are aligned in their assemblies. It is low for patchy kayak particles (0.52), indicating that the orientation of the PS spheroid component is nearly random in assemblies. This comparison indicates that the gold-to-gold patch bonding induces more orientational order in Janus spheroids

than in the patchy kayak particles. Janus spheroids are bonded along their major axis, which limits the orientational freedom of the spheroid and forces the Janus spheroids into orientationally ordered structures. By contrast, the kayaks are bonded by their spherical gold patches. This does not constrain the spheroid half of the particle, which is free to rotate about the bond. Consequently, while both the patchy kayaks and Janus spheroids show strong gold-to-gold patch bonding at intermediate salt concentrations, only Janus spheroids show orientational order at intermediate salt concentrations. We find, therefore, that the structures obtained by assembling patchy kayaks and Janus spheroids are very different. Patch anisotropy, in conjunction with shape anisotropy, both affect the final self-assembled structure.

### 4.5. Conclusions

We have reported a synthesis scheme for a new class of patchy particles that combines patch size, aspect ratio and patch separation anisotropy dimensions. From among these possibilities, we specifically synthesized patchy kayak and Janus spheroid particles. Two channel CLSM was used to resolve the anisotropic orientation of these particles in their self-assemblies. Image analysis routines were used to quantify all six degrees of freedom of the patchy particles. These imaging and computer aided identification techniques have potentially broad application to the study of anisotropic patchy particles and their assemblies. They were used in the present work to characterize the functionality of the patchy particles and their assemblies. We show that the assemblies of patchy kayaks and Janus spheroids are dependent on their propensity for gold-to-gold patch bonding as well as the shape of the particle. The particle synthesis, and image-processing methods introduced in this paper can potentially be extended to magnetic and catalytically active particles.

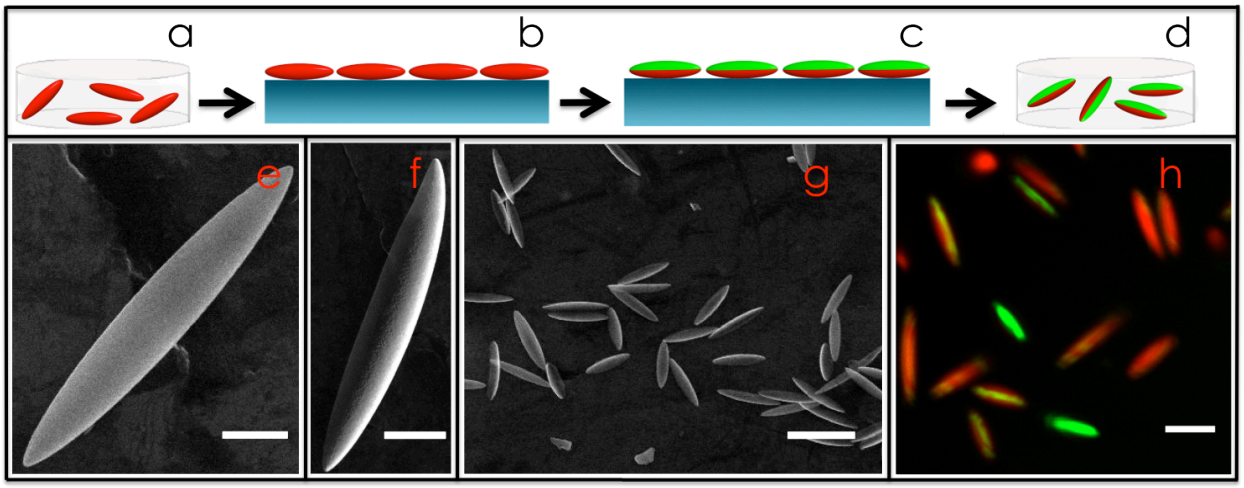


**Figure 4-1:** a-d) Schematic of Janus spheroid particle synthesis. SEM e) top view f) side view g) Zoomed-out view. h) Two-channel CLSM image. Scale bar: e,f) 0.5 μm and g,h) 3 μm.

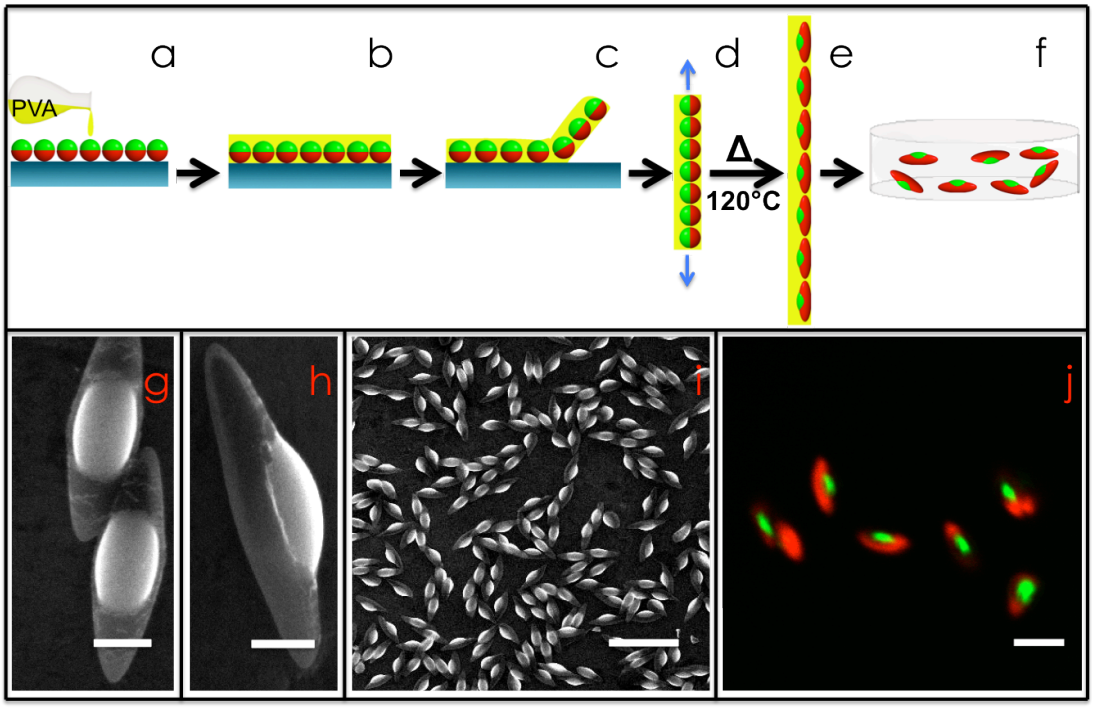


**Figure 4-2:** a-f) Schematic of kayak particle synthesis. SEM g) Top view h) Side view i) Zoomed-out view. j) Two-channel CLSM image. Scale bar: g, h) 0.5 µm i) 5 µm and j) 3 µm.

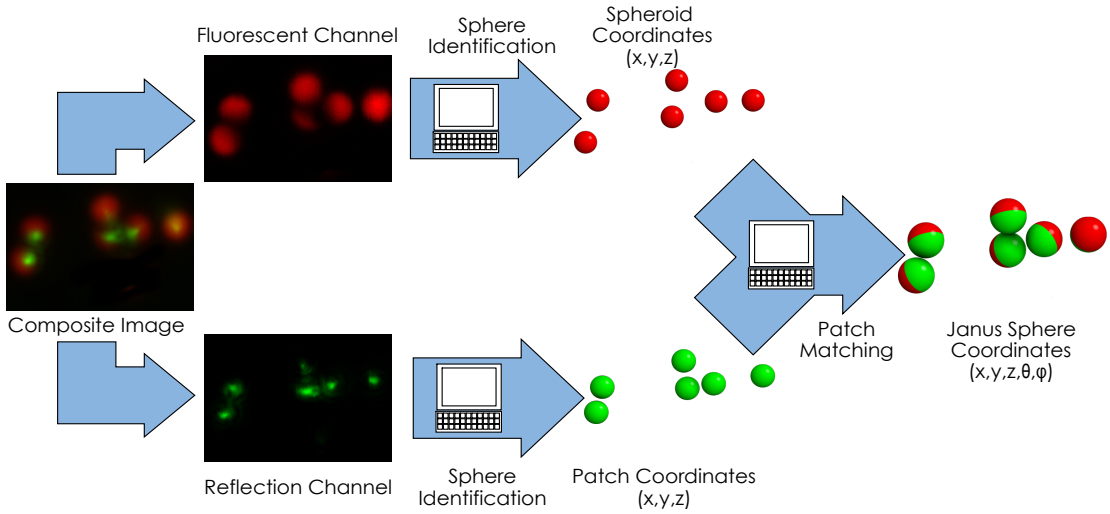


**Figure 4-3:** Janus sphere particle identification schematic.

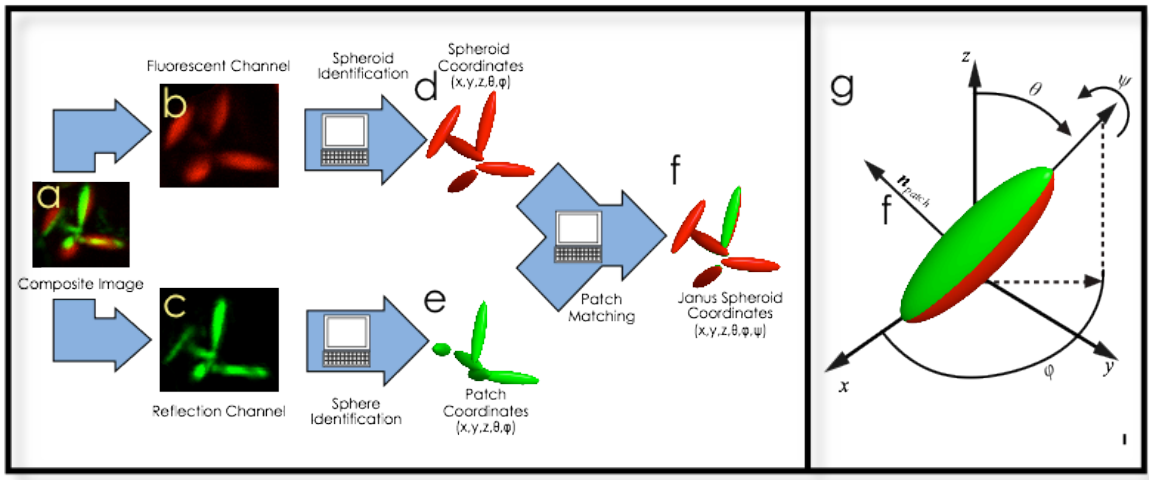


**Figure 4-4:** a-f) Janus spheroid image analysis schematic. Microscopy images are 2D maximum projections of the rendered image volume. g) The director ($\mathbf{n}_{\text{patch}}$) and orientation angles ($\theta,\phi,\psi$) identified by image analysis algorithms.

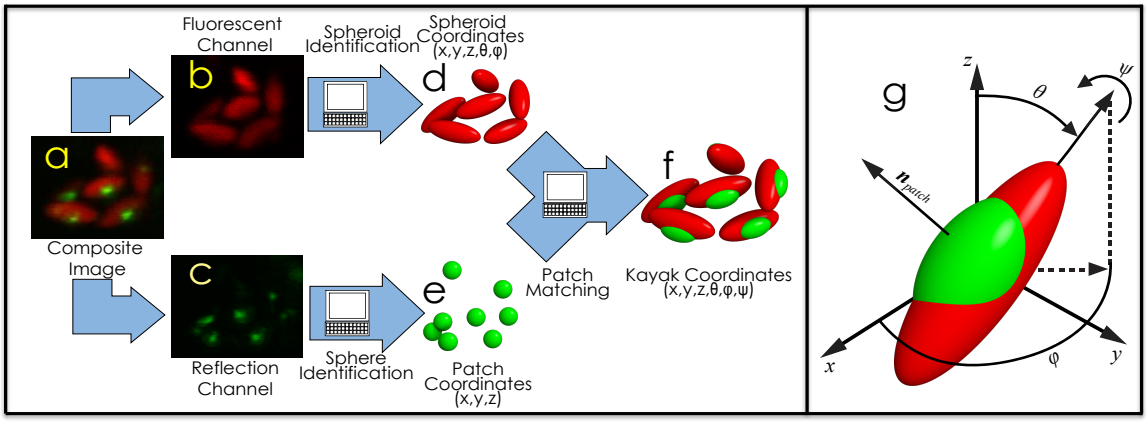


**Figure 4-5:** a-f) Patchy kayak image analysis schematic. Microscopy images are 2D maximum projections of the rendered image volume. g) The director ($\mathbf{n}_{\text{patch}}$) and orientation angles ($\theta$,$\phi$,$\psi$) identified by image analysis algorithms.

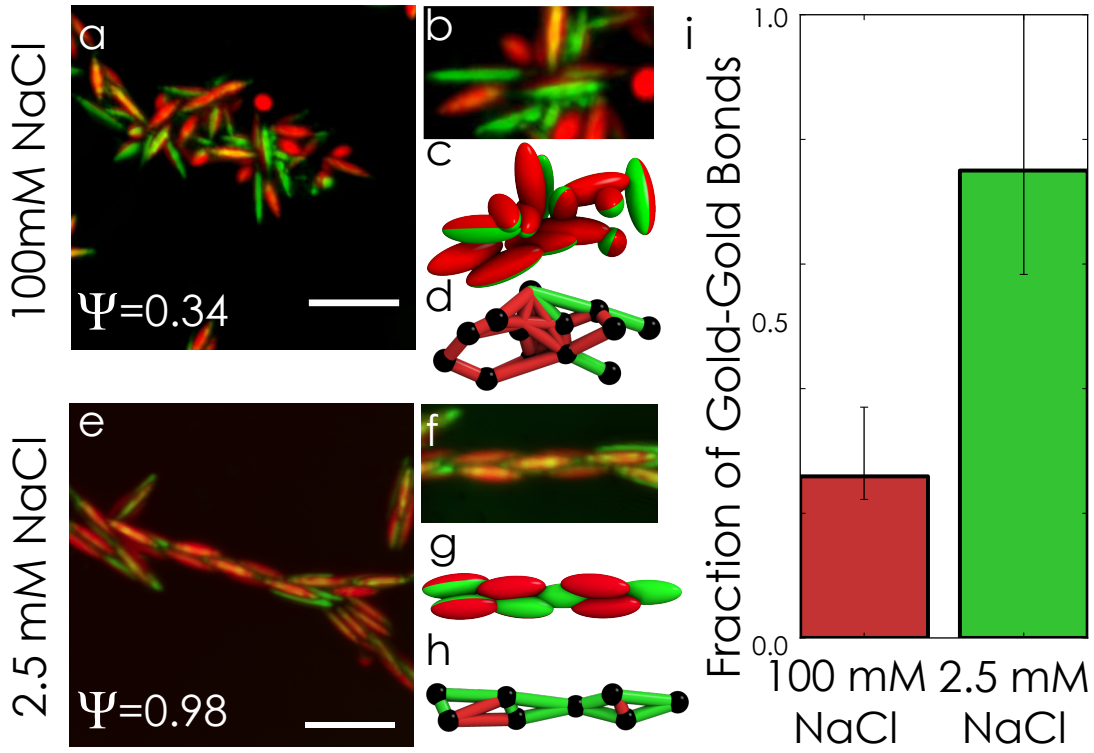


**Figure 4-6:** a) CLSM image of Janus spheroid particles suspended in 100 mM salt. The order parameter of the self-assembly (c.f. text) is provided in the image. b) Representative section of that assembly enlarged and rotated. c) Corresponding image-processed rendering. d) Corresponding bonding figure. e) CLSM image of Janus spheroid particles suspended in 2.5 mM salt. The computed order parameter is shown in the image. f) Representative section of that assembly enlarged and rotated. g) Corresponding image-processed rendering. h) Corresponding bonding figure. i) Graph of the fraction of gold-to-gold bonds to total particle contact bonds for intermediate and high salt concentrations. Scale bar: a, e) 5 μm.

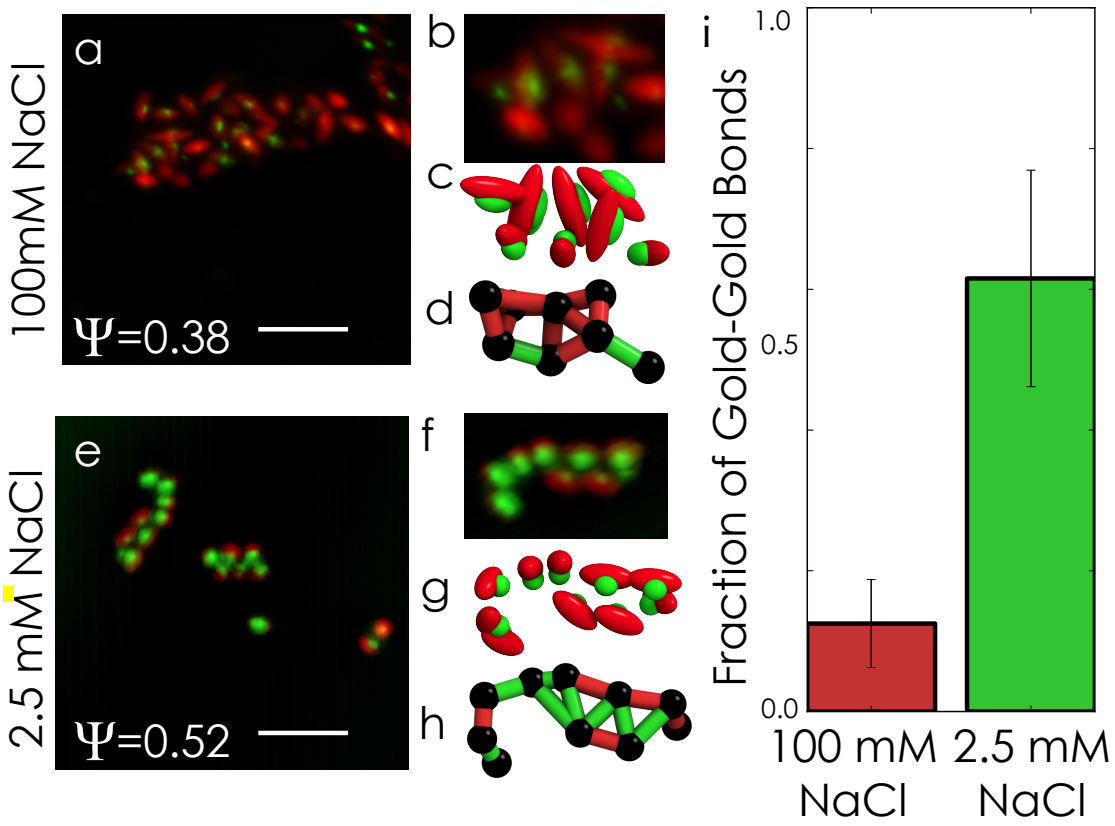


**Figure 4-7:** a) CLSM image of self-assembly of patchy kayak particles suspended in 100 mM salt. The order parameter is shown in the image inset b) Representative section of that assembly, enlarged and rotated. c) Corresponding image-processed rendering. d) Corresponding bonding figure. e) CLSM image of Janus spheroid assembly suspended in 2.5 mM salt. The order parameter is shown in the image inset. f) Representative section of that assembly enlarged and rotated. g) Corresponding image-processed rendering. h) Corresponding bonding figure. i) Graph of the fraction of gold-to-gold bonds to total particle contact bonds for intermediate and high salt concentrations. Scale bar: a, e) 5 μm.

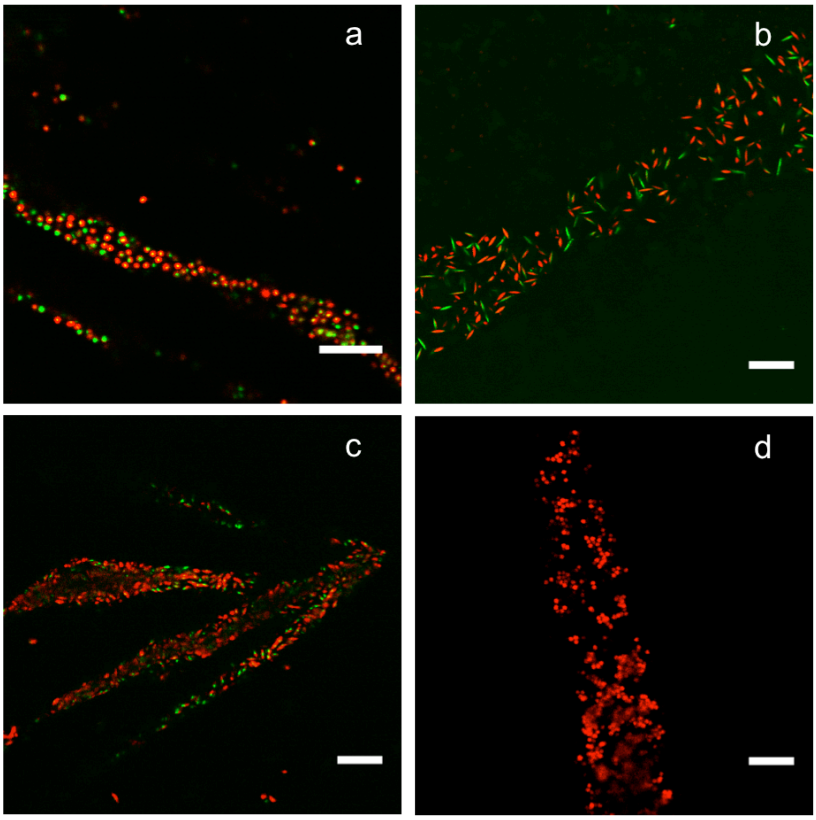


**Figure 4-8:** Zoomed out assembly images of a. Janus Spheres b. Janus Spheroid c. Kayak particles. d. Polystyrene spheres. Assemblies created using methods described in Figure 4-7 (main text). Scale bars 10 μm.

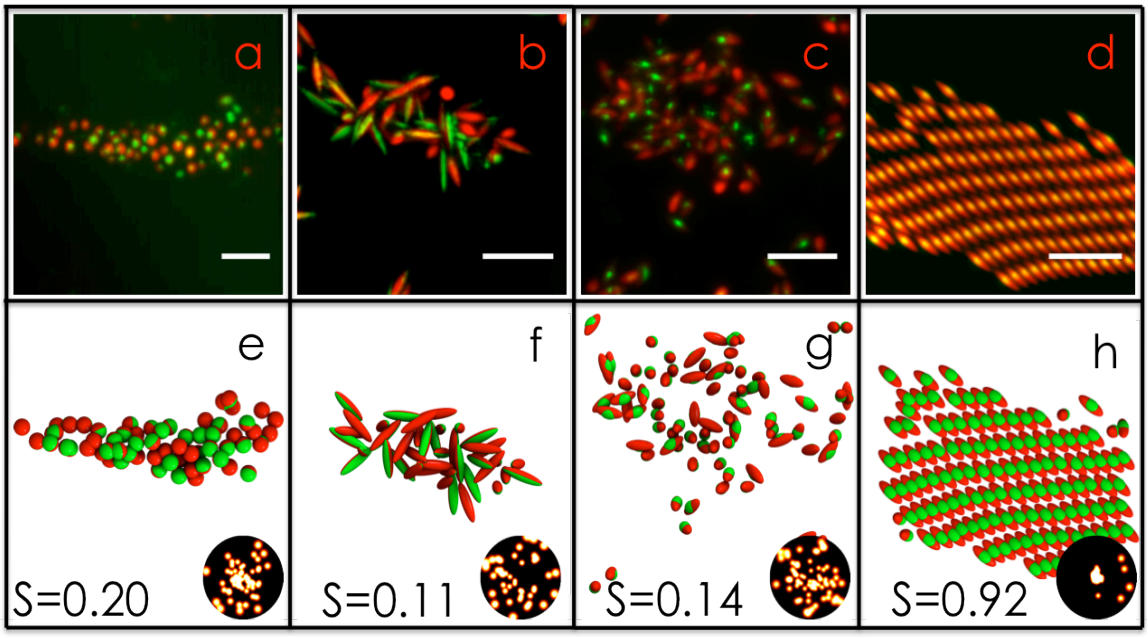


**Figure 4-9:** a-d) CLSM images of disordered assemblies of Janus sphere, Janus spheroid, patchy kayak particles and ordered kayak rafts. Assemblies are created at a 100 mM sodium chloride salt concentration. e-h) Renderings of the corresponding assemblies. Order parameter (S) and stereographic projections of the patch directors are also shown (c.f. main text). Scale bar: a-d) 5 μm.

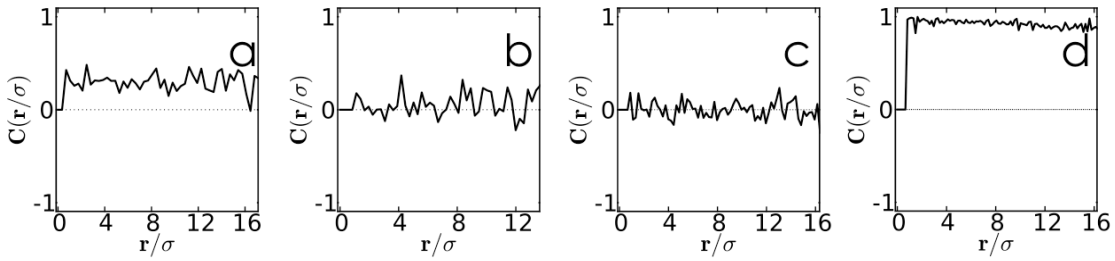


**Figure 4-10:** Janus Particle Assembly (Figure 4-9) correlation functions.

**Table 4-1:** Schematic and RMS value of the patch orientation error calculated for the image volumes shown in Figure 4-6 of the main text.

| | Particle | Schematic | $\Delta\varphi$ |
|---|---|---|---|
| 1 | Janus Sphere | 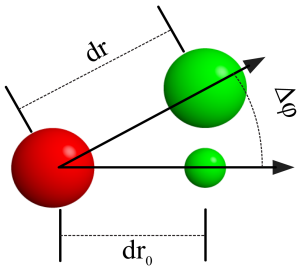  | 22° |
| 2 | Janus Spheroid | 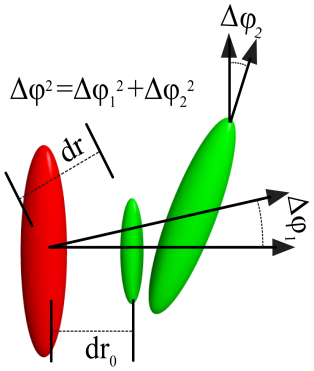  | 27° |
| 3 | Disordered Kayak | 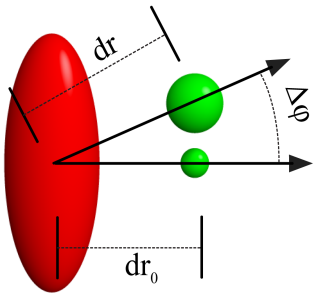  | 31° |
| 4 | Ordered Kayak | | 16° |

## 4.6. References


1. Glotzer, S. C. & Solomon, M. J. Anisotropy of building blocks and their assembly into complex structures. *Nature Materials* **6**, 557-562 (2007).

2. Mitragotri, S. & Lahann, J. Physical approaches to biomaterial design. *Nature Materials* **8**, 15-23 (2009).

3. Chen, Q. et al. Supracolloidal reaction kinetics of Janus spheres. *Science* **331**, 199-202 (2011).

4. Romano, F., Sanz, E. & Sciortino, F. Phase diagram of a tetrahedral patchy particle model for different interaction ranges. *J Chem Phys* **132**, 184501 (2010).

5. Sciortino, F. Gel-forming patchy colloids and network glass formers: thermodynamic and dynamic analogies. *The European Physical Journal B-Condensed Matter and Complex Systems* **64**, 505-509 (2008).

6. Pawar, A. B. & Kretzschmar, I. Multifunctional Patchy Particles by Glancing Angle Deposition. *Langmuir* **25**, 9057-9063 (2009).

7. Dendukuri, D., Pregibon, D. C., Collins, J., Hatton, T. A. & Doyle, P. S. Continuous-flow lithography for high-throughput microparticle synthesis. *Nature Materials* **5**, 365-369 (2006).

8. Park, B. J., Brugarolas, T. & Lee, D. Janus particles at an oil-water interface. *Soft Matter* **7**, 6413-6417 (2011).

9. Bhaskar, S. et al. Engineering, Characterization and Directional Self-Assembly of Anisotropically Modified Nanocolloids. *Small* **7**, 812-819 (2011).

10. Chen, Q., Bae, S. C. & Granick, S. Directed self-assembly of a colloidal kagome lattice. *Nature* **469**, 381-384 (2011).

11. Zhang, Z. & Glotzer, S. C. Self-assembly of patchy particles. *Nano Letters* **4**, 1407-1413 (2004).

12. Wang, Y. et al. Colloids with valence and specific directional bonding. *Nature* **491**, 51-55 (2012).

13. Liu, Y., Li, W., Perez, T., Gunton, J. D. & Brett, G. Self Assembly of Janus Ellipsoids. *Langmuir* **28**, 3-9 (2012).

14. Chaudhary, K., Chen, Q., Juarez, J. J., Granick, S. & Lewis, J. A. Janus Colloidal Matchsticks. *Journal of the American Chemical Society* **0**, (0).

15. Zhang, Z., Pfleiderer, P., Schofield, A. B., Clasen, C. & Vermant, J. Synthesis and Directed Self-Assembly of Patterned Anisometric Polymeric Particles. *Journal of the American Chemical Society* **133**, 392-395 (2011).

16. Noya, E. G., Vega, C., Doye, J. P. K. & Louis, A. A. The stability of a crystal with diamond structure for patchy particles with tetrahedral symmetry. *J Chem Phys* **132**, 234511 (2010).

17. Mukhija, D. & Solomon, M. J. Nematic order in suspensions of colloidal rods by application of a centrifugal field. *Soft Matter* **7**, 540-545 (2011).

18. Mock, E. B. & Zukoski, C. F. Determination of static microstructure of dilute and concentrated suspensions of anisotropic particles by ultra-small-angle X-ray scattering. *Langmuir* **23**, 8760-8771 (2007).

19. Li, Z. W., Lu, Z. Y., Sun, Z. Y. & An, L. J. Model, self-assembly structures, and phase diagram of soft Janus particles. *Soft Matter* **8**, 2693-2697 (2012).

20. Shah, A. A. et al. Liquid Crystal Order in Colloidal Suspensions of Spheroidal Particles by Direct Current Electric Field Assembly. *Small* **8**, 1551–1562 (2012).

21. Anthony, S. M., Kim, M. & Granick, S. Single-particle tracking of janus colloids in close proximity. *Langmuir* **24**, 6557-6561 (2008).

22. Ahn, J. H. et al. Heterogeneous three-dimensional electronics by use of printed semiconductor nanomaterials. *Science* **314**, 1754-1757 (2006).

23. Mohraz, A. & Solomon, M. J. Direct visualization of colloidal rod assembly by confocal microscopy. *Langmuir* **21**, 5298-5306 (2005).

24. Crocker, J. C. & Grier, D. G. Methods of digital video microscopy for colloidal studies. *Journal of Colloid and Interface Science* **179**, 298-310 (1996).

25. Mock, E. B., De Bruyn, H., Hawkett, B. S., Gilbert, R. G. & Zukoski, C. F. Synthesis of anisotropic nanoparticles by seeded emulsion polymerization. *Langmuir* **22**, 4037-4043 (2006).

26. Gary, L. H., Kazem, V. E., Mark, T. E. & Eric, R. W. Tracking rotational diffusion of colloidal clusters. *Opt. Express* **19**, 17189–17202 (2011).

27. Shah, A. A.; Schultz, B.; Kohlstedt, K. L.; Glotzer, S. C. & Solomon, M. J. Synthesis, assembly, and image analysis of spheroidal patchy particles. *Langmuir* **29**, 4688-4696 (2013).

# Chapter 5

# Actuation of one-dimensional shape-memory colloidal assemblies of Janus ellipsoids

**Chapter Summary**

Recent advances in the assembly of micron-scale colloidal particles have produced ordered structures with complex symmetry from close-packed cubic crystal structures to ordered open structures like Kagome lattices. Self-assemblies have also been reconfigured between crystal structures through martensitic transformations commonly seen in metals. However, these synthetic colloidal structures do not have the complex functionality displayed by micron-scale self-assemblies in nature, which can be actuated to control optical, transport, and mechanical properties. Muscles, for example, are made of bundles of myofibrils that are structured as one-dimensional, ordered micron-scale chains. Myofibrils relax and contract on actuation through the sliding motion of sarcomere subunits that are approximately two microns in size. We use ordered, one dimensional structure of muscle myofibrils as inspiration to create shape-memory colloidal assemblies that can be actuated. We used Janus ellipsoids as building blocks to assemble self-limiting one-dimensional chains. The unit cell of this ordered assembly permits reconfiguration of the positional order of the ellipsoids via a sliding mechanism upon micro-

scale actuation by alternating current (AC) electric fields. This actuation, an emergent property of Janus ellipsoid self-assemblies, permits the reversible elongation of the Janus ellipsoid assembly chain length (by ~ 36%) at short-time scales, comparable to normal elongation of human muscles. Actuation of synthetic Janus ellipsoid assemblies on long time scales further leads to the generation of long, uniform self-assembled chains.

## 5.1. Introduction

The equilibrium self-assembly of patchy particles[1] with anisotropic interactions[2] has shown great versatility in the assembly of structures useful for photonics[1], catalysis[3] and drug delivery[4]. Recent studies have shown that the assembly of shape-anisotropic patchy particles can lead to the generation of liquid crystal phases with orientational order.[5-7] We find that Janus ellipsoids, whose geometry is distinct from the more commonly studied case of spherocylinders[8], self-assemble into orientationally and positionally ordered, one-dimensional, self-limiting chains. The unique positional and orientational order of the Janus ellipsoid self-assembly, a consequence of the curved, quadratic surface of the ellipsoids, is instrumental in facilitating sliding motion similar to muscle myofibrils on actuation by AC electric fields.

AC electric fields have been widely used to create 1D chain-like structures and close-packed 2D assemblies from simple colloidal spheres[9] as well as to assemble patchy spherical colloids into staggered and zig-zag chain structures[10]. AC electric fields have also been used in conjunction with self-assembly to promote order-order martensitic reconfiguration of bulk colloidal crystals made from both spherical[11] and dumb-bell shaped colloids[12]. Here, we show that application of AC electric fields to ordered self-assembled chains leads to reconfiguration of the ellipsoids through a sliding mechanism. This transformation is reversed on removal of the

AC electric field leading to the generation of shape-memory colloidal self-assemblies with an amplitude of motion that is comparable to muscle tissue.

## 5.2. Materials and Methods

### 5.2.1 Janus Ellipsoid Synthesis:

Janus ellipsoids were synthesized using methods described in Shah et al.[15] Here, we synthesize carboxylate stabilized ellipsoids (F-8820, Invitrogen Inc) as well as sulfate stabilized ellipsoids (F-8851, Invitrogen Inc) using the same procedure. Briefly, 300 μL of a 2-wt% PS spherical particle solution is homogenized with 7.5 mL of a 10-wt% aqueous PVA solution. This solution is poured into Omni trays. The solution is allowed to dry overnight to form uniform ~ 40 μm thick films. This film is then cut into strips and placed in a custom made uniaxial mechanical stretching device built in an oven. The strips are first heated above the glass transition temperature of PS (~120°C) and then uniaxially stretched using the stretching device. The aspect ratio of the ellipsoidal particle can be controlled by the strain applied on the PVA strips (c.f. SI). The strips are then allowed to cool at room temperature and dissolved in water. This releases ellipsoidal particles that are centrifuged at 5000g and redispersed in ultrapure deionized (DI) water (Life Technologies) at least 5 times. This removes impurities and PVA from the particle solution.

Next, we use spin coating to create a monolayer of the ellipsoidal particles. A microscope glass slide (Fisher Scientific) is first placed in a base bath (30-40 g potassium hydroxide pellets (Sigma Aldrich) dissolved in 100mL water and 400mL isopropanol (Sigma Aldrich)) for ~ 30 minutes. The glass slide is then thoroughly rinsed with water. The uniform ellipsoids synthesized

earlier are also redispersed in 300 μL of ethanol. This solution is then spin coated onto the treated microscope glass slide to create a uniform monolayer of ellipsoidal particles.

Finally, the glass slide with the monolayer of ellipsoidal particles is placed in an e-beam evaporator. Vertical deposition of 7.5 nm chrome and 15 nm gold onto the glass slide leads to preferential deposition of chrome and gold on one half of the ellipsoids to create Janus ellipsoidal particles. These Janus ellipsoidal particles are then swept off the substrate and dispersed in water. These particles are then centrifuged (1000g) and redispersed in ultrapure DI water at least 5 times to remove impurities from the solution. Finally, the particles are dispersed in ~ 2.5 mL of ultrapure DI water to create a stock solution.

### 5.2.2 Self-Assembly of Janus Ellipsoids:

A 2.5 mL stock solution of the Janus ellipsoid particles is created using methods described in the earlier section. The particles in the stock solution are dispersed using a horn sonicator (Cole-Palmer Instruments) for 30 seconds. A variety of sodium chloride salt concentrations are created in ultrapure DI water (1 mM to 10 mM). 300 μL of the stock solution is then centrifuged and the supernatant is replaced by 300 μL of the required salt concentration. Janus ellipsoids in the salt solution are sonicated using the horn sonicator for 30 seconds and placed in one of the wells of an 8-well Lab-Tek II chambered #1.5 German coverglass system (Nunc). This holder was previously treated in the base bath for at least two hours, and thoroughly rinsed with water before addition of the Janus ellipsoid solution. The particles are then allowed to sediment and self-assemble for 20 hours before imaging with a confocal laser-scanning microscope (CLSM, Nikon A1r).

### 5.2.3 AC field assembly of Janus ellipsoids:

AC field assembly of Janus ellipsoids is performed in a device with coplanar electrodes for easy visualization with a CLSM (Velev et al). Coplanar electrodes are created by depositing 7.5 nm chrome and 15 nm gold on a coverslip (35 x 50 cm, Fisher Scientific) that has a 1mm thick (50 cm long) masking tape placed in the center of the slide. After deposition of the metal, the masking tape is removed to create a 1 mm gap between the two coplanar electrodes. This coverslip with the coplanar electrodes is then placed in the base bath for ~ 1 hour before use. After thoroughly rinsing the coverslip with water, a chamber is constructed to hold the colloidal suspension (c.f. SI). T2 thermocouple wires (0.5 mm diameter, Goodfellow Inc) are glued to each of the coplanar electrodes using silver epoxy (MG Chemicals). The colloidal suspension is then allowed to sediment and self-assemble for ~ 20 hours. The wires are subsequently connected to an AC field generator (Rigol DG 1022). The AC field generator is used to apply a 10 $V_{rms}$ square waveform at different frequencies across the colloidal suspension.

### 5.2.4 Chamber for AC electric field device

Glass spacers are first created by drilling a 0.5 cm hole in a microscope glass slide and cutting into 2 cm by 2 cm squares. The glass spacer is stuck to the coplanar electrode coverslip using an imaging spacer (Grace Bio-Labs imaging spacers, GBL654002). We also drill 35 x 50 mm coverslips with a 1 mm hole. This slide is attached to the glass spacer using another imaging spacer. We ensure that the hole in the cover slip is positioned above the hole in the glass spacer. This leads to the creation of a chamber with an inlet for the colloidal suspension. The colloidal suspension is subsequently pipetted into the chamber and used for experiments.

### 5.2.5 Synthesis of ellipsoids with varying aspect ratios

Ellipsoids are synthesized using methods described in the main text. The aspect ratio of the colloidal particles is controlled by the strain applied during the uniaxial extension of the PVA strips. We synthesize aspect ratio 2.1 ± 0.2, 3.2 ± 0.2, 5.0 ± 0.4 and 6.8 ± 0.9 ellipsoids on application of strains of 0.45, 0.9, 1.4 and 4.2 respectively to the PVA strips using the uniaxial stretching device.

## 5.3. Results and Discussions

Figure 5-1 reports the equilibrium assembly of Janus ellipsoids (Aspect ratio (r) (major axis length (2a) / minor axis diameter (D)) of the particles is 5.0 ± 0.4). The inset of Figure 5-1a shows the scanning electron microscopy image of one such Janus ellipsoid particle. Figure 5-1a reports the OrF equilibrium phase of sulfate-stabilized Janus ellipsoids, observed after 20 hours of self-assembly in a 5mM sodium chloride (NaCl) aqueous solution. The particles were synthesized by the sequential deposition of 7.5 nm of chrome and 15 nm of gold on a monolayer of ellipsoidal particles (c.f. Methods).[6] Two-channel reflection and fluorescence confocal laser-scanning microscopy (CLSM) was used to identify each half of the Janus particle in the assembled phases.[6] In Figure 5-1b-e, we show a close-up image of one self-assembled chain. Figure 5-1b shows the fluorescence channel (red) that identifies the uncoated polymer half of the particle, while Figure 5-1c shows the reflection channel (green) that identifies the metallic half of the particle. The composite image (Figure 5-1d) as well as its rendering (Figure 5-1e) shows that the gold faces are preferentially bonded, while the particles are aligned and offset due to the

Janus functionality and ellipsoidal shape of the particle. We further discuss the positional and orientational symmetry of these chains in Figure 5-2.

Figure 5-1 also shows that the structure of the self-assembled phase is a sensitive function of the pair interactions between the Janus ellipsoids. In pure deionized (DI) water, the Debye layer thickness and thus electrostatic repulsion is sufficiently large that Janus ellipsoids are free particles due to minimal gold-gold binding (free particle (FP) phase, Figure 5-1f). The inset images of Figure 5-1f show the fluorescence, reflection and composite channel for one such particle. At low salt concentrations (1mM), there is sufficient reduction in electrostatic repulsion that gold-gold binding leads to the assembly of Janus ellipsoid clusters (close packed cluster (ClC) phase, Figure 5-1g). Janus ellipsoid clusters are predominantly trimers or tetramers for this specific aspect ratio (r = 5.0). The inset image shows the fluorescence, reflection, and composite channel for one such tetramer. At intermediate salt concentrations (2-5 mM), electrostatic repulsion is further reduced, leading to an increased propensity for gold-gold binding. Resultant assemblies are chains that are positionally and orientationally ordered (OrF phase) as described earlier in Figure 5-1a-e. At even higher salt concentrations (10mM), assembled chains have neither positional nor orientational order (disordered chain (DC) phase) because the high gold-gold attractive force does not permit reorientation of Janus ellipsoid particles on bonding. The inset images show a close-up view of the fluorescence, reflection and composite channel of one such chain.

In Figure 5-1i, we plot the dimensionless chain length ($l$) (length of chain (μm) / major axis length of Janus ellipsoid (μm)) as a function of the salt concentration for r = 5.0 Janus ellipsoids and observe that the longest chains ($l \sim 9$) are assembled at a salt concentration of 5mM (as in Figure 5-1a-e). The standard deviations for $l$ are large because the chain lengths are

not uniform; this non-uniformity suggests a stochastic mechanism of chain formation, which we address later. We note that although some branching and defects in the chain assemblies occur, the growth of the OrF phase is clearly one-dimensional; growth perpendicular to the chain direction is suppressed. The OrF phase is unique to Janus ellipsoids and we focus on understanding this phase and exploiting its properties in this letter.

Figure 5-1 (main text) reports the self-assembly of sulfate-stabilized Janus ellipsoids (aspect ratio) at different salt concentrations. We demonstrate the assembly of similar structures from particles with different surface stabilizing groups. Here, we demonstrate the assembly of carboxylate-stabilized Janus ellipsoid particles (Figure 5-2). Carboxylate-stabilized Janus ellipsoids are synthesized from 1.1 μm diameter spherical particles (F-8820, Invitrogen Inc) using methods described in the main text. These particles are then self-assembled at different salt concentrations and results are depicted in Figure 5-2. The free particles (FP) phase is observed at 0 mM salt. Addition of 1 mM salt leads to formation of a cluster phase (ClC). Ordered fiber (OrF) phases are observed at 2 mM and 2.5 mM. Disordered chain (DC) phases are observed at higher salt concentrations (3 mM and 5 mM). We note that these phases are similar to the ones observed for sulfate-stabilized Janus ellipsoid particles. However, ordered chains are formed at lower salt concentrations as compared to the sulfate-stabilized particles. The transition between the OrF and DC phase also occurs at lower salt concentrations. We attribute this change to the variation in surface charge of the sulfate-stabilized and carboxylate-stabilized particles. We however note that the assembly structures are similar to those observed for the sulfate-stabilized Janus ellipsoidal particles.

Figure 5-3a-c reports the OrF phase for aspect ratio (r) = 4.1, 5.0 and 6.8 respectively. As is evident in the inset images, while the lattice constants of the ordered chains are dependent on

the dimensions of the particle, the OrF symmetry of the unit cell repeated along the chain is consistent across different aspect ratios. Figure 5-3d reports a phase diagram of the experimentally assembled phases observed at different aspect ratios. FP, ClC, DC and OrF phases (shown for r = 5.0 particles in Figure 5-1) are observed for a variety of different aspect ratios and salt concentrations. We note that the OrF phase is observed at different salt concentrations, but only for r > 3.5. Thus, this phase seems to require shape anisotropy in addition to Janus functionality, an observation we next investigate through simulations. Approximating the transition of specific phases as the midpoints between two experimentally observed unique phases makes the phase diagram. Voronoi tessellation is also used to create a phase diagram from the experimentally observed data points (data not shown). There is no major difference between the two methods of phase diagram construction and further refinement in the accuracy of the phase diagram is only possible through additional experiments

We conducted molecular dynamics (MD) simulations for r = 5.0 using HOOMD-Blue, a GPU accelerated MD code.13,14 Figure 5-3e shows our model particle – ten overlapping beads packed inside an ellipsoidal shell. These beads interact via three potentials: a shifted Weeks-Chandler-Andersen (WCA) potential to account for volume exclusion, an angularly modulated, shifted Lennard-Jones potential to model the van der Waals attraction between gold patches, and a Yukawa potential to model the screened electrostatic repulsion between particles due to surface charges (c.f. Supplementary Information (SI)). Our simulations reproduce all observed phases for Janus ellipsoids by varying the Debye layer thickness ($k^{-1}$) (equivalent to varying salt concentrations in experiments) (c.f. SI). Figure 5-3f shows a snapshot of a 1000-ellipsoid simulation assembling into the OrF phase. A chain extracted from this simulation is shown. Its detailed structure matches the ordering observed in the experiments, as shown in Fig 5-3a-c.

The OrF phase consists of chains that are composed of four strands of aligned particles, touching end-to-end. The strands lie on the vertices of a rhomb (Figure 5-3f), with ellipsoids in adjacent strands shifted by about one half-particle length, and rotated 90 degrees about the chain axis. One pair of strands is in contact with three other strands, while the other pair is in contact with two other strands. We note the strands can slide along each other with just a small energy penalty; thus the amount of shift between adjacent chains can fluctuate significantly. This energy landscape is the origin of the capacity for reconfiguration. It contrasts with the assembly of cylindrical rods: Vacha and Frenkel predicted ribbon-like assembly structures for patchy cylinders where particles assembled into chains that grew perpendicular to the major axis.[5] Our ellipsoid system differs in two respects – the potential favors alignment of the particles to maximize gold-gold interactions, rather than just contact, and the tapered ends of the ellipsoids allow maximal contact area when the particles are in chains rather than ribbons.

While the OrF motif is predominant, Figure 5-3g shows the two most common types of defects, observed in both simulations and experiment. On the left, an extra particle is inserted into the four-particle motif while on the right, a particle is missing from the four-particle motif. Figures 5-3h(i-iv) report the growth mechanism of an ordered fiber. First, the particles form clusters containing between three and five particles (Figure 5-3h(i)). These clusters diffuse and coalesce into larger clusters (Figure 5-3h(ii)). Clusters of more than five particles are elongated, but do not possess the same four-particle motif observed in the OrF structure due to end effects. End effects lead to a break in the OrF symmetry because enough particles are not present, thus leading to formation of trimers at the ends of chains. These elongated clusters continue to diffuse, and coalesce with other clusters when their ends, which have the most exposed gold patch, come in contact (Figure 5-3h(iii)). Once the chains have reached a dimensionless chain

length ($l$) greater than 4 (~ 16 Janus ellipsoids in a chain), the particles rearrange into the OrF structure (Figure 5-3h(iv)). We attribute this ability to rearrange to the low potential energy changes for sliding along the gold patches of neighboring ellipsoids (< 3 $k_BT$) relative to binding strengths in the OrF structure (~ 30 $k_BT$) (cf. SI). A movie of the chain growth depicted in Figure 5-3h is available in the SI (Supplementary Movie (SM) 1). Our simulations thus describe the growth mechanism of the OrF structure and shows that the symmetry of this structure is a result of the particle geometry and torsional potential.

Application of AC electric fields reconfigures the equilibrium assembly phases of the Janus ellipsoids, as reported in Figure 5-4. Figure 5-4a shows a schematic of the coplanar AC electric field device used for these experiments (c.f. Methods). A constant root mean square (RMS) voltage of 10 V and frequencies ranging from 1 kHz to 10 MHz were applied across the 1 mm gap and the resulting structures are visualized by CLSM. Figure 5-4b reports the phase diagram of the assembly phases observed for Janus ellipsoids at different salt concentrations and varying frequencies. At low frequencies, the main effect of the AC electric field is to align the self-assembled Janus ellipsoid phases (c.f. phase diagram, Figure 5-3) in the direction of the electric field lines. Thus, as a function of salt concentration we observe aligned free particle (AFP), aligned close packed cluster (AClC) and aligned ordered fiber (AOrF) phases (c.f. SI). At higher frequencies, however, new ordered phases are observed. The attractive force of the induced dipole caused, on application of AC electric fields at higher frequencies, the AFP and AClC phases to combine into a staggered chain (SC) phase. This ordered phase, observed previously for Janus spheres, is shown in Figure 5-4d and, in close up, in Figure 5-4e. After image processing, the coordinates of the chains are rendered as in Figure 5-4f. Janus ellipsoids are bonded by their tips on the gold half of the particle to two other particles and the ball and

stick diagram shows the various bonds between the Janus ellipsoid particles in the SC configuration (Figure 5-4g). At salt concentrations at which the OrF phase arises, application of an AC electric field leads to generation of a new chain-link (CL) phase that resembles the symmetry of common bicycle chains (Figure 5-4h). A close up view of the assembled chain along with a ball and stick diagram that depicts particle-particle contact bonds is shown in Figure 5-4i (3D rendering, Figure 5-4j). The symmetry of the repeated unit cell of the CL phase is a four-particle motif of two pairs of ellipsoids, with each pair oriented 180° relative to each other. Each pair is connected at the tip to an adjacent pair oriented 90° relative to it. Thus, each Janus ellipsoid in this assembly has four contact bonds with adjacent Janus ellipsoid particles. This phase, a reconfiguration of the equilibrium OrF phase, has no analog in the case of Janus spheres.

The existence of SC is expected for Janus particles.[10] In the appropriate frequency ranges, the electric dipole moment of the Janus ellipsoid moves away from the ellipsoid center of mass toward the extremities of the Janus gold half of the particle (c.f. Figure 5-4c). These dipoles chains create a staggered chain to minimize electrostatic energy. Simulations show that the SC structure is observed for particles that interact with a pair potential that forms clusters at equilibrium when an additional field-induced dipole is added at the ends of the gold half of the particle. This result is consistent with experimental observations (c.f. Figure 5-4d)

On the other hand, the origin of the CL structure is an emergent, unexpected outcome of the application of AC electric fields to Janus ellipsoids self-assembled into OrF chains. This outcome is unexpected because adjacent, parallel pairs of particles (as observed in the OrF and CL phase) should be suppressed in favor of SC structures. In the OrF phase, the dipoles on particles are close to each other and this is energetically very unfavorable.

Several collective mechanisms may be responsible for the elongation of the OrF chains into the CL structure upon the application of an AC electric field. We note that there exists a conducting channel through the center of the chains in the self-assembled OrF phase as all the gold patches are in contact. Thus, application of an AC electric field will cause charge to build-up at the chain-ends. This accumulation of charge will result in a net force on the chain ends towards the electrodes, pulling on either end of the chain. A second force driving the elongation of these chains results from the magnetic field induced by the intra-chain current. As the field switches direction, current flows along the conducting channel in the middle of the ellipsoids, resulting in an axial compression force. These extensional forces are counterbalanced by compressive self-assembly forces that seek to maximize contact between Janus ellipsoid particles. In simulations, we have reproduced the transition from OrF to CL by introducing either a constant force on the chain ends (to simulate a dielectrophoretic force), or by introducing an axial compression force (to simulate the magnetic compression).

The OrF phase can be rapidly and reversibly reconfigured into the CL phase upon the application of an external AC field. Figure 5-5 reports the short-time actuation of one-dimensional assemblies by switching between the self-assembled OrF phase and directed assembly CL phase upon application of AC electric fields (10 $V_{rms}$, 1 MHz). Figure 5-5a reports a close-up view of carboxylate-stabilized Janus ellipsoids self-assembled into an OrF phase chain (2 mM NaCl in DI water, c.f. SI). The AC electric field rapidly reconfigures the OrF phase chain into the CL phase (Figure 5-5b). This reconfiguration elongates the chain due to the difference in lattice parameter between the OrF and the CL phase. Elongation of the chain length is maintained as long as the AC electric field is applied, as shown in Figure 5-5c. Removal of the AC electric field leads to reconfiguration of the chains from the CL phase to the OrF phase, and

a concomitant reduction in the length of the assembly (Figure 5-5d). This structure is now identical to the initial, equilibrium assembly shown in Figure 5-5a (self-assembled OrF phase). This elongation in assembly chain length is quantified as a function of time by image-processing CLSM images taken at a rate of 30 frames per second (fps, Figure 5-5e, S.M-2). The reconfiguration in chain length is rapid: full extension of the chain occurs in 1.5 seconds, while relaxation of the chain occurs in 3.5 seconds. This process can be reversibly repeated multiple times on switching the AC electric field as noted in Figure 5-5f. The extension in chain length is measured to be 36 ± 7% and we note that this extensional strain is independent of the initial chain length as shown in Figure 5-5g (based on analysis of 30 chains, c.f. SM-3). The assembly goes out of frame for certain time periods and hence Figure 5-5e,f do not data points at all time intervals. We add a dotted line to the graph to show the approximate chain length for those time intervals.

The amount of extension and contraction induced by the reconfiguration is consistent with the self-assembled and emergent structures. In the OrF phase, the unit cell has a rhombic cross-section comprising of four Janus ellipsoids, only two of which are in contact (c.f. Figure 5-5 h,i). The two ellipsoids not in contact slide till they come into contact with each other due to both magnetic compression and electrostatic extension (Figure 5-5i). This leads to an extension of the chain into the CL phase (Figure 5-5j). These geometric considerations yield a net predicted strain of 41.4% in the unit cell (Figure 5-5j). Accounting for the finite size of the chains and the average length of the chains in our experimental measurements, we predict the strain to be 33.1% from geometric considerations, (c.f. Figure 5-5j) which is within the error bars of the strain amplitude measured for the shape-memory OrF to CL transition.

Traditionally, external fields have been used to accelerate self-assembly,[15] but rarely to create defect-free, higher quality assemblies.[16] Over long-time scales, the unique, emergent response of the OrF phase on micro-actuation by the AC electric field permits the formation of longer, more uniform chains as reported in Figure 5-6. Figure 5-6a shows the initial equilibrium phase of carboxylate-stabilized Janus ellipsoids (assembled at 2.5 mM salt). Application of a 10 $V_{rms}$ 2 MHz AC square wave electric field leads to reconfiguration of the OrF phase to the CL phase (c.f. Figure 5-4). The chain ends of assembled chains in the CL phase are attractive due to dipoles induced by the AC electric fields. A close-up view (Figure 5-6b,c and S.M-3) shows that smaller chains not only combine to form larger chains (as depicted by arrows in Figure 5-6c), but also align in the direction of the AC electric field. Subsequent removal of the AC electric field leads to reconfiguration of the CL phase chains back to self-assembled OrF phase chains, while maintaining the length of the chains achieved through application of the AC electric field. This is evident in the dramatic increase in chain length of the self-assembled chains immediately after application of the AC electric field for 30 minutes (Figure 5-6d). We note that the chains are not only longer but also more uniformly ordered, consistent with results of simulations (Figure 5-3), which show that long self-assembled Janus ellipsoid chains promote internal particle motion that leads to increased uniformity in self-assembled chains. Thus, the application of AC electric fields promotes 'annealing' of chains and improves the uniformity of chains. Over time, we note that Brownian fluctuations cause the chains to lose orientational alignment along the AC field direction and evolve toward an equilibrium chain length. However, there is a net increase (Figure 5-6e) of a factor of 2.5 in the dimensionless chain length (Figure 5-6f) at 24 hours after removal of the AC electric field relative to the original self-assembly. This increase in length occurs because at higher salt concentrations, the chain length becomes kinetically trapped during self-

assembly. Application of AC electric fields permits the assembled chains to escape this kinetic trap and arrive at the equilibrium chain length, just as in the anneal of other materials with slow kinetics, such as block copolymer self-assemblies.

This net increase in chain length is however not observed for Janus ellipsoids assembled at 2mM salt concentration (Figure 6f) because at this lower salt concentration, chains were not kinetically trapped during self-assembly and hence the equilibrium chain lengths obtained after application of the AC electric field are similar to self-assembled chain length distribution. Thus, the AC electric fields, applied in the long term, modify the kinetic pathways for assembly and can therefore be used as a tool to control the length of the shape-memory colloidal assemblies

**5.4. Conclusions**

The self-assembly of one-dimensional, ordered and self-limiting colloidal chains from Janus ellipsoid patchy particles that can be reconfigured rapidly on application of AC electric fields results in the formation of functional shape-memory colloidal assemblies. These shape-memory colloidal chains can be micro-actuated to control assembly chain-length. Micro-actuation of the assembly chains can also be used to make the self-assembled chains longer and more uniform.

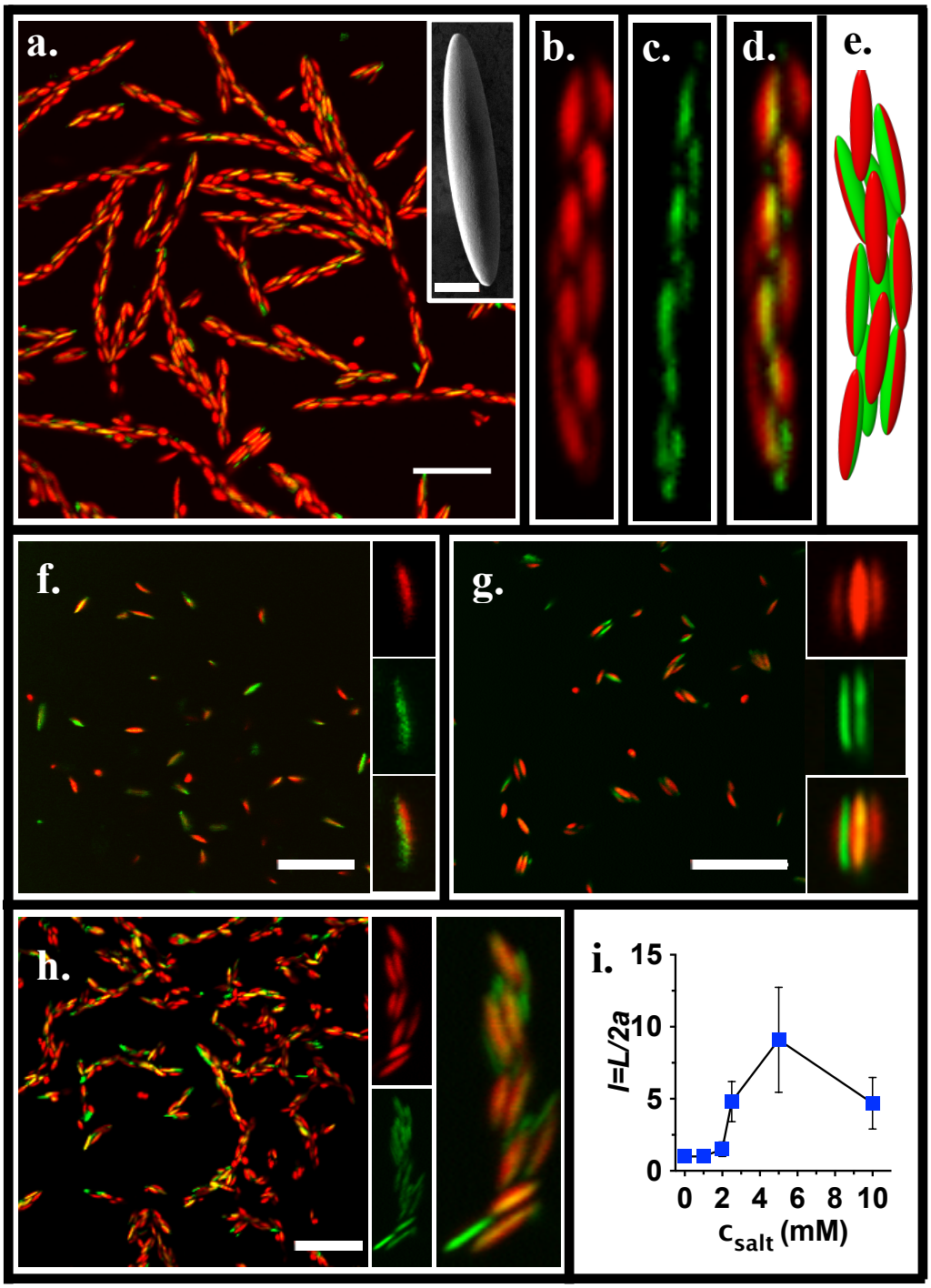


**Figure 5-1:** a. CLSM image of Janus ellipsoids (aspect ratio = 5) suspended in 5 mM NaCl in DI water. Scale bar: 10 μm. Inset scanning electron microscopy (SEM) of a Janus ellipsoid. Scale bar: 0.5 μm. b. Close-up of the fluorescence-imaging channel for one assembled Janus ellipsoid chain. c. Close-up of the reflection-imaging channel for one assembled Janus ellipsoid chain. d.

Composite channel that combines both the fluorescence and reflection channels. Red- Uncoated fluorescent polymer half of the particle. Green- Gold and chrome coated part of the particle. e. Computer generated rendering of Janus ellipsoid assembled chain. f. CLSM image of Janus ellipsoids (aspect ratio = 5) suspended in DI water without salt. Scale bar: 10 μm. Inset shows the fluorescence, reflection and composite channels of one such Janus ellipsoid. g. CLSM image of Janus ellipsoids (aspect ratio = 5) suspended in 1 mM NaCl salt in DI water. Scale bar: 10 μm. Inset shows the fluorescence, reflection and composite channels of one Janus ellipsoid cluster. h. CLSM image of Janus ellipsoids (aspect ratio = 5) suspended in 10 mM NaCl salt in DI water. Scale bar: 10 μm. Inset shows the fluorescence, reflection and composite channels of one such disordered chain. i. The dimensionless chain length ($l$) as a function of salt concentration ($c_{salt}$) is reported for Janus ellipsoids (aspect ratio = 5).

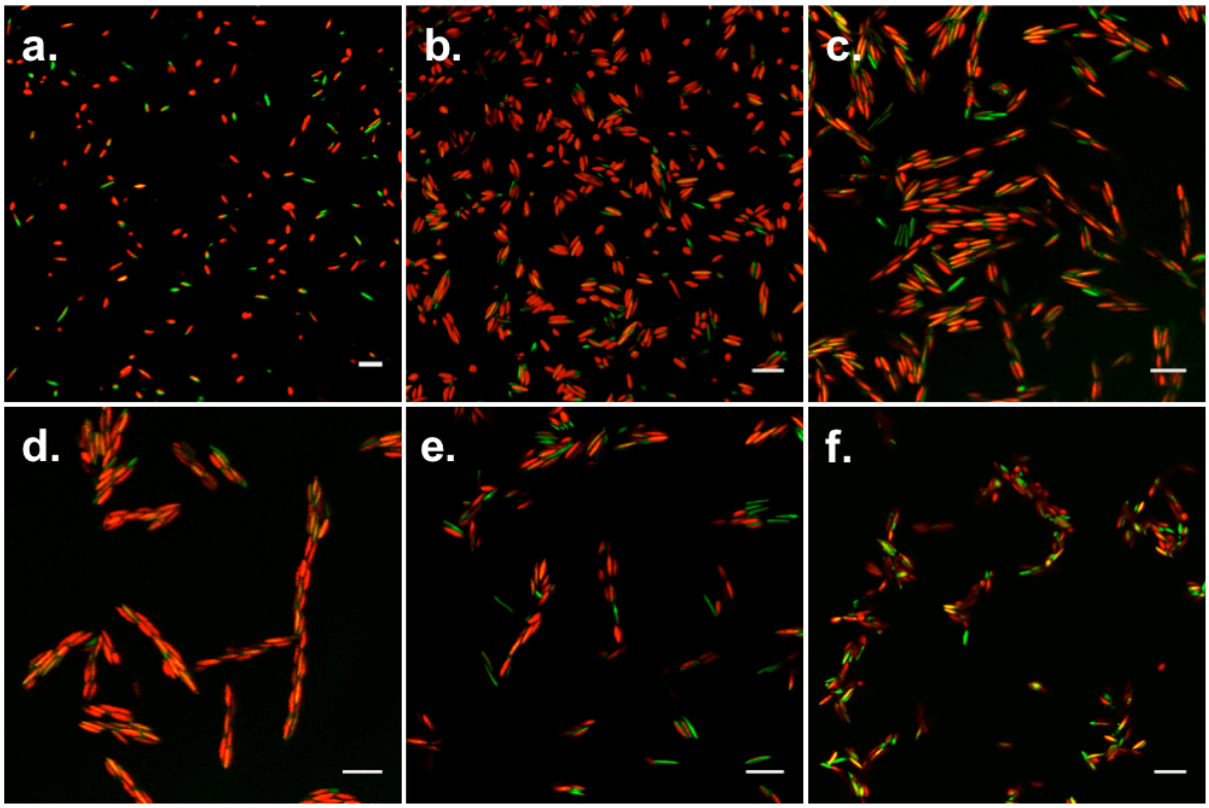


**Figure 5-2:** Assembly of carboxylate stabilized Janus elliposids as a function of sodium chloride (NaCl) salt concentration. a. 0 mM salt. b. 1 mM salt c. 2 mM salt. d. 2.5 mM salt. d. 3 mM salt. e. 5 mM salt. f. 10 mM salt

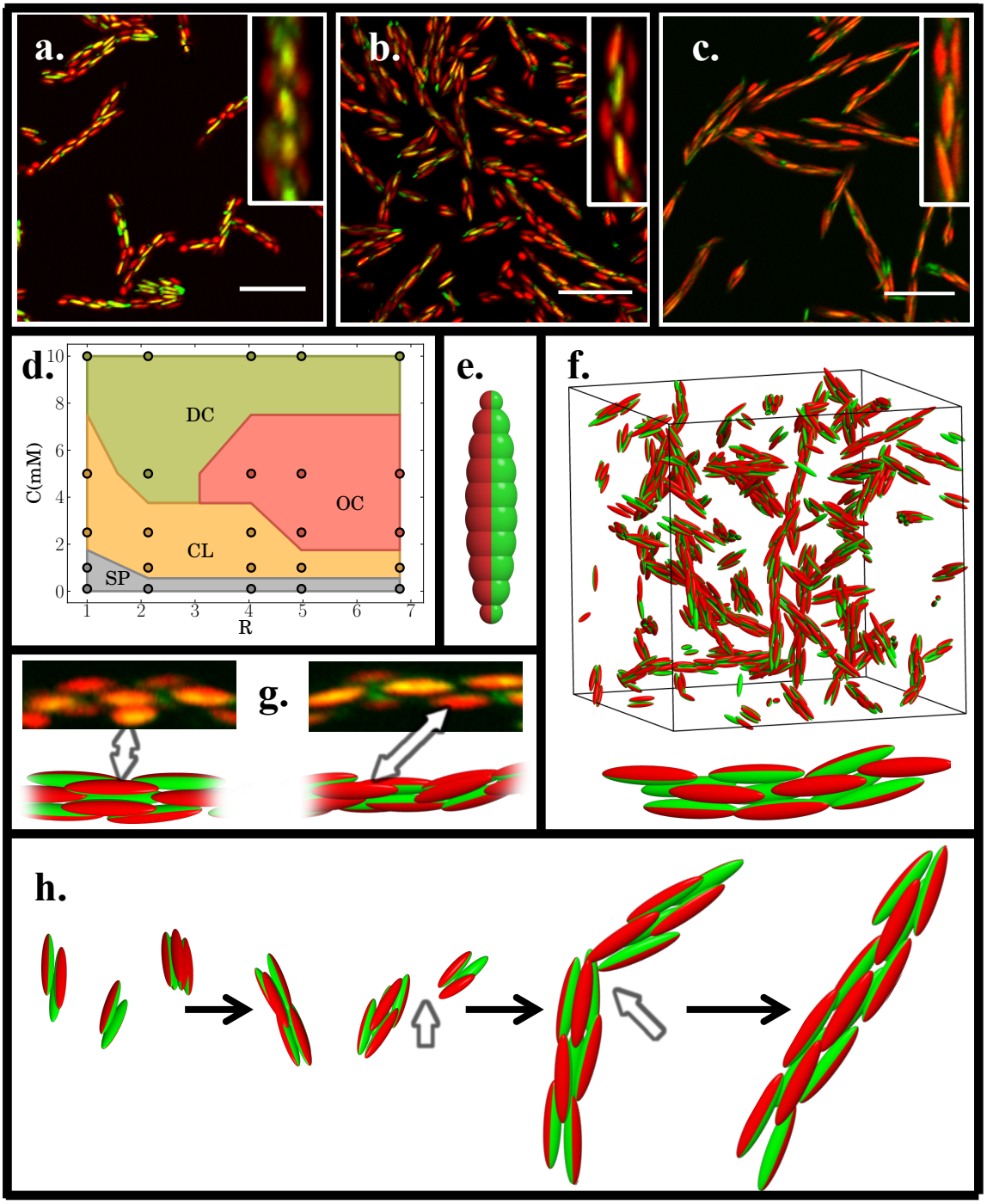


**Figure 5-3:** a., b., c. CLSM image of a close-packed chain link (CpCl) ordered phase for aspect ratio 4.1, 5.0 and 6.8 Janus ellipsoids respectively. Scale bar: 10 μm. Inset image reports the

close-up view of one such chain. d. Phase diagram of assembled phases of Janus ellipsoids as a function of their aspect ratio and salt concentrations. DC (Disordered chain phase), ClC(close packed cluster phases), FP (free particle) and OrF(ordered fiber phase) e. Representation of a Janus ellipsoid created by merging 10 spheres for simulation studies. The energy isosurfaces are smoother than this representation due to soft potentials (cf. SI Figure 3). f. Simulation study of the assembly of 1000 ellipsoids into the OrF ordered phase. Close-up view of one of the ordered chains is also shown. g. Two primary defect types, including the addition of an extra particle and the displacement of a particle from the unit cell are observed in experiments (CLSM images) and simulations (renderings). h. Kinetics of chain formation by the combination of clusters is depicted through simulation snapshots.

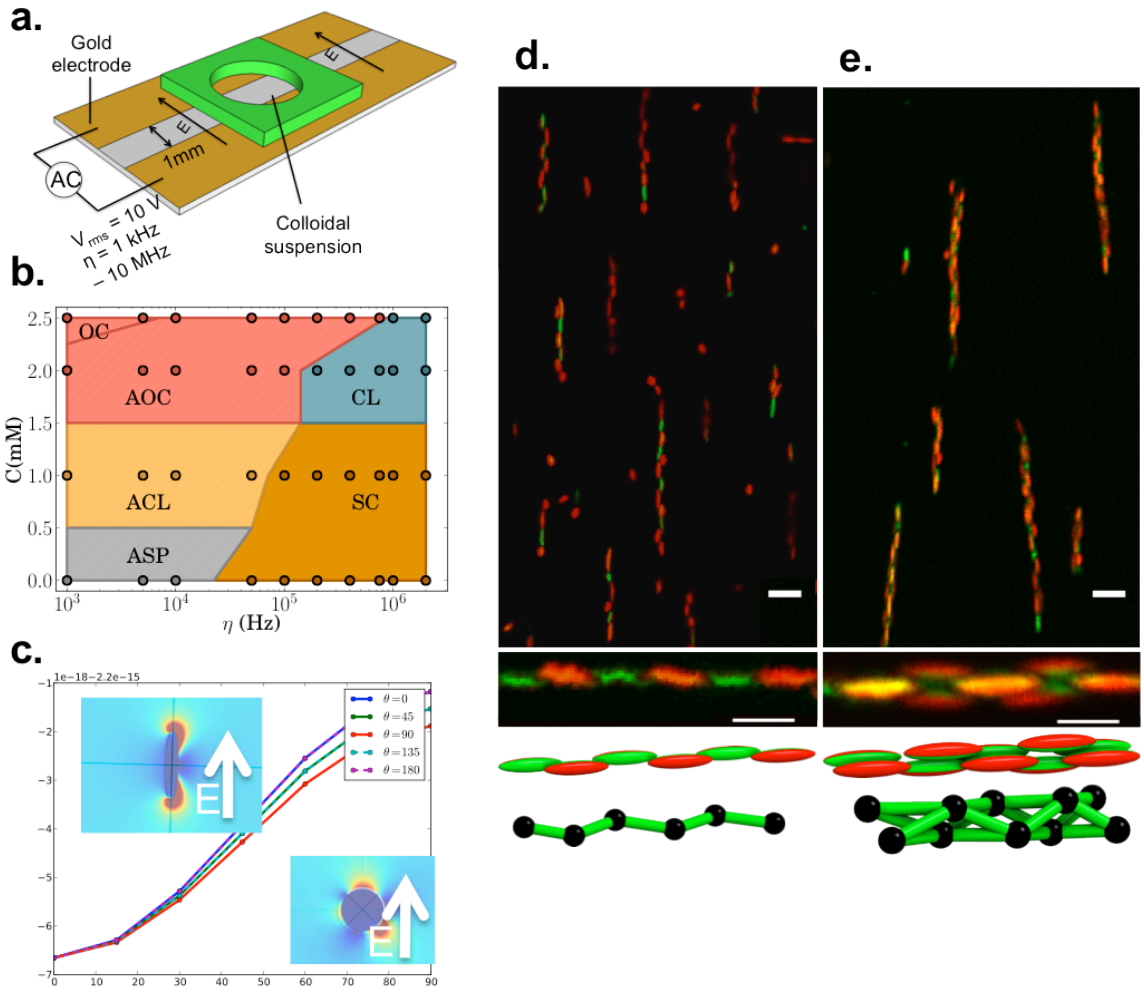


**Figure 5-4:** a. Schematic of AC electric field device. b. Phase diagram of assembly phases of Janus ellipsoids upon application of 10 $V_{rms}$ AC electric field as a function of salt concentration and frequency. c. COMSOL simulations of single particle Janus ellipsoids d. Zoomed-out CLSM image of staggered chain (SC) assembly structure. Scale bar: 5 μm. A close-up view of one of the chains (Scale bar: 3 μm) along with the corresponding rendering and the ball-stick bond diagram are also shown. e. Zoomed-out CLSM image of stretched chain-link (SCl) assembly structure. Scale bar: 5 μm. A close-up view of one of the chains (Scale bar: 3 μm) along with the corresponding rendering and the ball-stick bond diagram are also shown.

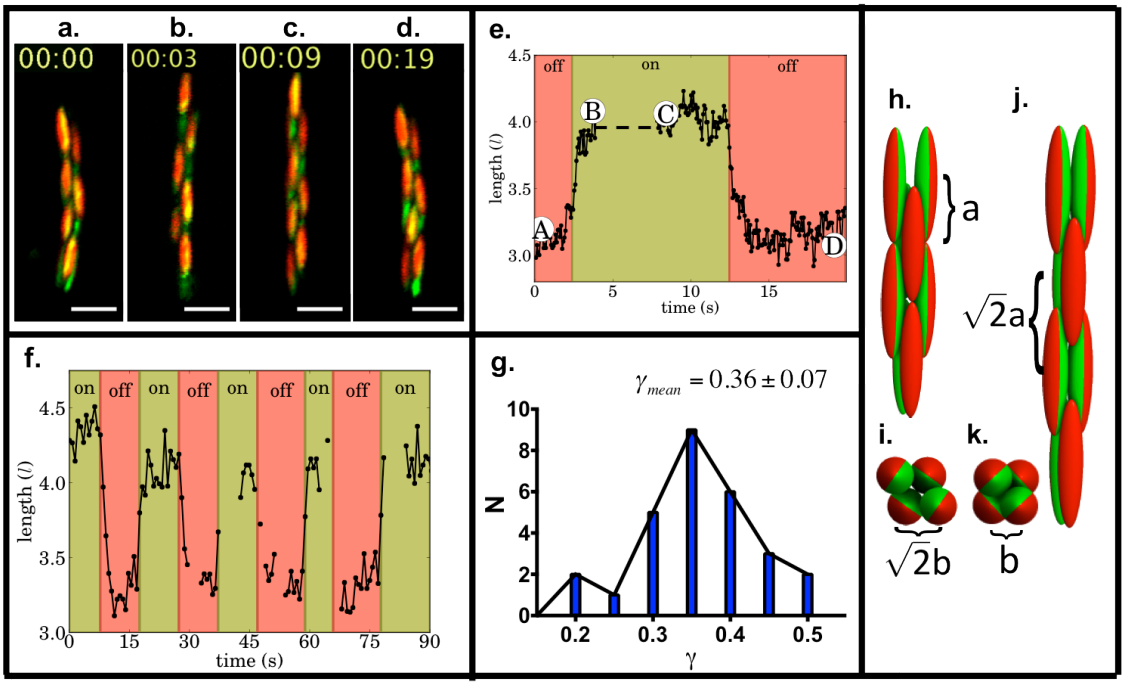


**Figure 5-5:** Close-up view of Janus ellipsoid chain a. Before application of AC electric field. (Scale Bar: 3 μm). b.,c. During application of AC electric field. (10 $V_{rms}$, 1 MHz) d. After application of AC electric field. e. Dimensionless chain length ($l$) as a function of time on application of AC electric fields. f. Dimensionless chain length ($l$) as a function of time on switching the AC electric field on – off. g. Distribution of the strain in the chain length on application of AC electric fields for a number of chains with varied lengths. h.-i. Rendering of the OrF structure and its rhombic cross section. j.-k. Rendering of the CL structure and its square cross section, showing the maximal strain possible under geometric constraints.

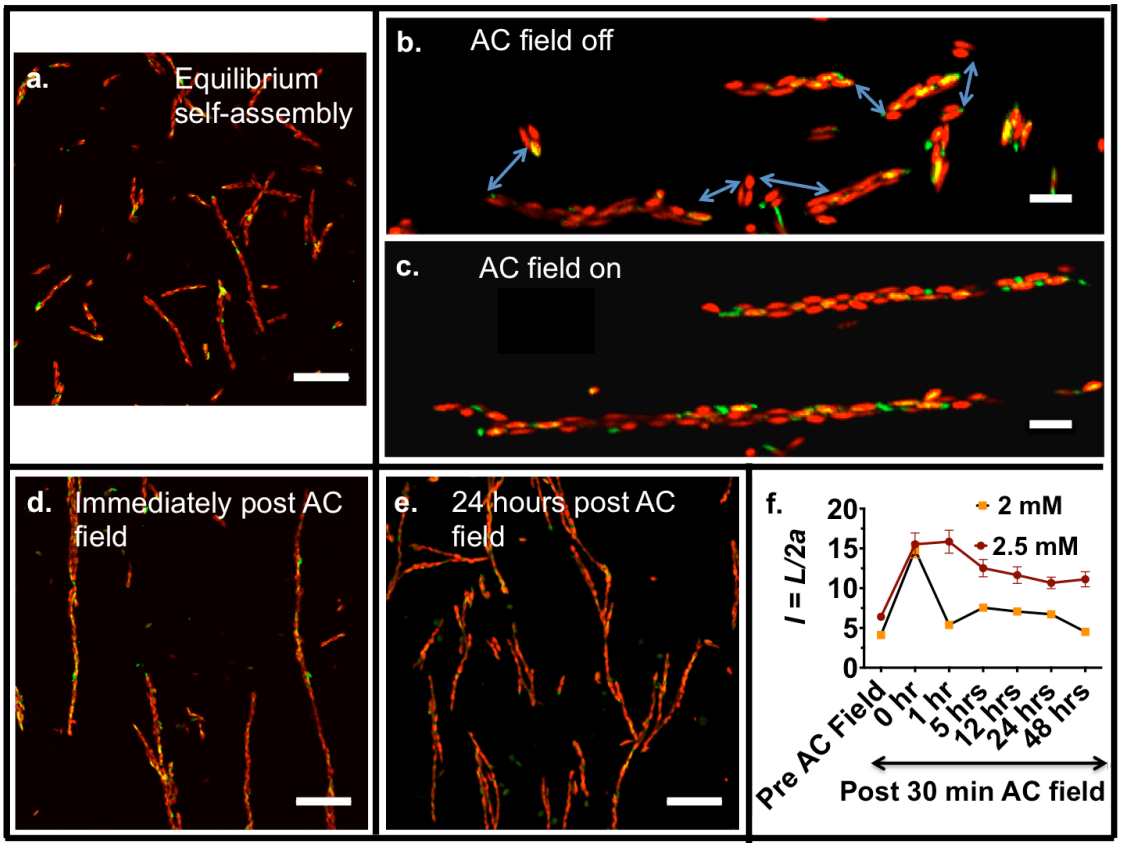


**Figure 5-6:** a. CLSM image of aspect ratio five Janus ellipsoids suspended in 2.5 mM NaCl in DI water. Scale bar: 20 µm. b., c. Close-up view of Janus ellipsoid assembly before and during application of AC electric fields respectively. d. CLSM image immediately after application of AC electric fields for 30 mins. e. CLSM image 24 hours after application of AC electric fields. f. Dimensionless chain length of Janus ellipsoid assemblies at 2 mM and 2.5 mM salt concentrations as a function of time.

## 5.5. References


1. Zhang, Z. & Glotzer, S. C. Self-assembly of patchy particles. *Nano Letters* **4**, 1407-1413 (2004).

2. Glotzer, S. C. & Solomon, M. J. Anisotropy of building blocks and their assembly into complex structures. *Nature Materials* **6**, 557-562 (2007).

3. Mao, X.; Chen, Q. & Granick, S. Entropy favours open colloidal lattices. *Nature materials* (2013).

4. Mitragotri, S. & Lahann, J. Physical approaches to biomaterial design. *Nature Materials* **8**, 15-23 (2009).

5. Vacha, R. & Frenkel, D. Relation between molecular shape and the morphology of self-assembling aggregates: a simulation study. *Biophysical journal* **101**, 1432-1439 (2011).

6. Shah, A. A.; Schultz, B.; Kohlstedt, K. L.; Glotzer, S. C. & Solomon, M. J. Synthesis, assembly, and image analysis of spheroidal patchy particles. *Langmuir* **29**, 4688-4696 (2013).

7. Liu, Y.; Li, W.; Perez, T.; Gunton, J. D. & Brett, G. Self Assembly of Janus Ellipsoids. *Langmuir Langmuir* **Langmuir 28**, 3-9 (2011).

8. Chaudhary, K.; Chen, Q.; Juarez, J. J.; Granick, S. & Lewis, J. A. Janus Colloidal Matchsticks. *Journal of the American Chemical Society* **0**, (0).

9. Lumsdon, S. O.; Kaler, E. W. & Velev, O. D. Two-dimensional crystallization of microspheres by a coplanar AC electric field. *Langmuir* **20**, 2108-2116 (2004).

10. Gangwal, S.; Cayre, O. J. & Velev, O. D. Dielectrophoretic assembly of metallodielectric Janus particles in AC electric fields. *Langmuir* **24**, 13312-13320 (2008).

11. Yethiraj, A.; Wouterse, A.; Groh, B. & van, B., Alfons. Nature of an electric-field-induced colloidal martensitic transition. *Physical review letters* **92**, 058301 (2004).

12. DemiroÃàrs, A. F.; Johnson, P. M.; van, K., Carlos M; van, B., Alfons & Imhof, A. Directed self-assembly of colloidal dumbbells with an electric field. *Langmuir* **26**, 14466-14471 (2010).

13. Joshua, A. A.; Chris, D. L. & A., T. General purpose molecular dynamics simulations fully implemented on graphics processing units. *Journal of Computational Physics* **227**, 5342 - 5359 (2008).

14. Trung, D. N.; Carolyn, L. P.; Joshua, A. A. & Sharon, C. G. Rigid body constraints realized in massively-parallel molecular dynamics on graphics processing units. *Computer Physics Communications* **182**, 2307 - 2313 (2011).

15. Shah, A. A.; Kang, H.; Kohlstedt, K. L.; Ahn, K. H.; Glotzer, S. C.; Monroe, C. W. & Solomon, M. J. Liquid Crystal Order in Colloidal Suspensions of Spheroidal Particles by Direct Current Electric Field Assembly. *Small* **8**, 1551–1562 (2012).

16. Vermolen, E. C. M.; Kuijk, A.; Filion, L. C.; Hermes, M.; Thijssen, J. H. J.; Dijkstra, M. & Van, B., A. Fabrication of large binary colloidal crystals with a NaCl structure. *Proceedings of the National Academy of Sciences* **106**, 16063-16067 (2009).

# Chapter 6

# Conclusions and Future Directions

## 6.1 Direct Current (DC) Electric Field Assembly Methods

In Chapter 2, we introduced a new direct current (DC) electric field assembly method to self-assemble colloidal particles into 3D crystalline structures. The method itself was shown to dramatically accelerate the self-assembly process of both colloidal spheres and ellipsoidal particles. The DC electric field assembly device was designed to permit direct visualization of the assembly structures on the confocal laser scanning microscope (CLSM). The images were analyzed using image-processing algorithms and assembly parameters, such as the volume fraction and order parameter, were determined. These assembly parameters were compared to theoretical predictions available for self-assembling systems of the colloidal particles.

In this study, we show that the DC electric field couples to the charge on colloidal particles and drives the particle to the oppositely charged electrode due to the generation of a current. This increase in particle concentration at the particle surface leads to the self-assembly of particles into ordered 3D assembly structures. The current itself was generated due to the reaction of impurities such as water and oxygen present in the solvent at the electrode surface on application of a DC voltage. The current and thus the assembly driving force is a direct function of the impurity concentration in the solvent. The driving force for the colloidal particles is thus lost on reactive consumption of all the impurities present in the solvent. Four our studies, we note that the DC electric field colloidal assembly experiments can be sustained for ~ 3 hours after which a majority of the impurities are consumed. Thus, the DC electric field assembly

method can be used to sustain assemblies for ~ 3 hours. To overcome this time barrier, reducing agents such as potassium ferricyanide were added to the solution. The concentration of these electrochemically active compounds is much higher than that of the impurities present in the solution (100 mM of compound as compared to an estimated 2-3 mM of impurities). Preliminary experiments show that pure DMSO and TBAB are unable to sustain high currents (50 $\mu A/cm^2$) for longer than 1000 seconds (evidenced by the spike in voltage to the DMSO decomposition voltage (c.f. Figure 6-1a). In contrast, DMSO with TBAB and potassium ferricyanide can sustain the same current for an order of magnitude longer time (~ 10000 seconds, Figure 6-1b)) before there is a spike in voltage. The ability to sustain a longer current also implies that the assemblies are maintained for longer time spans. Further, the presence of these electrochemical additives also permits finer control over the colloidal driving force. Thus, the addition of electrochemically active compounds seems to be a promising new direction to further improve both the time period as well as the quality of the colloidal assembly. Further studies are however needed to validate this hypothesis.

In chapter 2, we try to connect the DC electric field assembly method to equilibrium self-assembly in Figure 2-8. However, there is an order of magnitude discrepancy between the experimentally observed and theoretically expected Peclet numbers. We believe this is because the DC electric field assemblies are imaged and analyzed when the system has not achieved steady state. The theory, on the other hand, is for the self-assembly of ellipsoids at steady state. A more accurate comparison of the experiments with theory would include the evolution of volume fraction and thus the osmotic pressure as a function of time. Modelling the DC electric field assembly method as a function of time is thus a subject for furture studies.

In chapter 3, we use the DC electric field device to rapidly assemble colloidal spheres (~ 2 minutes). The ordered assemblies were analyzed using light-scattering, spectrophotometry and CLSM microscopy methods and compared to theoretical predictions for the assembly of colloidal spheres We observe that particles in the size range of 300 – 500 nm have unique reflective color properties and these assemblies could be useful for potential display and camouflage applications.

The DC electric field device has been used to successfully accelerate and qualitatively improve the assembly of colloidal particles, as shown in Chapter 2 and 3. We however note that the colloidal assembly is maintained only as long as the DC electric field is active and supplies a driving force to the colloidal particles. Removal of the DC electric field causes the 3D ordered structures to disassemble into a disordered, fluid phase. In preliminary experiments, we have switched between the disordered and ordered states of the colloidal assembly by switching the electric field. This is used, for example, to switch between the colorless (disassembly) and color (assembly) states of the colloidal sphere assemblies (300-500 nm in size). Reflective color can thus be created reversibly using this assembly method. The quality of the resultant structural color as well as the assembly-disassembly times of the colloidal assembly are directly related to the kinetics of the assembly and disassembly process that are not well understood currently. The efficacy and utility of the DC electric field method to create functional assemblies would be greatly enhanced by theoretical, simulation and experimental studies of the kinetics of the assembly method with assembly variables such as particle size, initial volume fraction and assembly time. This is a significant future study needed for DC electric field assemblies.

Finally, the DC electric field assembly method has proven to be an excellent tool in the self-assembly of complex particles. It can serve as a tool in the study of the assembly of complex

particles like discs, cylinders, tetrahedrons, etc. An exciting future area of study is in the area of reconfigurable, shape changing colloidal particles. These materials are expected to assemble complex structures, which cannot be assembled through the assembly of rigid particles. The DC electric field assembly method can prove to be an important tool to not only assemble, but also actuate the shape-change in colloidal particles.

### 6.2 Patchy Ellipsoidal Particle Synthesis and Assembly

In chapter 4, we demonstrate the synthesis of novel patchy ellipsoidal particles. These particles were assembled at different salt concentrations and imaging and image-processing techniques were developed to analyze the resultant assembly structures. Ordered assemblies were observed at specific salt concentrations. In chapter 5, these ordered assemblies of are specifically synthesized and analyzed. We note the formation of novel, ordered one-dimensional, self-limiting chains for the Janus ellipsoid particles. In this study, we also use a directed assembly method to reconfigure the ordered self-assembled chains. AC electric fields positionally reconfigure the self-assembled Janus ellipsoids to form a distinct, new ordered assembly. This order-order reconfiguration leads to the elongation of the self-assembled chains on application of AC electric fields. Such systems could potentially be used for micro robotics and artificial muscle applications. The interesting new colloidal synthesis and assembly methods can be extended easily to other colloidal systems to give new assembly structures and functional properties.

Patchy particles are a new and exciting area for colloidal assembly and this work significantly advances assembly studies in this area. In this work, we have predominantly focused on ellipsoidal patchy particles. The synthesis methods introduced in this work can be

easily extended to other shapes such as discs, spherocylinders, etc. Simulations have shown that such particles can be assembled into novel structures. Further, the single-particle and assembly dynamical properties of these particles can also now be studied experimentally using the newly developed analysis tools (CLSM direct visualization and image-processing). Finally, the rheological properties of patchy particle systems can also be studied to evaluate the structural properties of these materials. This would however require significant scale-up in the synthesis methods introduced in this work to produce large quantities of patchy particles.

Catalytically active patchy particles can be synthesized by simple modifications of the synthesis methods introduced in this work (using catalytically active materials, like platinum, instead of gold in the patchy particle synthesis process). The dynamic properties of shape anisotropic catalytically active particles are expected to be highly complex, and this study can be pursued easily using the methods introduced in this work. Further, the flocking assembly properties can also be experimentally studied for the first time using these methods.

Self-assembly traditionally leads to the formation of a single, minimum-free energy assembly structure. However, applications such as micro robotics and artificial muscles require the ability to actuate micron-scale structures. In this thesis, we have demonstrated the use of AC electric field direct assembly methods to actuate our self-assembled Janus ellipsoid structures. This novel approach to actuate self-assembled structures can be applied to other colloidal assembly systems to create order-order reconfiguration in self-assembled structures.

### 6.3 DC Electric Field Assembly of Patchy Particles

In the two parts of this thesis, we have first developed DC electric field assembly methods to assemble colloidal particles into 3D structures. Next, we have synthesized, self-

assembled and AC electric field-assembled patchy ellipsoidal particles. A unique opportunity going forward would be the ability to incorporate all three assembly methods in one experiment to create 3D self-assemblies that can be actuated.

We performed a quick test experiment to demonstrate the posiibilities in this area going forward. We used Janus spheres, synthesized using methods introduced in Chapter 4 and assembled them at the electrode surface using the DC electric field device introduced in Chapter 2. The Janus sphere particles were resuspended in a 50:50 water:dimethylsulfoxide solvent system to permit application of a DC electric field device, while maintaining relative stability of the particles (Figure 6-2a). Figure 6-2b shows the formation of a 2D assembly at the electrode surface. Small crystalline domains were also observed. Thus, janus particles were self-assembled into close packed crystalline structures. After ~ 10 minutes (gives the system enough time to self-assemble), we switched on an AC electric field along the vertical z-direction to replace the previously applied DC electric field. We note that the orientation of the Janus half of the particle's orientation can be controlled. Thus, 2D and 3D colloidal Janus sphere self-assemblies can be actuated using this experiment. Potential applications for such systems could include optical mirrors for example. The stability of Janus particles in DC electric fields and non-aqueous solvents is currently a challenge. Surface stabilizing thiols and surfactants will have to be used to enhance the stability of this system. Another significant challenge ist he sedimentation of Janus particles in solution, and density matching solvents will have tob e used to perform such experiments. Further, the current synthesis methods will need to be scaled up to perform such bulk assemblies. However, inspite of the challenges, Figure 6-2 shows the possibility of creating bulk patchy colloidal reconfigurable materials by combing the self and directed assembly of particles

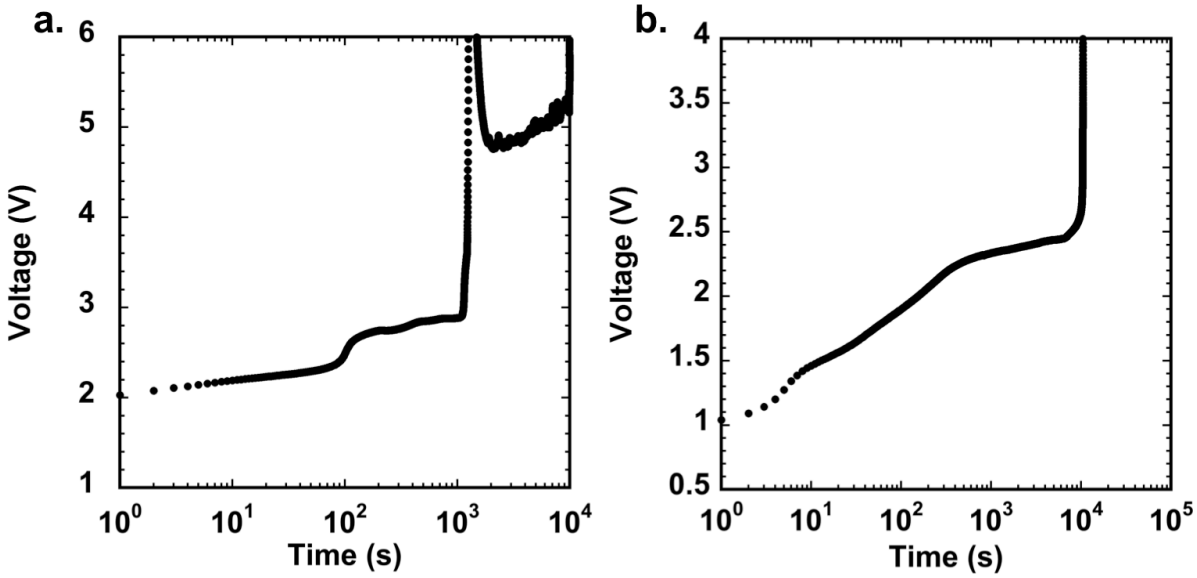


**Figure 6-1:** a. Change in voltage as a function of time on application of a constant current (50 μA/cm$^2$) for dimethyl sulfoxide (DMSO) and 100 mM tetra butylammonium bromide (TBAB) salt. b. Change in voltage as a function of time on application of a constant current (50 μA/cm$^2$) for dimethyl sulfoxide (DMSO) with 100 mM tetra butylammonium bromide (TBAB) salt and 100 mM manganese acetyl acetonate.

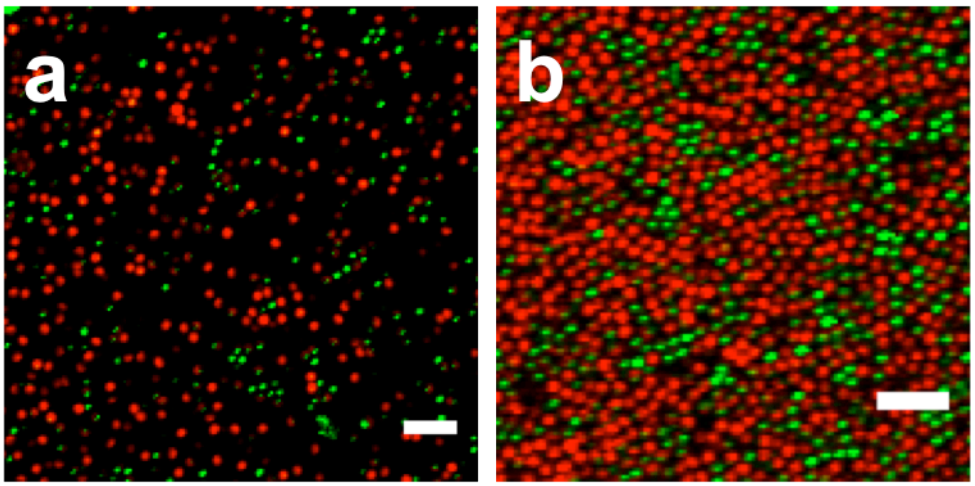


**Figure 6-2:** a. Janus spheres in solution before application of DC electric field. b. Janus spheres in solution on application of a 2.5 V DC electric field. Scale bars are 5 μm